Effect of t_{2g} Orbitals on Domain Walls in Electron-Doped Perovskite Ferroelectrics

A Thesis Submitted to the Committee on Graduate Studies
in Partial Fulfillment of the Requirements for the
Degree of Master of Science in the Faculty of Arts and Science.

Trent University
Peterborough, Ontario, Canada

M.Sc Materials Science Program
September 2023

Abstract

Effect of t_{2g} Orbitals on Domain Walls in Electon-Doped Pervoskite Ferroelectrics

by Brennan Cornell

In electron-doped ferroelectrics, the free electrons can become concentrated along the domain walls which act like a conducting surface. We consider the impact of free electrons occupying the t_{2g} orbitals on the domain walls of an electron-doped perovskite ferroelectric. We build an analytical model based on Landau-Ginzburg-Devonshire theory, and a trio of tight-binding Hamiltonians for free electrons. We self-consistently solve for the polarization, potential, and electron density using a finite-difference approximation. We find that the ferroelectric is effectively charge neutral. The free electrons are attracted to the positively-charged domain wall, leaving it with a small residual charge. As the electron density increases, the domain walls tilt to form zig-zag domain walls. Orbital selectivity of the t_{2g} orbitals depends on the relative orientations of the orbital plane and the domain wall. This property influences the rate at which the domain wall tilts as a function of the electron density.

Keywords: ferroelectric, perovskite, domain wall, charged domain wall, strontium titanate, lanthanum aluminate, Landau-Ginzburg

Acknowledgments

I would like to thank Dr. Bill Atkinson for taking a chance on a middle-aged man desperately trying to recapture the glory of youth. Your support, encouragement, and insights made this all possible.

I would like to thank my committee members, Dr. Carlo Bradac, and Dr. Hendrick de Haan for their guidance and support. I would also like to thank my external exmaminer, Dr. Oleg Rubel, who persevered through this document in the middle of his summer break.

I would like to recognize the financial support provided by Veteran's Affairs Canada to retired members of the Canadian Armed Forces pursuing educational upgrading.

Finally, thanks to all of my family and friends for their support and patience while I pursued my mid-life crisis.

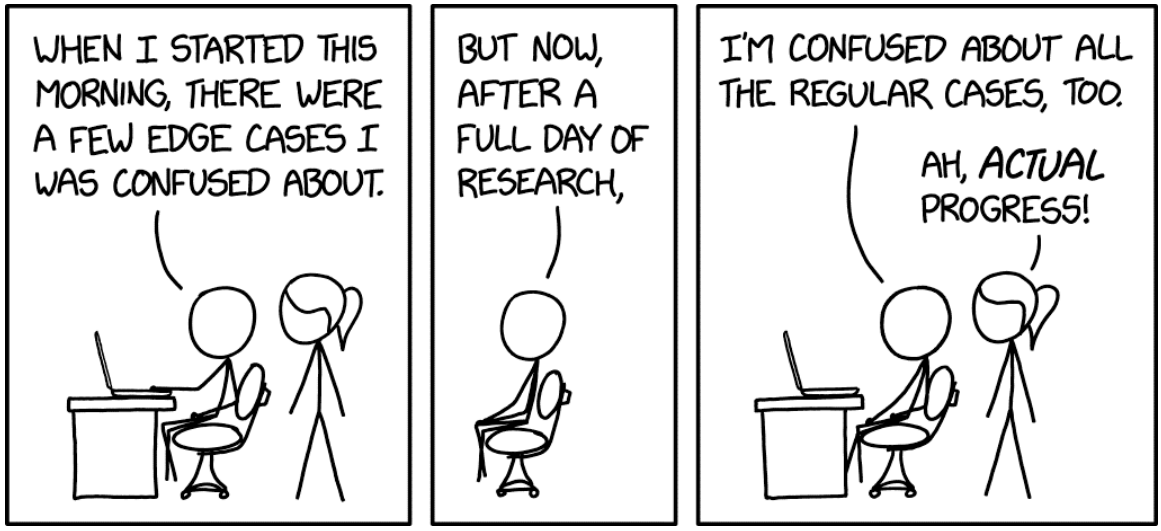

Figure 1: The experience of writing a thesis.

Statement of Contributions

The following contributions to this work are recognized:

1. Theory - The theory is based on well-known principles of electrodynamics and quantum mechanics, but this specific development [see Chapters 2 and 3] was undertaken by the author under the guidance of his supervisor, Dr. Bill Atkinson.

2. Model - The model was originally developed and published by Dr. Bill Atkinson in Ref [1]. Amendments to the model for the t_{2g} orbitals were developed and implemented by the author under the guidance of his supervisor.

3. Code - The FORTRAN code was entirely written by the author with the exception of the Anderson Mixing module which was provided by Dr. Bill Atkinson, and some code for calculating the electric field from the potential.

4. Figures - All figures were created by the author using a mix of Python, Paint 3D and PowerPoint.

5. Results - All analysis was done by the author under the guidance of his supervisor.

Contents

Abstract **ii**

Acknowledgments **iii**

Statement of Contributions **v**

Table of Contents **viii**

List of Figures **x**

List of Tables **xi**

1 Introduction **1**

1.1 Ferroelectricity 1

1.2 Perovskites 2

1.3 Domain Walls 2

1.4 Depolarizing Fields 4

1.5 Charged Domain Walls 6

1.6 LAO-STO Interface 7

1.7 Landau Theory 8

1.8 Motivation 9

2 Theory **12**

2.1 Analytical Model 12

2.2 Free Energy Equation 14

2.3 Tight-Binding Model . . . 17
2.4 Gauss' Law . . . 25
2.5 Coarse Graining the Model . . . 25
2.6 Summary . . . 31

3 Computational Model **32**
3.1 Discretization . . . 34
3.2 Initial Conditions . . . 35
3.3 Solving for the Polarization . . . 36
3.4 Solving for the Potential . . . 40
3.5 Solving for the Free Charge Densities . . . 42
3.6 Summary . . . 43

4 Results and Analysis **44**
4.1 Polarization . . . 46
4.2 Domain Wall Width . . . 49
4.3 Charge Distribution . . . 50
4.4 Domain Wall Neutrality . . . 54
4.5 Electric Fields . . . 57
4.6 Orbital Selectivity . . . 59
4.7 Kinetic Energy . . . 64
4.8 Summary . . . 69

5 Conclusion **70**

Bibliography **72**

A Raw Data **80**

B Code Discussion **87**
B.1 Overview . . . 87
B.2 Modules and Libraries . . . 89
B.2.1 Main.f90 . . . 89

B.2.2 Physical_Constants.f90 89
B.2.3 Coefficients.f90 90
B.2.4 Initialize.f90 91
B.2.5 LGD_Eqn_mod.f90 95
B.2.6 Potential_mod.f90 95
B.2.7 Schrodinger_mod.f90 95
B.2.8 Convergence.f90 96
B.2.9 WriteToFile.f90 96
B.2.10 Anderson_Mix.f90 97
B.3 Compiler Commands 97
B.4 Git Hub 97

C Generating the LGD Equation **99**

List of Figures

1 The experience of writing a thesis iv

1.1 Structure of a cubic perovskite with chemical structure ABO_3 3
1.2 Common domain wall configurations 4
1.3 Depolarizing field 5
1.4 LAO-STO Interface 8

2.1 Cartoon of the model 13
2.2 Cartoon of the tight-binding model 18
2.3 Cartoon of the hopping matrix elements 22
2.4 Cartoon of a one-dimensional repeating lattice 26

3.1 Flowchart describing the computational algorithm 33
3.2 Cartoon showing the interleaved lattices 35
3.3 Cartoon overlaying the lattice structure on the physical model 36

4.1 Polarization for the anisotropic model for different n_{2D} 46
4.2 Comparison of polarization between the isotropic and anisotropic models . 48
4.3 Domain wall width 49
4.4 Polarization near the domain wall for $n_{2D} = 0.2$ 51
4.5 Bound charge densities for $n_{2D} = 0.0$ and 0.15 53
4.6 Total charge density 54
4.7 Plot of maximum polarization versus surface polarization 56
4.8 Electric Fields 58

4.9 Orbital selectivity near the domain wall 61
4.10 Charge density cut for $n_{2D} = 0.4$ and x=15 nm 62
4.11 Electronic sub-band structure for $n_{2D} = 0.1$ 63
4.12 Cartoon of toy models for kinetic energy 65
4.13 Orbital preferences for different toy models based on kinetic energy 67
4.14 Orbital selectivity near the domain wall for $n_{2D} = 0.4$ 68

A.1 Polarization, electron densities and bound polarization for n2D=0.0 81
A.2 Polarization, electron densities and bound polarization for n2D=0.1 82
A.3 Polarization, electron densities and bound polarization for n2D=0.15 83
A.4 Polarization, electron densities and bound polarization for n2D=0.2 84
A.5 Polarization, electron densities and bound polarization for n2D=0.3 85
A.6 Polarization, electron densities and bound polarization for n2D=0.4 86

List of Tables

2.1 Short table of model parameters 15

B.1 Table of convergence parameters 90
B.3 Table of model geometry parameters 91
B.2 Table of looping and import/export parameters 91
B.4 Table of LGD module parameters 92
B.5 Table of Potential module parameters 93
B.6 Table of Schrodinger module parameters 94
B.7 Table of Mixing Parameters 96
B.8 Table of compiler commands 98

C.1 Table of cubic symmetries and associated transformations 104

Chapter 1

Introduction

1.1 Ferroelectricity

Ferroelectricity gets its name from ferromagnetism. In iron, the magnetic moments align themselves locally to form domains. In unmagnetized iron, the orientations of the magnetic moments are random, so the iron has no net magnetic moment. When an external magnetic field is applied, the magnetic moments experience a torque, and rotate to align themselves with the field. This gives the iron a net magnetic moment. A material is a ferromagnet when the magnetic moments remain aligned after the magnetic field is removed, and can be reoriented by application of another magnetic field. This property is why iron becomes magnetized after being put into a magnetic field. In a ferroelectric, we have the same property, but the role of the magnetic moment is now played by the electric dipole, and the magnetic field is replaced by the electric field.

Ferroelectrics cover a very broad range of materials [2]. They are receiving intense interest at the moment because of their utility in advanced electronics. Low-power computer memory using ferroelectric domains to store information has been commercially available since the early 2000's [3]. Recent interest is focused on the manipulation of charged domain walls within ferroelectrics since they can act like wires in nano-electronics [4–9], or multiferroic effects, where the ferroelectricity is entangled with another property (e.g., ferromagnetism [10–12], superconductivity [13, 14]).

We are interested in the charged domain walls of perovskite ferroelectrics, modelled on

the transition metal perovskite, strontium titanate ($SrTiO_3$ or STO). STO is naturally a paraelectric; it becomes polarized by an external electric field, but relaxes rapidly when the field is removed. However, it is an incipient ferroelectric, needing only minor changes to its chemical composition [15–17], or the application of an external strain [18, 19], to become ferroelectric. When free electrons are added to a ferroelectric, they can help stabilize otherwise unfavourable configurations of charged domain walls [4, 5]. We will investigate how free electrons affect the charged domain walls in perovskite ferroelectrics.

1.2 Perovskites

A common class of ferroelectrics are the perovskites [20,21] (e.g., barium titanate ($BaTiO_3$) [22], lead titanate ($PbTiO_3$) [23]). Perovskites have the chemical formula ABO_3 and a cubic unit cell structure with the A atoms at the corners, and the B atom in the centre of the cube. The oxygen atoms are face-centered, and form an octahedron around the center with the oxygen at the vertices [see Fig 1.1]. The A and B atoms become cations, giving up their valence electrons to the oxygen atoms. When the unit cell becomes distorted (e.g, one of the cations moves away from its high-symmetry position), cations-anions asymmetry generates a small dipole moment. The distortion of the unit cell and the dipole moment act on their neighbours, and result in a cascade of aligned dipole moments which generate a polarization. In a ferroelectric, for temperatures below the Curie temperature, T_{Curie}, this polarization emerges spontaneously as the result of a phase transition.

1.3 Domain Walls

The polarization, $\mathbf{P}$, is the sum of the dipole moments per unit volume (units of charge per area). The interface between two regions (or domains) with different polarizations is called a *domain wall*. At the domain wall, the polarization transforms from one orientation to the other across a width of $\sim 1 - 10$ nm [5, 24]. Fig 1.2 shows common orientations of polarization across a domain wall.

From classical electrodynamics, a change in polarization across a surface leads to a

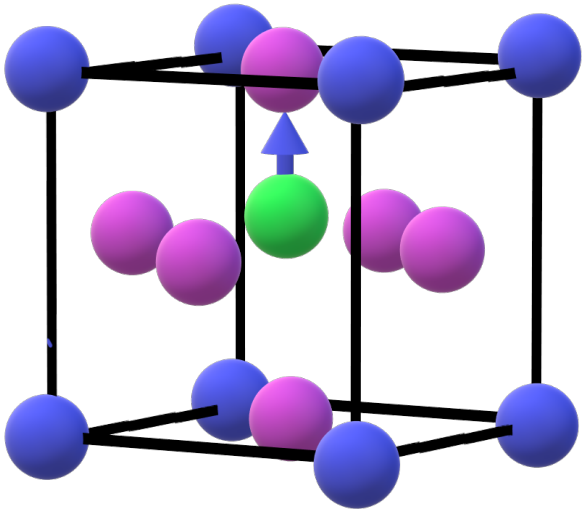

Figure 1.1: Cubic perovskite with chemical structure ABO_3. The A atoms (blue) are found in the corners of the unit cell. The B atom (green) is found in the centre. The oxygen atoms (purple) are face-centered, and form an octahedron around the B atom with the oxygen at the vertices. The A and B atoms are cations, giving up their valence electrons to form oxygen anions. In the ferroelectric state, the unit cell becomes slightly deformed as one of the cations moves away from its high-symmetry position. This generates a small dipole moment between the cation and the oxygen anions. We show the simplified case of the B cation moving upwards relative to the oxygen octahedra. In reality, other atoms within the unit cell would also adjust their positions, but the cubic symmetry remains broken.

bound surface charge, σ^{b}, given by

$$\sigma^{\mathrm{b}} = (\mathbf{P}_1 - \mathbf{P}_2) \cdot \hat{n}, \tag{1.1}$$

where $\mathbf{P}_1$ and $\mathbf{P}_2$ are the polarization along either side of the surface, and $\hat{n}$ is the unit normal to the side of the surface corresponding with P_1. When we have a head-to-head or tail-to-tail domain wall configuration [see Fig 1.2, (b) - (e)], the surface charge is non-zero. These are called *charged domain walls* (CDWs).

Recent research has focused on charged domain walls in ferroelectrics [4–7] [8, 9]. Since polarization can be controlled by external fields, we can control the location of charged domain walls. The properties of the charged domain wall are different from the bulk ferroelectric, which make them interesting in their own right. Practically, however, they can act

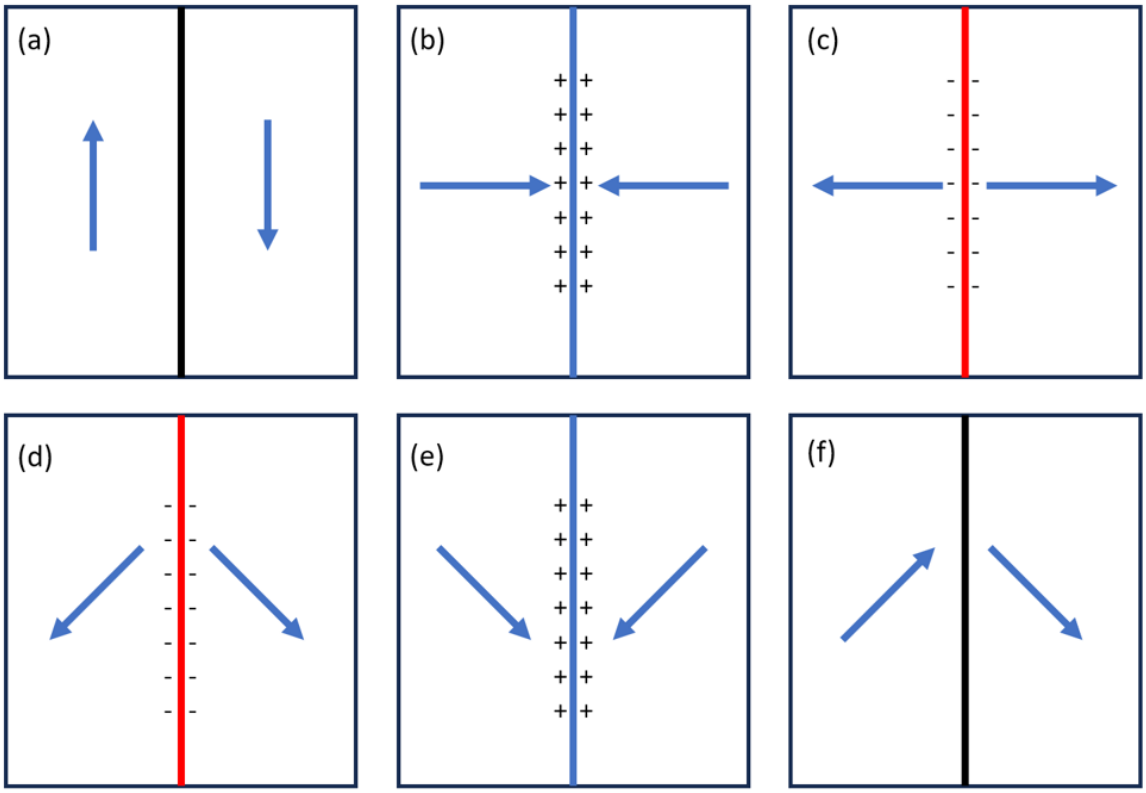

Figure 1.2: Common domain wall configurations. (a) The 180° (or Kittel) domains with a neutral domain wall (black line). The polarization (blue arrow) lies parallel to the domain wall on either side. There is no bound charge across the domain wall. (b) The head-to-head charged domain wall. The change in polarization across the wall leaves it with a positive bound charge (blue line). (c) The tail-to-tail charged domain wall. The change in polarization across the wall gives it a negative bound charge (red line). (d) – (e) The tail-to-tail, and head-to-head 90° charged domain walls, so-called because the polarizations intersect at 90°. (f) The head-to-tail 90° neutral domain wall. Although we have shown the case where the angle between the two intersecting polarization is 90°, each polarization can make a different angle with the domain wall leading to bound charge in the head-to-tail configuration as well. However, not all configurations are possible due to compatibility of the unit cells across the domain wall.

like adjustable wires within an insulator.

1.4 Depolarizing Fields

Each dipole generates an electric field [see Fig 1.3] which acts on its neighbours. Collectively, however, their effects tend to cancel out, except from regions of bound charge. The net electric field generated by a collection dipoles is just the electric field generated by the bound charges.

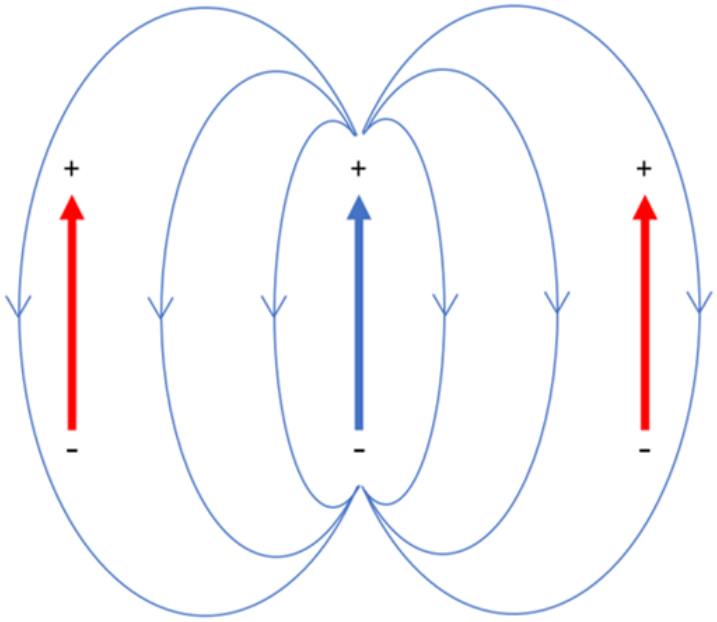

Figure 1.3: Depolarizing field. Each dipole (arrow) generates its own electric field (blue lines).

Consider a head-to-head domain wall [see Fig 1.2, (b)]. The domain wall can be approximated by an infinite sheet of positive charge which produces an electric field oriented anti-parallel to the polarization. The dipoles experience a force which suppresses their magnitude, and a torque attempting to rotate them through 180^o degrees. Both act to reduce the polarization, and diminish the bound charge across the domain wall. This field is called the *depolarizing* electric field because it acts to suppress the polarization. But suppressing the polarization leads to a smaller bound charge, which leads to a smaller depolarizing field, which leads to a larger polarization, etc... There is an equilibrium between the polarization and depolarizing field that must be met for a charged domain wall to exist. Ferroelectrics would prefer neutral domain walls.

1.5 Charged Domain Walls

The electrostatic energy, U, captures the dilemma of the charged domain wall. It is given by

$$U = \frac{1}{2}\epsilon_0 \int_{\mathrm{V}} d^3\mathbf{r} \ |\mathbf{E}|^2, \tag{1.2}$$

where ϵ_0 is the permittivity of free space, V is the volume of the charged domain wall, and $\mathbf{E}$ is the depolarizing field. In order to reduce its energy, a system can reduce the volume of the charged domain wall, or reduce the magnitude of the electric field, preferably to zero.

One mechanism for stabilizing charged domain walls is through mobile charge carriers. Most ferroelectrics are insulators. The presence of free electrons was assumed to suppress the ferroelectric effect through the screening of the local dipole moments, preventing the emergence of polarization [25, 26]. However, research over the past decade has identified a wide variety of ferroelectric materials that also possess metallic properties generated by dilute concentrations of free electrons [26]. These include various perovskites [27] including barium titanate [28–30], doped strontium titanate [31], lithium niobate [32], and metallic $LiOsO_3$ [33]. The free electrons become localized around positive charge centers (e.g., positively-charged domain walls, cations) where they screen the depolarizing electric fields [27]. When a charged domain wall is fully compensated by charge carriers, the net charge is zero $\Rightarrow \mathbf{E} = 0$, and they no longer generate self-destructive depolarizing fields.

When mobile charge carriers are bound to the domain wall, it acts like a conductive surface within the insulating ferroelectric. Conductivity along the charged domain wall and within the insulating bulk are orders of magnitude different [5]. In electron-compensated charged domain walls, values of $10^8 - 10^{10}$ times larger have been observed in barium titanate ($BaTiO_3$) [34] and 10^{13} times larger in lithium niobate ($LiNbO_3$) [32].

There are several mechanisms for generating mobile charge carriers in a ferroelectric [4]. For instance, electrons can transfer across the bandgap. In Ref [7], the authors explored this for perovskites. They concluded that the electron density required to neutralize the charged domain walls in a perovskite was too high to be achievable from intrinsic carriers ($\sim 10^{26}$

e/m^3). A second mechanism is to seed the ferroelectric with mobile, ionized impurities. The impurities donate electrons into the conduction band, and become positively-charged ions. They can collect at positive and negatively charged domain walls, respectively. Charged domain walls in bulk crystals of $BaTiO_3$ are suspected of being stabilized in this way [8]. Since ions are much more massive than electrons, it is observed that the free-electron compensated positively-charged domain walls have much higher conductivity than ion-compensated negatively-charged domain wall [4]. A third technique is to introduce electrons from another material in contact with the ferroelectric. When the interface is electrically suitable, electrons can migrate across the boundary. For instance, $BaTiO_3$ with platinum electrodes is predicted to produce tail-to-tail charged domain walls where the free electrons are donated by the platinum [7] [35]. We will also assume this mechanism for our system.

1.6 LAO-STO Interface

We will consider an interface between lanthanum aluminate ($LaAlO_3$, or LAO) and strontium titanate (STO). Lathanum aluminate is an insulating perovskite. It can be grown as a thin film composed of alternating layers of LaO and AlO_2 [see Fig 1.4] on an STO substrate. These LAO layers are oppositely charged, and build-up a potential across the material as more-and-more layers are deposited [36]. This is called the *polar catastrophe* since the increasing potential should be energetically unstable [37,38]. One proposed resolution, called *electronic reconstruction*, is for the potential to raise the valence band energy of the LAO above the conduction band energy in the STO [38]. This leads to a transfer of electrons from the surface of the LAO to the interface of the STO, where they accumulate in the titanium t_{2g} bands [39]. Indeed, above a critical thickness of LAO ($\sim 3-4$ unit cells), an electron gas is observed on the strontium side of the LAO-STO interface [38, 40, 41]. The holes in the LAO valence band generate an electric field that holds the electrons within a few unit cells of the interface [42]. The constrained free electrons are referred to as a two-dimensional electron gas (2DEG) [37]. However, an externally applied voltage can free the electrons to stray away from the interface, and into the bulk of the STO.

This 2D electron gas also exhibits several other interesting properties including super-

conductivity [43–45], ferromagnetism [46, 47] and a possible nematic phase [48, 49].

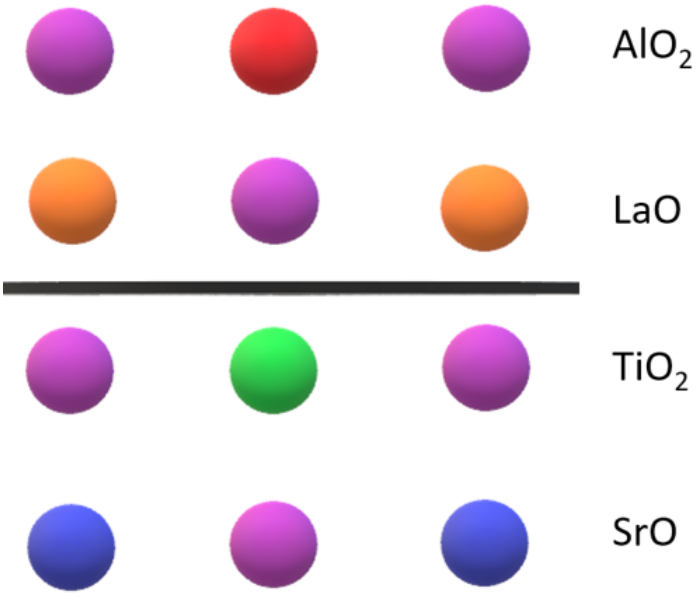

Figure 1.4: LAO-STO Interface. The purple spheres are oxygen, the blue spheres are strontium, the green sphere is titanium, the orange spheres are lanthanum, and the red sphere is aluminum. The interface consists of a layer of TiO_2 met by a layer of LaO. The LaO and AlO_2 layers have alternating positive and negative charges which generate a potential. The SrO and TiO_2 layers are charge neutral.

1.7 Landau Theory

Ferroelectric behaviour is described using extensions of *Landau Theory*. Landau Theory posits that phase transitions can be described using an *order parameter*, T, corresponding with some property of the ordered phase. By definition, the order parameter is zero in one phase, and non-zero in another. The Landau free energy of the system is assumed analytic at the transition point allowing for the expansion of the energy in terms of the order parameter [50]. We write

$$\mathcal{F}[T] = \int d^3\mathbf{r} \left[a + bT(\mathbf{r}) + cT(\mathbf{r})^2 + dT(\mathbf{r})^3 + eT(\mathbf{r})^4 + \dots \right] \tag{1.3}$$

where $\mathcal{F}$ is the free energy, $d^3\mathbf{r}$ is an infinitesimal unit of volume, and $a, b, c, d, e \dots$ are coefficients. The free energy equation can include as many terms as desired, but is usually

terminated by the sixth or eighth order. The final term is always of even order; otherwise there is not a stable lowest-energy state. Stable and meta-stable states of the system correspond with global and local minima of the energy, respectively. Using symmetry arguments, the number of terms and coefficients in the expansion of the free energy are constrained. This is discussed in greater detail in Appendix C. Appendix A to Ref [51] contains a wide range of free energy equations and coefficients for different materials.

For ferroelectrics, the usual order parameter is the polarization, $\mathbf{P} = (P_x, P_y, P_z)$. Our system satisfies cubic symmetry (O_h) at high temperatures, so our free energy equation must satisfy multiple rotational, mirror-image, and inversion symmetries [see Table C.1]. Our equation will be discussed at greater length in section 2.2.

Laudau-Ginzburg-Devonshire (LGD) theory is the application of Landau theory to ferroelectrics. In traditional Landau theory, only powers of the order parameter are considered. In LGD theory, the free energy also includes gradients of the order parameter [50].

Consider the following free energy equation for a 1D ferroelectric system,

$$\mathcal{F}[P] = \int dx \left[\frac{a}{2} P(x)^2 + \frac{b}{4} P(x)^4 + \alpha \left(\frac{\partial P}{\partial x} \right)^2 \right]. \tag{1.4}$$

Solutions have the form $P(x) = P_0$ or $P_0 \tanh(kx)$ where $k = \sqrt{\frac{-a}{2\alpha}}$ and $P_0 = \sqrt{\frac{-a}{b}}$. It models a second order phase transition (i.e. stable minima) whenever $a \leq 0$ and $b, \alpha \geq 0$. Otherwise, the only real-valued solution is $P = 0$ and no ferroelectric phase emerges. The uniform solution P_0 is the lowest energy solution, and is called the *bulk solution*. It does not have any domain walls because the polarization never changes signs. The tanh solutions switch signs when $x = 0$, signaling the presence of a domain wall. They approach the bulk solution away from the domain wall since $P(x) \approx P_0$ whenever $|x| \gg 0$.

1.8 Motivation

We will examine the impact of free electrons on the charged domain walls of electron-doped perovskite ferroelectrics. Our model is motivated by the LAO-STO interface where the itinerant electrons donated by the LAO to the STO are free to stabilize charged domain

walls. We adapt the model at Ref [1] as the basis for our work. It combines Landau theory for the polarization with charge densities generated from a Hamiltonian for the free electrons occupying a single, isotropic orbital. We adapt this model such that the free electrons occupy the t_{2g} orbitals (i.e. d_{xy}, d_{xz}, d_{yz}) on the titanium atom, and consider different two-dimensional electron densities (n_{2D}) simulating different amounts of charge transfer across the LAO-STO interface. An advantage of this approach is that we can make our models reasonably large ($\sim 30 \times 50$ nm^2) compared with density functional theory (DFT) models for same level of computational resources.

Literature on the modelling of free electrons and charged domain walls is limited. Many papers use a Laudau equation to model polarization, but rarely consider the electrons, and treat them classically when they do. A 1D model for the switchability of an electron-doped ferroelectric substrate was investigated at Ref [52]. It combined an Ising model for the polarization with a Hamiltonian for the electronic structure. An atomistic shell-model and continuous phase-field simulation was used to investigate the impact of defects on domain walls in $PbTiO_3$ [23]. This model used LGD theory, but did not include any charge carriers. Smaller-scale DFT efforts have looked at the domain wall structure for different materials (e.g., $PbTiO_3$ [53, 54], $BaTiO_3$ [55], $BiFeO_3$ [56]), but they did not include itinerant electrons. Ref [9] appears is the closest to our model. It examined a 1D charged domain wall using a simplified fourth-order Landau equation (no gradient terms), and a Schrödinger equation for the electrons. The system is solved self-consistently using Hartree and Thomas-Fermi methods. However, the authors make a number of assumptions in order to simplify the problem analytically which we do not make. This is heartening, because other than Ref [1] on which our model is based, this approach is unique.

We are interested in understanding:

1. How does the electron density affect the domain wall?

2. How do the t_{2g} orbitals and the domain wall interact?

We develop the analytical model in Chapter 2. The discrete implementation used computationally is described in Chapter 3. Our results and discussion are found in Chapter 4. The raw results can be found in Appendix A. A discussion of the model's implementation

in code is presented in Appendix B.

Chapter 2

Theory

2.1 Analytical Model

We model an itinerant electron gas occupying the titanium t_{2g} orbitals (i.e. d_{xy}, d_{xz}, d_{yz}) of strontium titanate. The STO is topped with a thin cap of lanthanum aluminate, and held between two capacitors at an external voltage ΔV=0. The lowest-energy conduction bands have t_{2g} character, and are located at the titanium cation [39]. The STO-LAO interface results in a two-dimensional electron gas (2DEG) forming on the STO side of the interface. This is characterized by a two-dimensional electron density, n_{2D}. Unless otherwise stated, n_{2D} has units of electrons per unit cell. A short list of model parameters can be found in Table 2.1.

A cartoon of our system is shown in Fig 2.1. It consists of a block of STO with dimensions (L_x, L_y, L_z), topped by a polar cap with dimensions (L_x, L_y, L_p). They are sandwiched between two capacitor plates on top and bottom which are held at 0 V. The ferroelectric and the polar cap have total polarizations at position $\mathbf{r}$ satisfying

$$\mathbf{P}^{\text{total}}(\mathbf{r}) = \mathbf{P}(\mathbf{r}) + \mathbf{P}^{\text{back}}(\mathbf{r}), \tag{2.1}$$

where the ferroelectric polarization, $\mathbf{P}$, arises from the ferroelectric distortion of the unit cell, and the background polarization, $\mathbf{P}^{\text{back}}$, comes from atomic distortions and non-ferroelectric

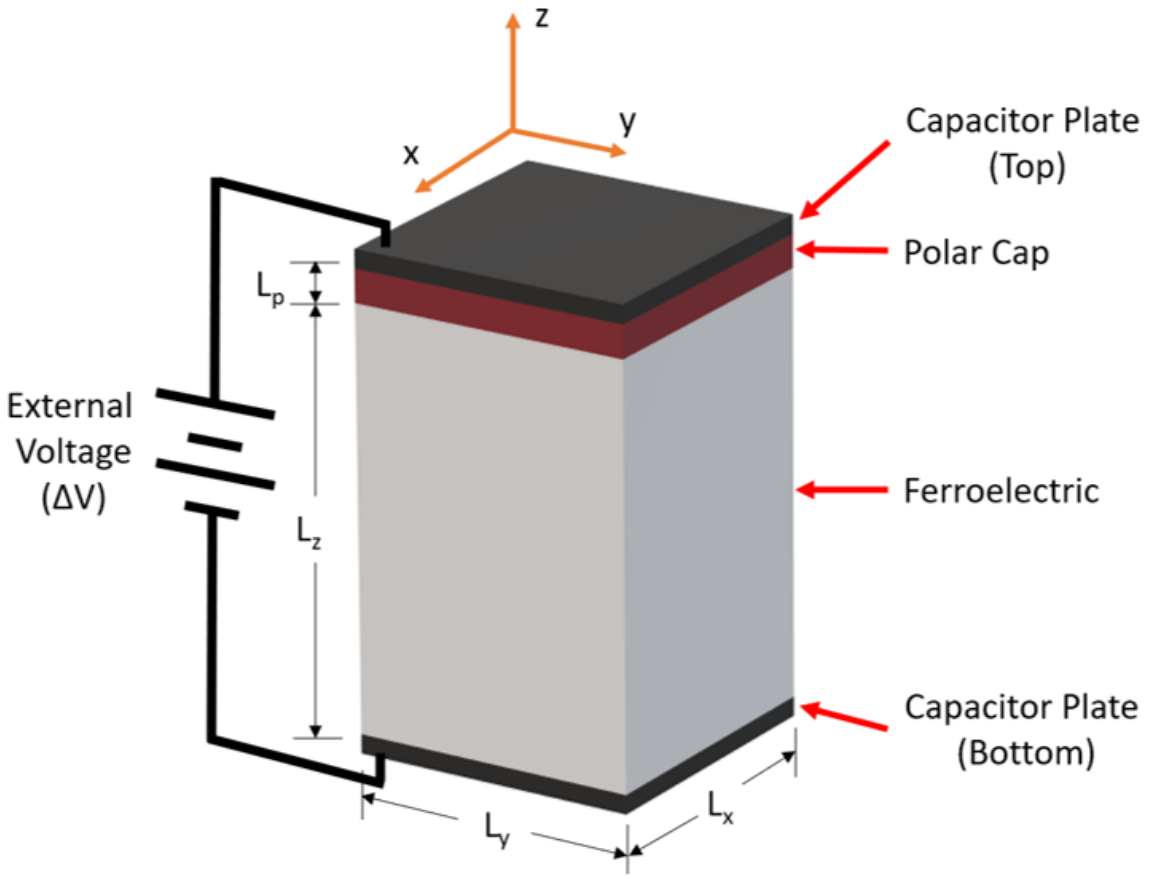

Figure 2.1: The ferroelectric (e.g., STO) is sandwiched between two capacitor plates and a polar cap (e.g., LAO). The external voltage is kept at 0 V in our model.

phonons. The background polarization is given by

$$\mathbf{P}^{\text{back}}(\mathbf{r}) = \epsilon_0 \chi \mathbf{E}(\mathbf{r}), \tag{2.2}$$

where ϵ_0 is the permittivity of free space, $\mathbf{E}$ is the electric field, and χ is the background dielectric susceptibility. Since the polar cap is not a ferroelectric, $\mathbf{P}_{\text{PC}} = 0$. We have

$$\chi(z) = \begin{cases} \chi_{\text{FEM}} \text{ when } 0 \leq z \leq L_z \\ \chi_{\text{PC}} \text{ when } L_z < z \leq L_z + L_p \end{cases} \tag{2.3}$$

We denote the ferroelectric polarization vector, $\mathbf{P}(\mathbf{r}) = (P_x(\mathbf{r}), P_y(\mathbf{r}), P_z(\mathbf{r}))$, the electric potential, $\phi(\mathbf{r})$, and the charge density, $\rho(\mathbf{r})$ for a position vector $\mathbf{r} = (x, y, z)$ in cartesian coordinates. We impose 90° rotational symmetry around the z-axis, so that $L_x = L_y$. Al-

though our model has finite dimensions, we impose the periodic boundary condition along the x- and y-axes, and the open boundary condition along the z-axis. We further impose translational invariance between unit cells along the y-axis (i.e. $\mathbf{P}(x, y, z) = \mathbf{P}(x, y + a, z)$ where a is the lattice constant). This leaves us with 2D solutions in x-z plane. Experimentally, we see several systems where the domain wall appears to be 2D [23] [57] [58]. Moreover, although interesting, solving this model in 3D is computationally intensive, and beyond our current resources. We set $P_y = 0$, and suppress the y-axis going forward except when required for clarity or relevancy.

The boundary conditions are summarized below:

$$\frac{\partial P_x}{\partial z}(x, y, 0) = \frac{\partial P_x}{\partial z}(x, y, L_z) = 0 \tag{2.4}$$

$$\frac{\partial P_z}{\partial z}(x, y, 0) = \frac{\partial P_z}{\partial z}(x, y, L_z) = 0 \tag{2.5}$$

$$\mathbf{P}(x, y, z) = \mathbf{P}(x + L_x, y, z) \tag{2.6}$$

$$\mathbf{P}(x, y, z) = \mathbf{P}(x, y + a, z) \tag{2.7}$$

Since we set ΔV=0, the potential, $\phi(\mathbf{r})$, satisfies

$$\phi(x, y, 0) = 0 \tag{2.8}$$

$$\phi(x, y, L_z + L_p) = 0 \tag{2.9}$$

2.2 Free Energy Equation

From classical thermodynamics, the polarization can be found by minimizing the free energy. Since the variables in our free energy are themselves functions, we use calculus of variations to find the minima. We consider the free energy, $\mathcal{F}$, to be a functional of the polarization components, (P_x, P_y, P_z).

For cubic symmetry, a generic fourth-order LGD free energy in the ferroelectric polar-

Model	Coefficients	Value	Units	Reference
LGD	a_1	2×10^8	$C^{-2}m^2N$	Appendix A in [51]
	a_3	-1.6×10^8	$C^{-2}m^2N$	Appendix A in [51]
	b	5.88×10^9	$C^{-4}m^4N$	Appendix A in [51]
	b'	-2.94×10^9	$C^{-4}m^4N$	Appendix A in [51]
	g_{11}	2×10^{-10}	$C^{-2}m^6N$	Appendix A in [51]
	g_{44}	2×10^{-10}	$C^{-2}m^2N$	Appendix A in [51]
Schrödinger	t_0	0	meV	[52]
	$t_\parallel$	236	meV	[52]
	$t_\perp$	35	meV	[52]
	χ_{PC}	25	Dimensionless	[52]
	χ_{FEM}	4.5	Dimensionless	[52]
Physical	a (Lattice Constant)	0.395	nm	[52]
	Δ (Lattice Spacing)	1	nm	Model in [1]
	L_x	28	nm	Model in [1]
	L_y	28	nm	Model in [1]
	L_z (FEM)	46	nm	Model in [1]
	L_p (PC)	5	nm	Model in [1]
	ΔV	0	V	

Table 2.1: Short table of model parameters. A complete list of the parameters and variables in the model can be found in Appendix B.

ization, $\mathbf{P}$, is

$$\begin{aligned}\mathcal{F}_P &= \int_0^{L_x} dx \int_0^{L_z} dz \Bigg\{ \frac{g_{11}}{2} \left[\left(\frac{\partial P_x}{\partial x} \right)^2 + \left(\frac{\partial P_y}{\partial y} \right)^2 + \left(\frac{\partial P_z}{\partial z} \right)^2 \right] \\ &+ \frac{g_{44}}{2} \left[\left(\frac{\partial P_x}{\partial y} \right)^2 + \left(\frac{\partial P_x}{\partial z} \right)^2 + \ldots + \left(\frac{\partial P_z}{\partial y} \right)^2 \right] \\ &+ \frac{A}{2} \left(P_x^2 + P_y^2 + P_z^2 \right) + \frac{b}{4} \left(P_x^2 + P_y^2 + P_z^2 \right)^2 + \frac{1}{2\epsilon_0} \left[|\mathbf{P}|^2 + |\mathbf{D}|^2 \right] \\ &+ \frac{b'}{2} \left(P_x^2 P_y^2 + P_y^2 P_z^2 + P_z^2 P_x^2 \right) \Bigg\} - \frac{1}{\epsilon_0} \mathbf{D} \cdot \mathbf{P}, \end{aligned} \tag{2.10}$$

where $\mathbf{D}$ is the electric displacement. Our free energy equation does not contain any terms related to the strain or tilt which are sometimes included. The subscript indices of g_{11} and g_{44} refer to directions in the Voigt notation.

The terms in $\mathbf{D}$ and $\mathbf{P}$ come from replacing the electrostratic energy term [see Eq (1.2)]

with the electric displacement and polarization given by

$$\mathbf{D} = \mathbf{P} + \epsilon_0 \mathbf{E} \tag{2.11}$$

$$\Rightarrow \mathbf{E} = \frac{1}{\epsilon_0} \left(\mathbf{D} - \mathbf{P} \right). \tag{2.12}$$

We replace the electric field with these terms because they make it easier to obtain self-consistent solutions. Otherwise, we find that the depolarizing field associated with the bound charge leads to large oscillations in the polarization from cycle-to-cycle which never decay. The algorithm will be discussed in Chapter 3 and Appendix B.

Although our free energy respects cubic symmetry, in reality, the z-axis in inequivalent to x and y because we have a thin film. We separate the A coefficient into a_1 and a_3 coefficients for the P_x^2 and P_z^2 terms, respectively. We only want the ferroelectric polarization to emerge along the z-axis, so we set $a_1 > 0$ and $a_3 < 0$ [see section 1.7 regarding signs of the coefficients].

With a little work, we obtain

$$\begin{aligned} \frac{\delta \mathcal{F}}{\delta P_x} =& P_x \left[a_1 + \frac{1}{\epsilon_0} + b|\mathbf{P}|^2 + b'(P_y^2 + P_z^2) \right] \\ & - g_{11} \left(\frac{\partial^2 P_x}{\partial x^2} \right) - g_{44} \left(\frac{\partial^2 P_x}{\partial y^2} \right) - g_{44} \left(\frac{\partial^2 P_x}{\partial z^2} \right) - D_x \\ =& 0. \end{aligned} \tag{2.13}$$

and,

$$\begin{aligned} \frac{\delta \mathcal{F}}{\delta P_z} =& P_z \left[a_3 + \frac{1}{\epsilon_0} + b|\mathbf{P}|^2 + b'(P_x^2 + P_y^2) \right] \\ & - g_{44} \left(\frac{\partial^2 P_z}{\partial x^2} \right) - g_{44} \left(\frac{\partial^2 P_z}{\partial y^2} \right) - g_{11} \left(\frac{\partial^2 P_z}{\partial z^2} \right) - D_z \\ =& 0. \end{aligned} \tag{2.14}$$

For fixed $\mathbf{D} = (D_x, D_z)$, we solve Eqs (2.13) and (2.14) to find P_x and P_z.

2.3 Tight-Binding Model

The distribution of electrons is determined by the Schrödinger equation. Since this is hard to solve, we will approximate their behaviour using a *tight binding model* (TBM) to build an effective Hamiltonian, $\hat{H}$, that combines the electron-electron, and Coulombic interactions. In the TBM, we assume that the electrons associated with any given nucleus have a very low probability of leaving the vicinity of the nucleus. The wavefunction describing their probability density is effectively zero for ranges greater than the size of the unit cell. As a consequence, the only matrix elements governing their interactions are those between adjacent nucleii in the lattice (see Fig 2.2).

We denote the crystal Hamiltonian, $\hat{H}_0$, by

$$\hat{H}_0 = -\frac{\hbar^2}{2m}\nabla^2 + U(\mathbf{r}), \tag{2.15}$$

where m is the mass of the electron, and $U(\mathbf{r})$ is the ionic potential of the crystal lattice. The eigenvector-eigenvalue solutions of $\hat{H}_0$ correspond with the eigenstates and associated energies for the electrons arising from the lattice structure itself (e.g., Bloch electrons).

We define the effective Hamiltonian, $\hat{H}$, by combining the lattice energies with the Coulomb energies,

$$\hat{H} = \hat{H}_0 - e\phi(\mathbf{r}), \tag{2.16}$$

where ϕ is the electrostatic potential acting on the electrons. We remark that we will use boldface $\mathbf{H}$ to denote a matrix Hamiltonian.

Let $\zeta_{i\alpha\sigma} = |i\alpha\sigma\rangle$ denote a Wannier orbital of type $\alpha \in \{d_{xy}, d_{xz}, d_{yz}\}$ with particle of spin σ located at the lattice point i. The set of $|i\alpha\sigma\rangle$ over all $\{i, \alpha, \sigma\}$ form an orthonormal basis for the wavefunctions. Using this basis, we can define the hopping matrix elements $(h_{ij,\alpha\alpha',\sigma\sigma'})$ of the tight-binding Hamiltonian as follows

$$\begin{aligned} h_{ij,\alpha\alpha',\sigma\sigma'} =& \langle i\alpha\sigma|\hat{\mathbf{H}}|j\alpha'\sigma'\rangle \\ =& \langle i\alpha\sigma|\hat{\mathbf{H}}_0|j\alpha'\sigma'\rangle - e\langle i\alpha\sigma|\phi(\mathbf{r})|j\alpha'\sigma'\rangle \\ =& t_{ij,\alpha\alpha',\sigma\sigma'} - e\phi(\mathbf{r}_i)\delta_{ij,\alpha\alpha',\sigma\sigma'}, \end{aligned} \tag{2.17}$$

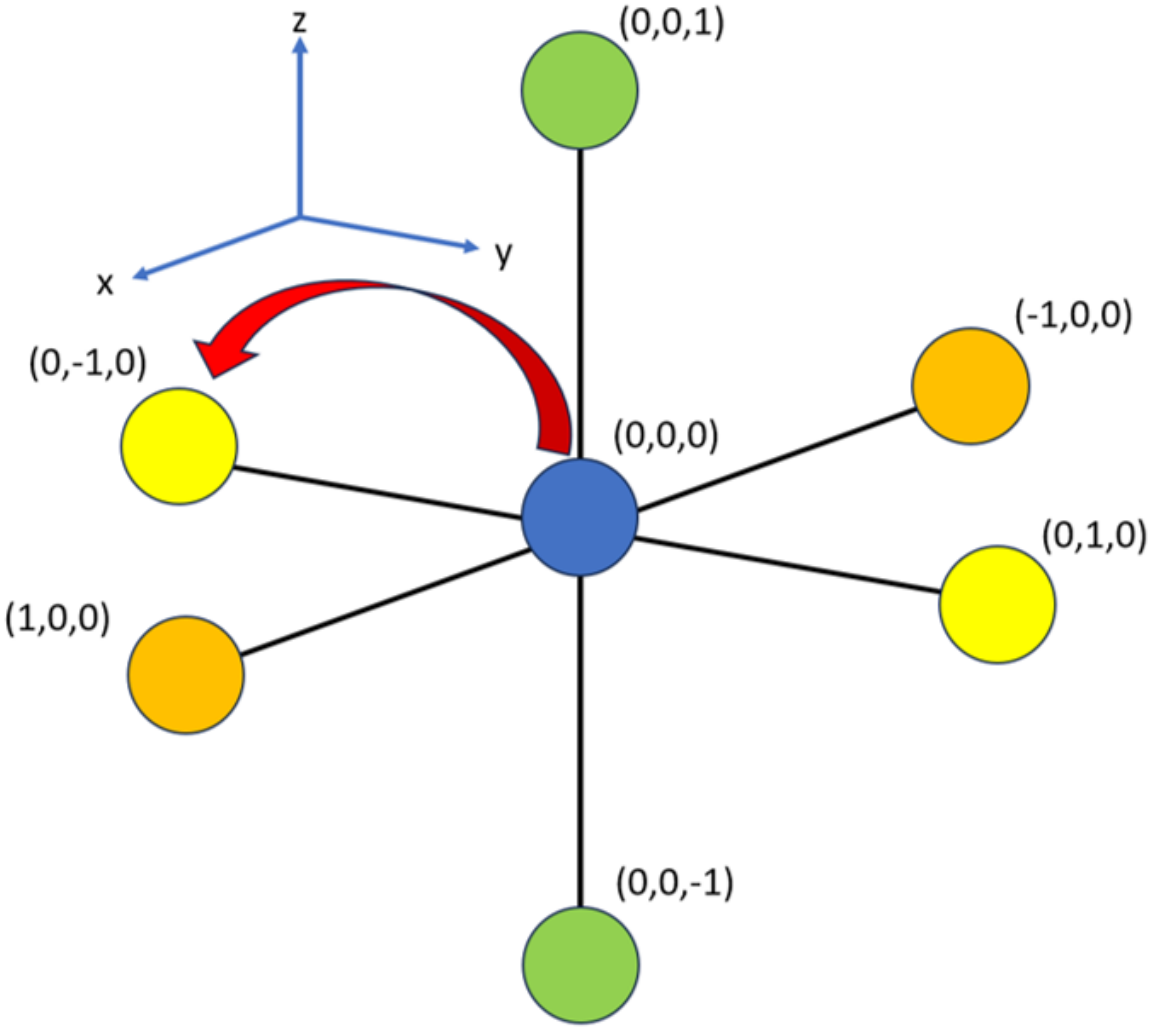

Figure 2.2: The tight-binding model. Transitions only occur between adjacent lattice points along the x-, y- and z-axis. The hopping matrix element, $t_{ij,\alpha\alpha',\sigma\sigma'}$, determines the probability for an electron at location $i = (i_x, i_y, i_z)$ in orbital α with spin σ to transition to location $j = (j_x, j_y, j_z)$ in orbital α' with spin σ'. In the TBM, we must have that $i = j$ or one of $j_x = i_x \pm 1$, $j_y = i_y \pm 1$ or $j_z = i_z \pm 1$.

where $t_{ij,\alpha\alpha',\sigma\sigma'}$ is the corresponding hopping matrix element in the crystal Hamiltonian, $\hat{\mathbf{H}}_0$, using the same basis elements. This approximation is good when $\phi(\mathbf{r})$ is smoothly varying. The second term is only non-zero when the two atomic orbitals are identical (location, type and spin).

The probability of transitions between orbitals of different types or different spins is very low, so the hopping matrix element for transitions $|i\alpha\sigma\rangle \Rightarrow |j\alpha'\sigma'\rangle$ is taken to be zero whenever $\alpha \neq \alpha'$ or $\sigma \neq \sigma'$, and we ignore any spin-orbit coupling. We further assume

that hopping matrix elements are independent of spin. The matrix representation of $\hat{H}$ will be block-diagonal for an appropriate choice of basis where each block corresponds with a different orbital type. We denote the block-diagonal matrices by $\hat{\mathbf{H}}^{\alpha}$ where α identifies the orbital type, and t_{ij}^{α} is the hopping matrix element between lattice locations i and j. Re-writing Eq (2.16), we obtain

$$\hat{\mathbf{H}}^{\alpha} = \sum_{i,j} \hat{c}_{i\alpha\sigma}^{\dagger} \left[t_{ij}^{\alpha} - e\phi(i)\delta_{ij} \right] \hat{c}_{j\alpha\sigma}, \tag{2.18}$$

where $\hat{c}_{i\alpha\sigma}^{\dagger}$ and $\hat{c}_{j\alpha\sigma}$ are the creation and annihilation operators for an electron at lattice site i, in orbital type α, with spin σ.

Since our model is translationally invariant in the y-direction, it is useful to separate this direction from our Hamiltonian. Let j be a location in the discrete three-dimensional lattice where

$$j = (j_x, j_y, j_z). \tag{2.19}$$

Fourier transforming from real space into $k-$space along the y-axis gives

$$\hat{c}_{j\alpha\sigma} = \frac{1}{\sqrt{N_y}} \sum_{k} e^{ikj_y} \hat{c}_{(j_x,k,j_z)\alpha\sigma}, \tag{2.20}$$

where N_y is number of lattice points along the y-axis, and k are the wavenumbers corresponding with the y-axis.

Subtituting Eq (2.20) into Eq (2.18),

$$\begin{aligned} \hat{\mathbf{H}}^{\alpha} = \sum_{j,j'} & \left(\frac{1}{\sqrt{N_y}} \sum_{k} e^{-ikj_y} \hat{c}_{(j_x,k,j_z)\alpha}^{\dagger} \right) \\ & \left[t_{ij}^{\alpha} - e\phi(j)\delta_{jj',\alpha\alpha'} \right] \left(\frac{1}{\sqrt{N_y}} \sum_{k'} e^{ik'j'_y} \hat{c}_{(j'_x,k_{m'},j'_z)\alpha\sigma} \right) \end{aligned} \tag{2.21}$$

To separate out the y-components of j, j', define $I = (j_x, j_z), J = (j'_x, j'_z)$. Notationally,

$Ij_y = (j_x, j_y, j_z)$. Reworking the equation, we have

$$\hat{\mathbf{H}}^{\alpha} = \sum_{I,J} \sum_{j_y, j_y'} \left(\frac{1}{\sqrt{N_y}} \sum_{k} e^{-ikj_y} \hat{c}^{\dagger}_{Ik\alpha} \right) \left[t^{\alpha}_{IJ,j_y j_y'} - e\phi_{Ij_y} \delta_{IJ,j_y j_y'} \right] \left(\frac{1}{\sqrt{N_y}} \sum_{k'} e^{ik'j_y'} \hat{c}_{Jk'\alpha} \right). \tag{2.22}$$

In order to combine the exponential terms, we need to consider the action of the hopping matrix element and potential energy terms on the exponential. From translational symmetry, ϕ must be independent of y, and the hopping matrix element $t^{\alpha\sigma}_{IJ,j_y j_y'}$ only depends on $j_y - j_y'$. Consequently, we can combine the exponential terms, as follows

$$\hat{\mathbf{H}}^{\alpha} = \frac{1}{N_y} \sum_{I,J} \sum_{j_y, j_y'} \left(\sum_{k,k'} e^{-i(k'j_y' - kj_y)} \right) \left(\hat{c}^{\dagger}_{Ik\alpha} \right) \left[t^{\alpha}_{IJ,(j_y - j_y')} - e\phi(Ij_y)\delta_{IJ,j_y j_y'} \right] \left(\hat{c}_{Jk'\alpha\sigma} \right). \tag{2.23}$$

Define $\kappa = j_y' - j_y$. Then,

$$\begin{aligned} \sum_{k,k'} e^{i(k'j_y' - kj_y)} &= \sum_{k,k'} e^{i(k'(\kappa + j_y) - kj_y)} \\ &= \sum_{k,k'} e^{i(k'\kappa + k'j_y - kj_y)} \\ &= \sum_{k,k'} e^{i(k'\kappa)} e^{i(k'-k)j_y}. \end{aligned} \tag{2.24}$$

and,

$$\sum_{j_y} e^{i(k-k')j_y} = N_y \delta_{kk'}. \tag{2.25}$$

Substituting Eq (2.24) into Eq (2.23), we obtain

$$\begin{aligned}\hat{\mathbf{H}}^{\alpha} =& \frac{1}{N_y}\sum_{I,J}\left(\sum_{j_y,\kappa}\sum_{k,k'} e^{i(k'\kappa)}e^{i(k'-k)j_y}\right)\left(\hat{c}^{\dagger}_{Ik\alpha}\right)\Big[t^{\alpha}_{IJ,\kappa} \\ & - e\phi(I)\delta_{IJ}\delta_{\kappa}\Big]\left(\hat{c}_{Jk'\alpha}\right) \\ =& \frac{1}{N_y}\sum_{I,J}\left(\sum_{\kappa}\sum_{k} e^{ik\kappa}N_y\right)\left(\hat{c}^{\dagger}_{Ik\alpha}\right)\Big[t^{\alpha}_{IJ,\kappa} \\ & - e\phi(I)\delta_{IJ}\delta_{\kappa}\Big]\left(\hat{c}_{Jk\alpha}\right) \\ =& \sum_{I,J}\sum_{k}\left\{\sum_{\kappa} e^{ik\kappa}\left(\hat{c}^{\dagger}_{Ik\alpha}\right)\Big[t^{\alpha}_{IJ,\kappa} - e\phi(I)\delta_{IJ}\delta_{\kappa}\Big]\left(\hat{c}_{Jk\alpha}\right)\right\}, \end{aligned} \tag{2.26}$$

where we used the orthogonality condition from Eq (2.25). We remark that $\delta_{IJ}\delta_{\kappa} = 1$ whenever $j = Ij_y = Jj'_y = j'$.

For fixed I, J, and k, we define

$$\tilde{h}^{\alpha}_{IJ}(k) = \sum_{\kappa} e^{ik\kappa}\Big[t^{\alpha}_{IJ,\kappa} - e\phi(\mathbf{r}_I)\delta_{IJ}\delta_{\kappa}\Big]. \tag{2.27}$$

In the tight-binding model, the only non-zero terms in the Hamiltonian will coincide with the same location and the nearest neighbours. (i.e. if $i = (i_x, i_z)$, then $j = (i_x, , i_z), (i_x \pm 1, i_z)$, or $(i_x, i_z \pm 1)$ and $\kappa = 0, \pm 1$). Substituting these results into (2.26), we can calculate the individual hopping matrix elements,

$$\tilde{h}^{\alpha}_{IJ}(k) = \begin{cases} t^{\alpha}_{II,0} - e\phi_I\delta_{IJ} + 2t^{\alpha}_{II,1}\cos(k) \text{ when } I = J \\ t^{\alpha}_{IJ,0} \text{ when } I = (i_x, i_z), \text{ and } J = (i_x \pm 1, i_z) \text{ or } (i_x, i_z \pm 1) \\ 0 \text{ otherwise} \end{cases}, \tag{2.28}$$

where we assumed that $t_{IJ,-1} = t_{IJ,1}$ by symmetry.

We will simplify this notation by remarking that $(IJ, 0)$ corresponds with transitions between adjacent lattice cells along the x- and z-axes, and that $(II, \pm 1)$ corresponds with transitions between adjacent lattice cells along the y-axis. When $I = (i_x, i_z)$, we set $t^{\alpha}_{IJ,0} = t^{\alpha}_x$ when $J = (i_x \pm 1, i_z)$, $t^{\alpha}_{IJ,0} = t^{\alpha}_z$ when $J = (i_x, i_z \pm 1)$, $t^{\alpha}_{II,\pm 1} = t^{\alpha}_y$, and $t^{\alpha}_{II,0} = t^{\alpha}_0$. We

re-write Eq (2.28) in the new notation as

$$\tilde{h}^{\alpha}_{IJ}(k) = \begin{cases} t^{\alpha}_0 - e\phi_I\delta_{IJ} + 2t^{\alpha}_y\cos(k) \text{ when } I = J \\ t^{\alpha}_x \text{ when } I = (i_x, i_z), \text{ and } J = (i_x \pm 1, i_z) \\ t^{\alpha}_z \text{ when } I = (i_x, i_z), \text{ and } J = (i_x, i_z \pm 1) \\ 0 \text{ otherwise} \end{cases}, \tag{2.29}$$

From experimental observations, hopping matrix elements in the same plane as the orbital are larger than matrix elements between planes. (i.e. electrons hop more freely between d_{xy} orbitals aligned in the same x-y plane than between d_{xy} orbitals stacked along the z-axis.) We denote the hopping matrix element for orbital type α to the same orbital type in the same plane as $t^{\alpha}_{\parallel}$, and perpendicular to the plane as $t^{\alpha}_{\perp}$ [see Fig 2.3]. Moreover, we assume that the orbitals can all be rotated into one another, so the hopping matrix element cannot have any orbital dependence. (i.e. $t^{\alpha}_{\parallel} = t_{\parallel}$ and $t^{\alpha}_{\perp} = t_{\perp}$ for all α.)

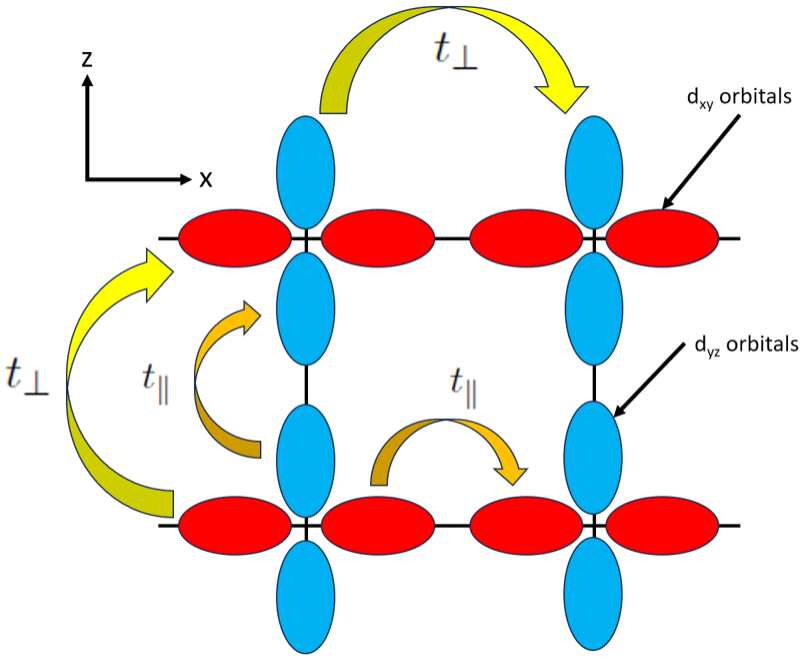

Figure 2.3: Cartoon of the hopping matrix elements between orbital types. We have 2×2 lattice points each of which has a set of d_{xy} (red) and d_{yz} (light blue) orbitals. The view is along the y-axis, so we see the orbitals side-on extending in the x-y (red) and y-z planes (light blue). The orange arrows represent hopping between two sites that lie in the same orbital plane ($t_{\parallel}$). The yellow arrows correspond with hopping between two sites that are perpendicular to the orbital's plane ($t_{\perp}$). The d_{xz} orbitals are not shown.

For the different orbital types, α, we obtain the following hopping matrix elements:

$$t_0^{d_{xy}} = t_0^{d_{xz}} = t_0^{d_{yz}} = t_0 \tag{2.30}$$

$$t_x^{d_{xy}} = -\,t_{\parallel} \tag{2.31}$$

$$t_y^{d_{xy}} = -\,t_{\parallel} \tag{2.32}$$

$$t_z^{d_{xy}} = -\,t_{\perp} \tag{2.33}$$

$$t_x^{d_{xz}} = -\,t_{\parallel} \tag{2.34}$$

$$t_y^{d_{xz}} = -\,t_{\perp} \tag{2.35}$$

$$t_z^{d_{xz}} = -\,t_{\parallel} \tag{2.36}$$

$$t_x^{d_{yz}} = -\,t_{\perp} \tag{2.37}$$

$$t_y^{d_{yz}} = -\,t_{\parallel} \tag{2.38}$$

$$t_z^{d_{yz}} = -\,t_{\parallel} \tag{2.39}$$

Since t_0 lies along the diagonal, we can set it as the zero of energy in our system (i.e. $t_0 = 0$). The negative sign is convention since it is known that $t_{IJ} \leq 0$ for all I, J.

We can separate our matrix, $\tilde{\mathbf{H}}^{\alpha}(k)$, into the sum of a new Hermitian matrix, $\tilde{\mathbf{T}}^{\alpha}$, and a diagonal matrix, $\tilde{\mathbf{D}}^{\alpha}(k)$, defined by

$$\tilde{\mathbf{T}}^{\alpha}_{IJ} = \begin{cases} t_0^{\alpha} - e\phi_I\delta_{IJ} \text{ when } I = J \\ t_x^{\alpha} \text{ when } I = (i_x, i_z) \text{ and } J = (i_x \pm 1, i_z) \\ t_z^{\alpha} \text{ when } I = (i_x, i_z) \text{ and } J = (i_x, i_z \pm 1) \\ 0 \text{ otherwise} \end{cases}, \tag{2.40}$$

and,

$$\tilde{\mathbf{D}}^{\alpha}_{IJ}(k) = \begin{cases} 2t_y^{\alpha}\cos(k) \text{ when } I = J \end{cases} \tag{2.41}$$

$$\Rightarrow \tilde{\mathbf{D}}^{\alpha}(k) = 2t_y^{\alpha}\cos(k)\mathbf{I}, \tag{2.42}$$

where $\mathbf{I}$ is the identity matrix.

Since $\tilde{\mathbf{T}}$ is Hermitian, it can be diagonalized with a unitary matrix, U. Trivially, we also have that $U^{\dagger}\tilde{\mathbf{D}}^{\alpha}(k)U = \tilde{\mathbf{D}}^{\alpha}(k)$. The column vectors of U are the eigenfunctions of $\tilde{\mathbf{T}}^{\alpha}$ for eigenvalues ϵ_n where n is the column index. The column vectors of U are also trivially the eigenfunctions of $\tilde{\mathbf{D}}^{\alpha}$ with eigenvalues $\epsilon(k) = 2t_y^{\alpha}\cos(k)$. Then, the column vectors of U are the eigenfunctions of $\tilde{\mathbf{H}}^{\alpha}(k) = \tilde{\mathbf{T}}^{\alpha} + \tilde{\mathbf{D}}^{\alpha}$ with eigenvalues $\epsilon_n + \epsilon(k)$. Conveniently, since $\tilde{\mathbf{T}}$ does not have any k-dependence, the eigenvalue equation only needs to be solved once for each of the orbital types.

To determine the distribution of electrons across our energy bands, we use the Fermi-Dirac function, $f(\epsilon)$, to determine the probability of occupancy for a state with energy ϵ, given by

$$f(\epsilon) = \left(1 + e^{\frac{\epsilon-\mu}{k_B T}}\right)^{-1}, \tag{2.43}$$

where k_B is Boltzmann's Constant, T is the temperature, and μ is the chemical potential. We determine μ by imposing

$$N = \sum_{\sigma}\sum_{n} f(\epsilon_{nk}), \tag{2.44}$$

where N is the total number of electrons across all of energy levels $\epsilon_{nk} = \epsilon_n + \epsilon(k)$, σ is the spin, and n is summed over all energy levels.

The free charge density at lattice point i is

$$\rho_i^f = -2\frac{e}{V}\sum_{\alpha}\sum_{n}\sum_{k} f(E_{nk\alpha})|U_{ni\alpha}|^2 \tag{2.45}$$

where 2 comes from spin, $-e$ is the charge of the electron, and V is the volume of the unit cell. The energy $E_{nk\alpha}$ is the energy $\epsilon_n + \epsilon(k)$ for the orbital α. The matrix element $U_{ni\alpha}$ is the element of the eigenvector corresponding with energy ϵ_n for orbital α at lattice point i.

2.4 Gauss' Law

Given the electron density, we can calculate the electric potential, $\phi(\mathbf{r})$ across the lattice. This is defined as

$$\phi(\mathbf{r}_i) = \frac{1}{4\pi\epsilon_0} \sum_{j \neq i} \frac{\rho^{\text{total}}(\mathbf{r}_j)}{|\mathbf{r}_i - \mathbf{r}_j|}, \tag{2.46}$$

where $\rho^{\text{total}}(\mathbf{r}_i) = \rho^f(\mathbf{r}_i) + \rho^b(\mathbf{r}_i) + \rho^{\text{ext}}(\mathbf{r}_i)$, the sum of the free, bound and external charges, respectively. The external charge is found along the capacitor plates, and is already accounted for in the boundary conditions for the potential [see Eqs (2.8) and (2.9)]. In order to not double-count its effect, $\rho^{\text{ext}}(\mathbf{r}_i) = 0$.

It is computationally easier to tackle this problem using the differential form of Gauss' law

$$-\nabla^2\phi = \frac{\rho(\mathbf{r})}{\epsilon_0}. \tag{2.47}$$

The free charge density is obtained from Eq (2.45). The total bound charge is given by

$$\rho^b(\mathbf{r}) = -\nabla \cdot \mathbf{P}^{\text{total}}(\mathbf{r}) \tag{2.48}$$

where $\mathbf{P}^{\text{total}}$ is given by Eq (2.1). The electric field, $\mathbf{E}$, is determined by

$$\mathbf{E}(\mathbf{r}) = -\nabla\phi(\mathbf{r}). \tag{2.49}$$

2.5 Coarse Graining the Model

We constructed our model using a lattice of unit cells as the fundamental building block. However, it is often useful to change the discrete steps of the model to some other value to facilitate larger volumes. Our computational bottleneck is the size of the Hamiltonian matrices which depends on the number of grid points. By making the distances between lattice points larger, the physical extent of our model increases without increasing the computational burden. We refer to this process as *coarse graining* the model since we are extending our approximation over a larger distance, sacrificing precision for scale. We will use the term lattice constant, a, to refer to the size of the unit cell, and lattice spacing, Δ,

to refer to the size of the coarse-grained lattice.

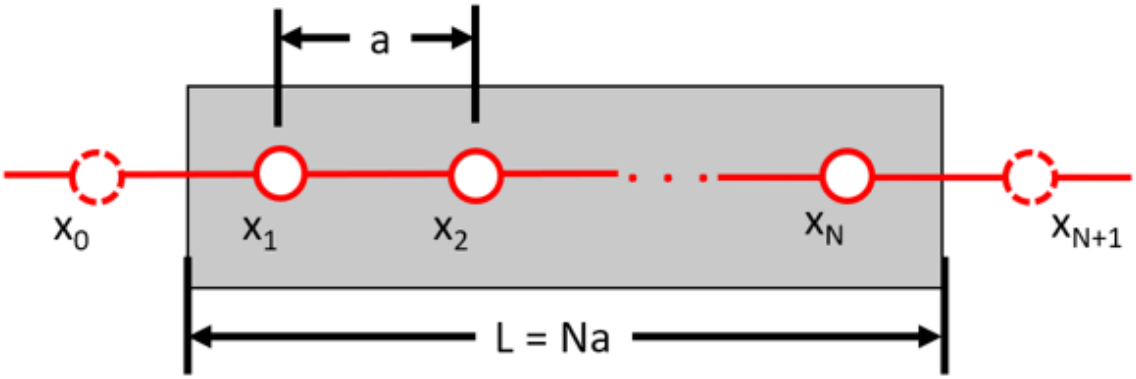

Figure 2.4: A one-dimensional repeating lattice. The distance between lattice points is a such that $x_n = na$, and lattice repeats after N points.

Fig 2.4 shows a one-dimensional repeating lattice. Absent a potential, $\phi(x)$, we can write the tight-binding Hamiltonian as

$$\mathbf{H} = \begin{bmatrix} \epsilon_0 & -t_1 & . & . & -t_1 \\ -t_1 & \epsilon_0 & -t_1 & . & 0 \\ . & & . & & . \\ . & & -t_1 & \epsilon_0 & -t_1 \\ -t_1 & . & . & -t_1 & \epsilon_0 \end{bmatrix}, \tag{2.50}$$

where $\mathbf{H}$ acts on the eigenvectors made up of $\psi_i = \psi(x_i) = \psi(ia)$ for each $1 \leq i \leq N$. We can re-write the eigenvalue equation as

$$\epsilon_0 \psi_i - t_1 \left(\psi_{i-1} + \psi_{i+1}\right) = E\psi_i. \tag{2.51}$$

There are two boundary conditions that interest us:

1. Periodic Boundary Condition: $\psi_n = \psi_{n+N}$ for all $0 < n \leq N$; and,
2. Open Boundary Condition: $\psi_0 = \psi_N = 0$.

Consider the periodic boundary condition. We can re-write Eq (2.51) as

$$2t_1\psi_i - t_1 \left(\psi_{i-1} + \psi_{i+1}\right) = \left[E - \epsilon_0 + 2t_1\right] \psi_i. \tag{2.52}$$

Since our model is periodic, we consider solutions of the form $\psi_i = A\sin(kx_i) + B\cos(kx_i)$. Using the periodic boundary condition, we must have

$$\begin{aligned} \psi_0 &= \psi_N \\ A\sin(0) + B\cos(0) &= A\sin(kNa) + B\cos(kNa) \\ B &= A\sin(kNa) + B\cos(kNa) \\ \Rightarrow k_n &= \frac{2\pi n}{Na} \end{aligned} \tag{2.53}$$

Using simple algebra, we can re-write $A\sin(k_n x) + B\cos(k_n x) = C\cos(k_n x + \alpha_n)$ for some phase shift α_n and new magnitude $C = \sqrt{A^2 + B^2}$. Then,

$$\begin{aligned} \psi_{i-1} + \psi_{i+1} &= C\cos(k_n(x-a) + \alpha_n) + C\cos(k_n(x+a) + \alpha_n) \\ &= 2C\cos(k_n x + \alpha_n)\cos(k_n a) \end{aligned} \tag{2.54}$$

using sine and cosine summation rules.

Substituting these results back into Eq (2.51), we obtain

$$\begin{aligned} E \cdot C\cos(k_n x + \alpha_n) &= \epsilon_0 C\cos(k_n x + \alpha_n) - t_1 C\left[2\cos(k_n x + \alpha_n)\cos(k_n a)\right] \\ &= C\cos(k_n x + \alpha_n)\left[\epsilon_0 - t_1\cos(k_n a)\right] \\ \Rightarrow E_n &= \epsilon_0 - 2t_1\cos(k_n a), \end{aligned} \tag{2.55}$$

and the set of $\{\sin(k_n x), \cos(k_n x) | n \in Z\}$ forms an orthogonal basis for the wavefunctions.

Now, assume there is a potential $\phi(x)$ with the same periodicity as the lattice (i.e. $\phi(x) = \phi(x + L)$). We construct a new Hamiltonian as

$$\left[H_0 + \phi(x)\right]\psi(x) = \epsilon\psi(x), \tag{2.56}$$

where H_0 is the tight-binding Hamiltonian with no potential [see Eq (2.50)]. We expand

the new wavefunctions in the orthogonal basis as

$$\psi(x) = \sum_n C_n \cos(k_n x + \alpha_n) \text{ where } k_n = \frac{2\pi n}{Na}, \tag{2.57}$$

and,

$$\begin{aligned}
\epsilon \sum_n C_n \cos(k_n x + \alpha_n) &= [H_0 + \phi(x)] \sum_n C_n \cos(k_n x + \alpha_n) \\
&= \sum_n C_n \left[H_0 \cos(k_n x + \alpha_n) + \phi(x) \cos(k_n x + \alpha_n)\right] \\
&= [E_n + \phi(x)] \sum_n C_n \cos(k_n x + \alpha_n).
\end{aligned} \tag{2.58}$$

Now, Taylor expand E_n around k_n to second order,

$$\begin{aligned}
E_n &= \epsilon_0 - 2t_1 \cos(k_n a) \\
&\approx \epsilon_0 - 2t_1 \left[1 - \frac{1}{2}(k_n a)^2\right] \\
&\approx \epsilon_0 - 2t_1 + t_1 (k_n a)^2.
\end{aligned}$$

We only take terms to second order since only states with small values of n will be occupied at low electron densities.

Substituting this result back into Eq (2.58), we get

$$\sum_n C_n \left[\epsilon_0 - 2t_1 + t_1 a^2 k_n^2 + \phi(z)\right] \cos(k_n z + \alpha_n) = \epsilon \sum_n C_n \cos(k_n z + \alpha_n). \tag{2.59}$$

Formally, we can replace k_n with $-i\frac{\partial}{\partial z}$ since

$$\left(-i\frac{\partial}{\partial z}\right)^2 \cos(k_n x + \alpha_n) = k_n^2 \cos(k_n x + \alpha_n). \tag{2.60}$$

This yields

$$\sum_n C_n \left[\epsilon_0 - 2t_1 + t_1 a^2 \left(-i\frac{\partial}{\partial x}\right)^2 + \phi(x)\right] \cos(k_n x + \alpha_n) = \epsilon \sum_n C_n \cos(k_n x + \alpha_n)$$

$$\sum_n C_n \left[\epsilon_0 - 2t_1 - t_1 a^2 \frac{\partial^2}{\partial x^2} + \phi(x)\right] \cos(k_n x + \alpha_n) = \epsilon \sum_n C_n \cos(k_n x + \alpha_n)$$

$$\left[\epsilon_0 - 2t_1 - t_1 a^2 \frac{\partial^2}{\partial x^2} + \phi(x)\right] \sum_n C_n \cos(k_n x + \alpha_n) = \epsilon \sum_n C_n \cos(k_n x + \alpha_n)$$

$$\Rightarrow \left[\epsilon_0 - 2t_1 - t_1 a^2 \frac{\partial^2}{\partial x^2} + \phi(x)\right] \psi = \epsilon\psi. \tag{2.61}$$

This is a new 1D eigenvalue equation that our wavefunctions must satisfy.

We repeat this process for the *open boundary condition*, and obtain

$$\epsilon\psi = \left[\epsilon_0 - 2t_1 - t_1 a^2 \frac{\partial^2}{\partial z^2} + \phi(z)\right] \psi, \tag{2.62}$$

where $\psi(z) = \sum_n C_n \sin(k_n z)$ and $k_n = \frac{\pi n}{Na}, n \in N$.

In our model, the x- and y-directions have the periodic boundary condition while the z-direction satisfies the open boundary condition. Through separation of variables, we can treat each axis independently, and apply Eq (2.61) or Eq (2.62). We combine these results to obtain an effective 3D Schrödinger equation of the form

$$\left[\epsilon_0 - 2t_x^\alpha + t_x^\alpha a^2 \left(\frac{\partial^2}{\partial x^2}\right) - 2t_y^\alpha \cos(k_y a) - 2t_z^\alpha \right.$$
$$\left. + t_z^\alpha a^2 \left(\frac{\partial^2}{\partial z^2}\right) + \phi(x,z)\right]\psi = E^\alpha_{k_x,k_y,k_z}\psi, \tag{2.63}$$

where $t_x^\alpha, t_y^\alpha, t_z^\alpha$ correspond with the energies to hop along the x-,y-, and z-axis respectively for an orbital of type α, and k_x, k_y, k_z are the quantized wavenumbers along those axes. We determined the values for $t_x^\alpha, t_y^\alpha, t_z^\alpha$ at Eqs (2.31) – (2.39). We note that we did not Taylor expand the y-axis because it will not be necessary to construct the terms in our effective Hamiltonian.

Using finite differences, we can approximate the second derivative of ψ by

$$\frac{\partial^2 \psi_i}{\partial \eta^2} = \frac{\psi_{i+1} + \psi_{i-1} - 2\psi_i}{(\Delta\eta)^2}, \tag{2.64}$$

where $\Delta\eta$ is the coarse-grained step along the η-axis, which need no longer be the lattice constant, a.

Substituting this result back into Eq (2.63), and acting on an individual ψ at lattice point $i = (n, m)$ where n, m are the n^{th} and m^{th} lattice locations along the x- and z-directions respectively, we obtain

$$\begin{aligned}
E_{k_x,k_y,k_z}\psi_{(n,m)} &= \left[\epsilon_0 - 2t_x - 2t_y\cos(k_y a) - 2t_z + \phi\right]\psi_{(n,m)} \\
&\quad - t_x a^2\left[\frac{\psi_{(n+1,m)} + \psi_{(n-1,m)} - 2\psi_{(n,m)}}{(\Delta x)^2}\right] \\
&\quad - t_z a^2\left[\frac{\psi_{(n,m+1)} + \psi_{(n,m-1)} - 2\psi_{(n,m)}}{(\Delta z)^2}\right] \\
&= \left[\epsilon_0 - 2t_x\left(1 - \frac{a^2}{(\Delta x)^2}\right) - 2t_z\left(1 - \frac{a^2}{(\Delta z)^2}\right) - 2t_y\cos(k_y a) + \phi\right]\psi_{(n,m)} \\
&\quad - \frac{t_x a^2}{(\Delta x)^2}\left[\psi_{(n+1,m)} + \psi_{(n-1,m)}\right] \\
&\quad - \frac{t_z a^2}{(\Delta z)^2}\left[\psi_{(n,m+1)} + \psi_{(n,m-1)}\right].
\end{aligned} \tag{2.65}$$

This gives us a new Hamiltonian matrix, $\tilde{\mathbf{H}}$, for which the eigenvalues and eigenvectors correspond with the solutions to our 3D tight-binding Hamiltonian with potential ϕ,

$$\tilde{h}^{\alpha}_{ij}(k) = \begin{cases} \epsilon_0 - 2t^{\alpha}_x\left(1 - \frac{a^2}{(\Delta x)^2}\right) - 2t^{\alpha}_z\left(1 - \frac{a^2}{(\Delta z)^2}\right) - 2t^{\alpha}_y\cos(k_y a) + \phi \text{ when } i = j \\ -\frac{t^{\alpha}_x a^2}{(\Delta x)^2} \text{ when } i = (n,m), j = (n \pm 1, m) \\ -\frac{t^{\alpha}_z a^2}{(\Delta z)^2} \text{ when } i = (n,m), j = (n, m \pm 1) \\ 0 \text{ otherwise} \end{cases}, \tag{2.66}$$

where $t^{\alpha}_x, t^{\alpha}_y$ and t^{α}_z are the hopping matrix elements (i.e. $t_{\parallel}$ or $t_{\perp}$) for an orbital of type α along the x-, y- and z-axis respectively. We see that if $\Delta = a$, we recover our original matrix from Eq (2.29). We solve this matrix computationally to obtain the energies and

wavefunctions associated with our coarse-grained model.

2.6 Summary

We have developed all of the components required to solve our model. For a fixed electric displacement, D_x and D_z, we minimize our free energy equations to solve for the ferroelectric polarization, P_x and P_z [see Eqs (2.13) and (2.14)]. Using our potential, ϕ, and 2D electron density, n_{2D}, we solve for our chemical potential [see Eq (2.44)] and free charge density, ρ^f [see Eq (2.45)]. We use the total polarization [see Eq (2.1)] to solve for our bound charge [see Eq (2.48)]. We use our bound and free charge densities to solve for our potential [see Eq (2.47)]. Our solutions must satisfy all of our boundary conditions [see Eqs (2.4) – (2.9)]. Since these equations are implemented computationally, the next chapter will discuss their translation into a discrete form.

Chapter 3

Computational Model

Whereas Chapter 2 covered the theoretical foundation for the model, this chapter will cover the practical implementation. In particular, it translates many equations into their discrete forms, and discusses the algorithms used to solve them. Combined with Appendix B, this should give interested readers a jump start in implementing similar methods. Many months were invested in implementing and testing these equations before results were generated.

Self-consistency was achieved through an iterative cycle of feedback until the change in results between cycles was below a certain threshold. Our computational algorithm is illustrated in Fig 3.1, and described in the following steps:

1. Define the system parameters. (e.g., coefficients in the LGD free energy equation, size of the unit cell, $t_{\|}$). Key parameters are listed in Table 2.1. A complete list of parameters can be found in Appendix B.

2. Define initial conditions. Selection of these values is critical to ensuring that the model converges in a timely manner. This is discussed in Section 3.2.

3. Solve the Landau-Ginzburg-Devonshire (LGD) free energy equations for polarization, $\mathbf{P}$, given by Eqs (2.13) and (2.14). We use a Galarkin-Newton Gradient Approximation (GNGA) described in Ref [59] and adapted in Section 3.3.

4. Solve the Schrödinger equation (2.63) using the coarse-grained Hamiltonian, Eq (2.66), to find the energies and wavefunctions for the potential, ϕ. The chemical potential

is determined using Eq (2.44). The charge densities are determined using Eq (2.45). This is described further in Section 3.5.

5. Given the free and bound charge densities, solve for the potential, ϕ, using Eq (2.47) and for the new electric field, $\mathbf{E}$, using Eq (2.49). This is described further in Section 3.4.

6. Check convergence criteria. Compare the maximum absolute value of the difference between new and old values of the potential until they fall below a given threshold (i.e. $\max |\phi_{\text{new}} - \phi_{\text{old}}| \leq \epsilon \times \max |\phi_{\text{new}}|$, for some small value ϵ). If the model has not converged, then mix the new and old values for potential using Anderson Mixing [60] or simple mixing.

7. Repeat Steps 3 – 6 until convergence is achieved.

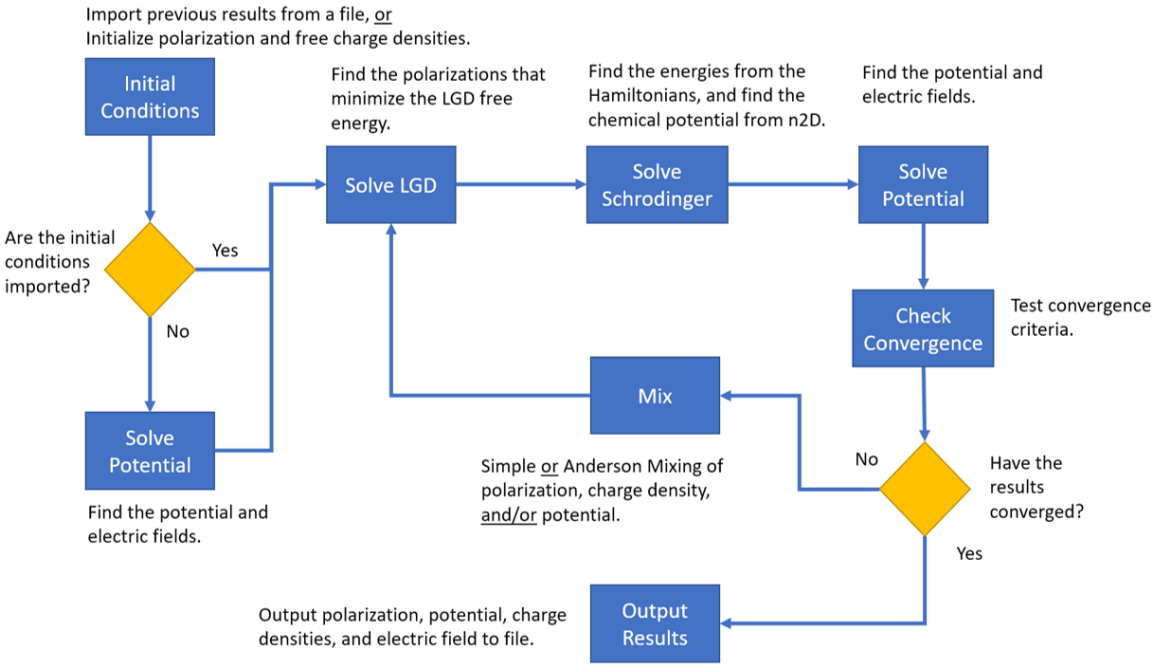

Figure 3.1: Flowchart describing the computational algorithm.

3.1 Discretization

We employ two off-set, interleaved lattices as illustrated in Fig 3.2. The electron (or charge) density and the potential are defined on the first (or primary) lattice, and the polarization and electric field are defined on the second. The two lattices arise naturally from the relationship between the the charge density and polarization (i.e. $\rho^b = -\nabla \cdot \mathbf{P}$), or the potential and electric field (i.e. $\mathbf{E} = -\nabla\phi$). Consider Eq (2.49),

$$\begin{aligned} \mathbf{E} &= -\nabla\phi \\ \Rightarrow E_x &= -\frac{\partial\phi}{\partial x} \\ &= -\left[\frac{\phi(x+\Delta x)-\phi(x)}{\Delta x}\right], \end{aligned} \tag{3.1}$$

where the last line is a discrete derivative over the lattice spacing Δx. Geometrically, it is natural to associate E_x with the intermediate point $x + \frac{1}{2}\Delta x$. Since we take our discrete derivatives in two dimensions, the electric field, $\mathbf{E} = (E_x, E_z)$, lies naturally at the mid-points between the primary lattice points. This defines the secondary lattice. Similarly, the equation $\rho^b = -\nabla \cdot \mathbf{P}$ maps the polarization on the secondary lattice onto bound charge densities on the primary.

We overlay our lattices on our physical model so that the primary lattice coincides with the edges of the ferroelectric at the bottom, and the polar cap at the top [see Fig 3.3]. The secondary lattice is offset by one-half lattice width in the x- and z-directions, and has one f row of lattice points along the z-axis. We remark that the electric field and potential are defined in both the ferroelectric and the polar cap, but the ferroelectric polarization and the free charge densities are only defined within the ferroelectric itself.

There is a microscopic gap between the capacitor plate and the ferroelectric at the bottom, and the capacitor plate and the polar cap at the top. This ensures that there is no transfer of free electrons between the capacitor plates and ferroelectric or polar cap.

To transition from our continuum to discrete model, we evaluate our variables at the points $\mathbf{r}_i$ which correspond with the lattice point i. Their values approximate the values near that point.

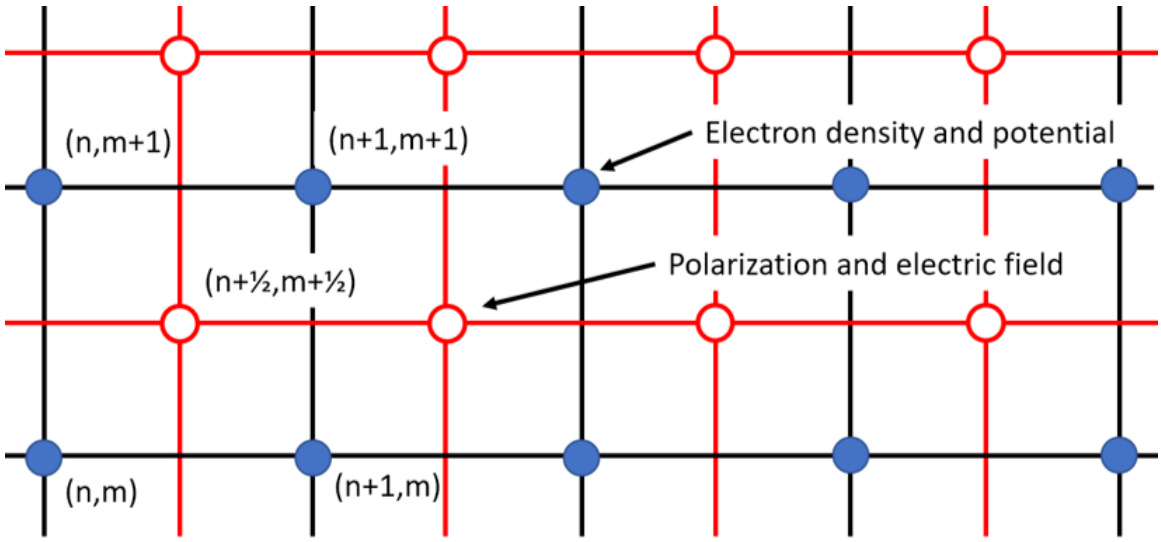

Figure 3.2: Interleaved lattices. The electron density and potential are evaluated at the blue points denoted (n, m). The electric field and polarization are evaluated at the red points denoted $(n + \frac{1}{2}, m + \frac{1}{2})$. The grid of blue points is called the primary lattice. The grid of red points is called the secondary lattice.

3.2 Initial Conditions

The closer the initial condition is to the final result, the more likely (and quickly) the algorithm will converge. Wherever possible, we used existing solutions for some n_{2D} as the initial guess for a nearby value of n_{2D}. When unavailable, any combination of polarization, electron density, or potential could be used to initialize the model. In practice, when not importing results from previous runs, we initialized the polarization, left the electron density equal to zero, and then solved for an initial potential and electric fields. The free charge distribution was obtained from solutions of the coarse-grained Hamiltonians and a given n_{2D}. Over successive cycles, the feedback resulted in self-consistent values. We used several different approaches for generating an initial distribution of values for polarization and/or charge density. The Initialize module responsible for initializing the computational model is discussed in detail in Appendix B.

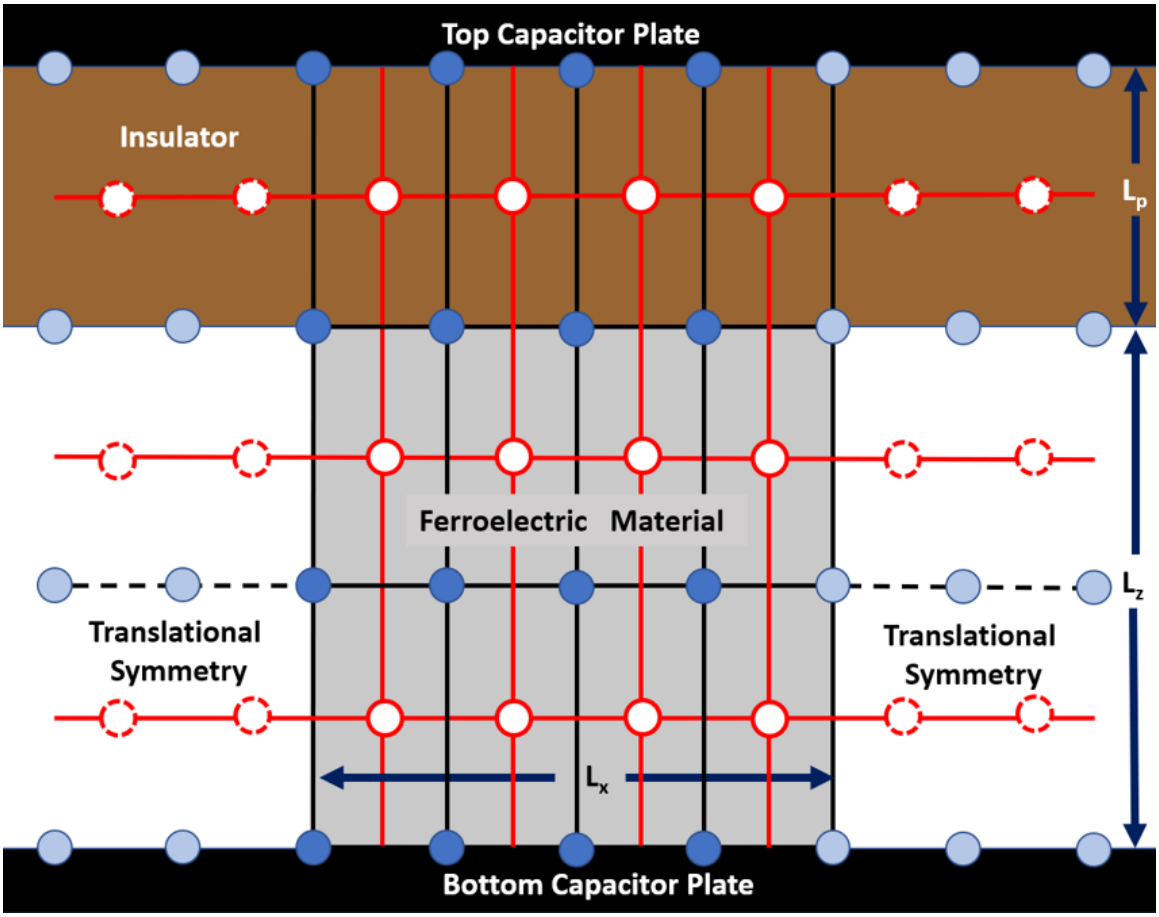

Figure 3.3: The primary lattice aligns with the edge of the ferroelectric material in the x- and z-directions. Along the x-axis, we have translational symmetry. i.e. $\mathbf{P}(x,z) = \mathbf{P}(x+nL_x, z)$ for all $n \in \mathbb{Z}$.

3.3 Solving for the Polarization

We used the Galerkin-Newton Gradient Algorithm (GNGA) discussed in Ref [59] to mininize the free energy equation, $\mathcal{F}$, for P_x and P_z. The paper's algorithm has been adapted to our system as follows.

For each lattice point i and $\eta \in \{x, z\}$,

1. Calculate

$$g_{i,\eta} = \frac{\delta \mathcal{F}}{\delta P_{i,\eta}} \tag{3.2}$$

where $g_{i,\eta}$ is given by Eqs (2.13) and (2.14).

2. Calculate the Hessian,

$$A_\eta = \begin{bmatrix} \frac{\delta^2 \mathcal{F}}{\delta P_{1,\eta}^2} & \frac{\delta^2 \mathcal{F}}{\delta P_{1,\eta} \delta P_{2,\eta}} & \cdots & \frac{\delta^2 \mathcal{F}}{\delta P_{1,\eta} \delta P_{N,\eta}} \\ \vdots & \ddots & & \vdots \\ \vdots & & \ddots & \vdots \\ \frac{\delta^2 \mathcal{F}}{\delta P_{N,\eta} \delta P_{1,\eta}} & \frac{\delta^2 \mathcal{F}}{\delta P_{N,\eta} \delta P_{2,\eta}} & \cdots & \frac{\delta^2 \mathcal{F}}{\delta P_{N,\eta}^2} \end{bmatrix} \tag{3.3}$$

   This is an $(N_x \times N_z)^2$ matrix where N_x, N_z are the number of lattice cells in the x and z-directions respectively of the ferroelectric.

3. Compute the matrix, χ_η satisfying

$$\chi_\eta = A_\eta^{-1} g_\eta \tag{3.4}$$

   where g_η is a column vector made up of the $g_{i,\eta}$ from above.

4. Set $P_{i,\eta}^{\text{new}} = P_{i,\eta}^{\text{old}} - \delta \chi_{i,\eta}$ for some small fixed value δ. We used $\delta = 0.5$ but it can be adjusted to change the level of mixing.

5. Calculate $\Delta = \max |\chi_{i,\eta}|$.

6. The iterative code is converged when $\Delta < \epsilon \approx 1 \times 10^{-8}$. If $\Delta > \epsilon$, then repeat from Step 1.

We use a finite difference approximation for our derivatives. For notational simplicity, we will adopt the shorthand of $(n', m') = (n + \frac{1}{2}, m + \frac{1}{2})$. We approximate the derivative of the polarization, P_x, by

$$\frac{\partial P_x}{\partial x}(n, m') = \frac{P_{(n',m'),x} - P_{(n'-1,m'),x}}{\Delta x} \tag{3.5}$$

$$\frac{\partial P_x}{\partial z}(n', m) = \frac{P_{(n',m'),x} - P_{(n',m'-1),x}}{\Delta z}, \tag{3.6}$$

and the second derivative as:

$$\frac{\partial P_x^2}{\partial x^2}(n',m') = \frac{P_{(n'+1,m'),x} + P_{(n'-1,m'),x} - 2P_{(n',m'),x}}{(\Delta x)^2} \tag{3.7}$$

$$\frac{\partial P_x^2}{\partial z^2}(n',m') = \frac{P_{(n',m'+1),x} + P_{(n',m'-1),x} - 2P_{(n',m'),x}}{(\Delta z)^2}. \tag{3.8}$$

The selection of the locations on the left-hand-side of the Eqs (3.5) – (3.8) is deliberate. We want to highlight that the first order derivatives change lattices, while the second order derivatives stay on the same lattice.

Combining these results, we arrive at equations for the functional derivatives on the secondary lattice,

$$\begin{aligned}\frac{\delta \mathcal{F}}{\delta P_{(n',m'),x}} =& P_{(n',m'),x}\left[a_1 + b|\mathbf{P}_{(n',m'),x}|^2 + b' P_{(n',m'),z}^2 + \frac{1}{\epsilon_0}\right] \\ &- g_{11}\left(\frac{P_{(n'+1,m'),x} + P_{(n'-1,m'),x} - 2P_{(n',m'),x}}{(\Delta x)^2}\right) \\ &- g_{44}\left(\frac{P_{(n',m'+1),x} + P_{(n',m'-1),x} - 2P_{(n',m'),x}}{(\Delta z)^2}\right) \\ &- \frac{1}{\epsilon_0} D_{(n',m'),x},\end{aligned} \tag{3.9}$$

and,

$$\begin{aligned}\frac{\delta \mathcal{F}}{\delta P_{(n',m'),z}} =& P_{(n',m'),z}\left[a_3 + b|\mathbf{P}_{(n',m'),x}|^2 + b' P_{(n',m')}^2 + \frac{1}{\epsilon_0}\right] \\ &- g_{44}\left(\frac{P_{(n'+1,m'),z} + P_{(n'-1,m'),z} - 2P_{(n',m'),z}}{(\Delta x)^2}\right) \\ &- g_{11}\left(\frac{P_{(n',m'+1),z} + P_{(n',m'-1),z} - 2P_{(n',m'),z}}{(\Delta z)^2}\right) \\ &- \frac{1}{\epsilon_0} D_{(n',m'),z}.\end{aligned} \tag{3.10}$$

Fortunately, Eqs (3.9) and (3.10) only contain lattice points $(n',m'),(n' \pm 1,m')$, and $(n',m' \pm 1)$. This greatly simplifies the Hessian matrix because the only non-zero terms for $\frac{\delta^2 \mathcal{F}}{\delta P_{i,\eta} \delta P_{j,\eta}}$ will be $i = j$, or when i and j adjacent to each other along the x- or z-axis.

Across the the top and bottom boundaries of the ferroelectric, we imposed $\frac{\partial P_x}{\partial z} = 0$ and $\frac{\partial P_z}{\partial z} = 0$ [see Eqs (2.4) and (2.5)]. Even though the polarization is not defined in

the capacitor or the polar cap, we pretend that there exists $P_{(n',m'+1),x} = P_{(n',m'),x}$ and $P_{(n',m'+1),z} = P_{(n',m'),z}$ whenever m is along the top boundary of the ferroelectric, and $P_{(n',m'-1),x} = P_{(n',m'),x}$ and $P_{(n',m'-1),z} = P_{(n',m'),z}$ when m is along the bottom boundary of ferroelectric.

Taking the second order functional derivatives, we obtain the solution away from the interface,

$$\frac{\delta^2\mathcal{F}}{\delta P^2_{(n',m'),x}} = a + 3bP^2_{(n',m'),x} + (b+b')P^2_{(n',m'),z} + \frac{1}{\epsilon_0} + \frac{2g_{11}}{(\Delta x)^2} + \frac{2g_{44}}{(\Delta z)^2}, \tag{3.11}$$

and a second equation along the interface,

$$\frac{\delta^2\mathcal{F}}{\delta P^2_{(n',m'),x}} = a + 3bP^2_{(n',m'),x} + (b+b')P^2_{(n',m'),z} + \frac{2g_{11}}{(\Delta x)^2} + \frac{g_{44}}{(\Delta z)^2}. \tag{3.12}$$

Fortunately, the off-diagonal terms are unaffected by the interface, and

$$\frac{\delta^2\mathcal{F}}{\delta P_{(n',m'),x}\delta P_{(n'\pm1,m'),x}} = -\frac{g_{11}}{(\Delta x)^2}, \tag{3.13}$$

$$\frac{\delta^2\mathcal{F}}{\delta P_{(n',m'),x}\delta P_{(n',m'\pm1),x}} = -\frac{g_{44}}{(\Delta z)^2}. \tag{3.14}$$

For P_z, we similarly obtain the bulk equation,

$$\frac{\delta^2\mathcal{F}}{\delta P^2_{(n',m'),z}} = a + 3bP^2_{(n',m'),z} + (b+b')P^2_{(n',m'),x} + \frac{2g_{11}}{(\Delta z)^2} + \frac{2g_{44}}{(\Delta x)^2}, \tag{3.15}$$

and interface equation,

$$\frac{\delta^2\mathcal{F}}{\delta P^2_{(n',m'),z}} = a + 3bP^2_{(n',m'),z} + (b+b')P^2_{(n',m'),x} + \frac{g_{11}}{(\Delta z)^2} + \frac{2g_{44}}{(\Delta x)^2}. \tag{3.16}$$

The off-diagonal Hessian terms become

$$\frac{\delta^2\mathcal{F}}{\delta P_{(n',m'),z}\delta P_{(n'\pm1,m'),x}} = -\frac{g_{11}}{(\Delta x)^2}, \tag{3.17}$$

$$\frac{\delta^2\mathcal{F}}{\delta P_{(n',m'),z}\delta P_{(n',m'\pm1),x}} = -\frac{g_{44}}{(\Delta z)^2}. \tag{3.18}$$

These equations allow us to computationally solve Steps (1) and (2) of the GNGA algorithm. Step (3) can be solved using standard techniques in linear algebra. We used the well-known Basic Linear Algebra Subprogram (BLAS) and Linear Algebra PACKage (LAPACK) libraries for access to common subroutines. Steps (4) – (6) are straightforward to implement.

3.4 Solving for the Potential

The scalar potential, $\phi(\mathbf{r})$, is related to the total charge density, $\rho^{\text{total}}(\mathbf{r})$, by Poisson's Equation,

$$\begin{aligned} -\epsilon_0 \nabla^2 \phi(\mathbf{r}) =& \rho^{\text{total}}(\mathbf{r}) \\ =& \rho^b(\mathbf{r}) + \rho^f(\mathbf{r}), \end{aligned} \tag{3.19}$$

where $\rho^b(\mathbf{r})$ and $\rho^f(\mathbf{r})$ are the bound, and free charge densities respectively. Any external charge density is accounted for in our boundary conditions for the potential [see Eqs (2.8) and (2.9)].

The bound charge density, $\rho^b(\mathbf{r})$, was given by Eq (3.20). For the total polarization, this is

$$\begin{aligned} \rho^b(\mathbf{r}) =& -\nabla \cdot [\mathbf{P} + \epsilon_0 \chi(\mathbf{r}) \mathbf{E}(\mathbf{r})] \\ =& -\left[\frac{\partial \left(P_x(\mathbf{r}) + \epsilon_0 \chi(\mathbf{r}) E_x(\mathbf{r}) \right)}{\partial x} + \frac{\partial \left(P_z(\mathbf{r}) + \epsilon_0 \chi(\mathbf{r}) E_z(\mathbf{r}) \right)}{\partial z} \right]. \end{aligned} \tag{3.20}$$

Since we are taking first order derivatives in only one dimension, we obtain a term that is not on either lattice [see Eq (3.5)]. To approximate it properly, we bracket its value from either side. For instance,

$$\begin{aligned} \frac{\delta P_x}{\partial x}(n, m') &= \frac{P_{(n',m'),x} - P_{(n'-1,m'),x}}{\Delta x}, \\ \frac{\delta P_x}{\partial x}(n, m'-1) &= \frac{P_{(n',m-1'),x} - P_{(n'-1,m-1'),x}}{\Delta x}, \end{aligned}$$

where $(n,m) = \frac{1}{2}[(n,m') + (n,m'-1)]$, then

$$\Rightarrow \frac{\delta P_x}{\partial x}(n,m) = \frac{1}{2\Delta}\Big[P_{(n',m'),x} - P_{(n'-1,m'),x} + P_{(n',m'-1),x} - P_{(n'-1,m'-1),x}\Big]. \tag{3.21}$$

Since P_η and E_η are defined on the secondary lattice, we approximate their derivatives on the primary lattice as

$$\begin{aligned}\frac{\partial\left(P_x + \epsilon_0\chi E_x\right)}{\partial x}(n,m) = \frac{1}{2\Delta x}\Big[&P_{(n',m'),x} - P_{(n'-1,m'),x} \\ &+ P_{(n',m'-1),x} - P_{(n'-1,m'-1),x} \\ &+ \epsilon_0\left[\chi_{(n',m')}E_{(n',m'),x} - \chi_{(n'-1,m)}E_{(n'-1,m'),x}\right] \\ &+ \epsilon_0\left[\chi_{(n',m'-1)}(E_{(n',m'-1),x} - \chi_{(n'-1,m'-1)}E_{(n'-1,m'-1),x}\right]\Big],\end{aligned} \tag{3.22}$$

with a similar result in the z-direction.

We approximate the second derivative of the potential by

$$\frac{\partial^2\phi}{\partial x^2}(n,m) = \frac{\phi_{(n+1,m)} + \phi_{(n-1,m)} - 2\phi_{(n,m)}}{(\Delta x)^2}, \tag{3.23}$$

$$\frac{\partial^2\phi}{\partial z^2}(n,m) = \frac{\phi_{(n,m+1)} + \phi_{(n,m-1)} - 2\phi_{(n,m)}}{(\Delta z)^2}, \tag{3.24}$$

where Δx and Δz are the lattice spacing in the x and z-directions respectively. Unlike the polarization, we do not need to worry about the interfaces with the capacitor plates because our boundary conditions set our values at these points.

Combining Eqs (3.19) and (3.24), we obtain

$$\frac{\phi_{(n+1,m)} + \phi_{(n-1,m)} - 2\phi_{(n,m)}}{(\Delta x)^2} + \frac{\phi_{(n,m+1)} + \phi_{(n,m-1)} - 2\phi_{(n,m)}}{(\Delta z)^2} = -\frac{1}{\epsilon_0}\rho^f_{(n,m)} - \frac{1}{\epsilon_0}\rho^b_{(n,m)}. \tag{3.25}$$

We solve this equation using the *relaxation method*, described below:

1. Define a new equation for $\phi^*_{(n,m)}$ by re-arranging Eq (3.25) for $\phi_{(n,m)}$. Taking $\Delta x = \Delta z = \Delta$, set

$$\phi^*_{(n,m)} = \frac{1}{4}\Bigg\{ \phi_{(n+1,m)} + \phi_{(n-1,m)} + \phi_{(n,m+1)} + \phi_{(n,m-1)} + \frac{\Delta^2}{\epsilon_0}\left[\rho^f_{(n,m)} + \rho^b_{(n,m)}\right] \Bigg\} \tag{3.26}$$

2. Calculate $\Delta = \max |\phi^*_{(n,m)} - \phi_{(n,m)}|$.

3. For $\epsilon \approx 10^{-8} - 10^{-12}$, if $\Delta < \epsilon \times \max |\phi|$, then we have converged. Otherwise, set $\phi_{(n,m)} = \phi^*_{(n,m)}$ for all (n, m), and repeat from Eq (3.26).

Once obtained, we solve for the electric field, **E** using a discrete version of Eq (2.49).

3.5 Solving for the Free Charge Densities

Eq (2.66) gives us the entries of the coarse-grained Hamiltonians for the different t_{2g} orbitals. We solve them computationally using standard libraries for determining eigenvalues and eigenvectors of Hermitian matrices. This is discussed further in Appendix B.

We remark that our Hamiltonian has dimensions of $N_x N_z \times N_x N_z$, where N_x and N_z are the number of lattice points along each dimension of the ferroelectric. In order to index lattice positions in the Hamiltonian, we need to translate between our two-dimensional lattice index (n, m) and a one-dimensional lattice index $i \in [1, N_x N_z]$. We used the mapping

$$i = n + (m-1)N_x. \tag{3.27}$$

Under this mapping, if $i = n + (m-1)N_x$ and $j = n' + (m'-1)N_x$, then the matrix hopping element at (i, j) in the Hamiltonian corresponds with the transition from (n, m) to (n', m').

To determine the free charge density, we find the chemical potential, μ, for a fixed 2D charge density using Eq (2.44). For a given n_{2D}, this becomes

$$n_{2D} = \frac{2a^2}{L_x L_y} \sum_\alpha \sum_n \sum_k f(\epsilon_{n\alpha} + \epsilon(k)) \tag{3.28}$$

where a is the lattice constant, $\epsilon_{n\alpha}$ is the n^{th} eigenenergy for orbital type α, and $\epsilon(k)$ is the energy corresponding with the wavenumber k along the y-axis. We solve this using the *bisection method*. We bracket the value of the chemical potential with the largest eigenvalue on top, and the smallest eigenvalue minus k_BT on the bottom, and iterate until our calculated n_{2D} is is within $10^{-8} - 10^{-12}$ of n_{2D}. Once the potential is obtained, we calculate the free charge density on the lattice using a discrete version of Eq (2.45).

3.6 Summary

This chapter summarized the discrete equations used to solve each step of the computational model. Variations of these equations were attempted during testing to see if they led to faster convergence, but were ultimately discarded in favour of the above. Understanding the dual lattices, algorithms, and complexities of the boundary conditions is essential for readers intending to replicate this model, or portions thereof.

Chapter 4

Results and Analysis

In the introduction, we highlighted two broad questions we wanted to investigate:

1. How does the electron density, n_{2D}, affect the domain wall?
2. How do the t_{2g} orbitals and the domain wall interact?

We will tackle these questions as follows:

1. Examine the shape of the domain wall for different values of n_{2D}. We will compare our results with those published in Ref [1]. The model in Ref [1] uses the same algorithms and techniques discussed in Chapters 2 and 3, but only has a single, isotropic orbital per unit cell. We will refer to this model as the *isotropic model*, and our model as the *anisotropic model*. We will find that the results are qualitatively similar, but quantitatively distinct. These differences must be related to the t_{2g} orbitals.
2. Examine the bound charge density and free charge densities. We will find that the domain wall is positively charged, and is almost fully-compensated by the free electrons.
3. Examine the near charge neutrality of the domain wall. We will find that the surface polarization of the ferroelectric can be determined from the requirement to fully compensate the n_{2D}. This implies that our ferroelectric is nearly charge neutral.
4. Examine the electric fields. We will find weak depolarizaing fields that only extend ~ 10 nm away from the domain wall.

5. Examine the orbital selectivity. We will find that the relative orientations of the orbital planes (e.g., d_{xy} has an x-y orbital plane) and the domain wall affect the charge concentrations in each orbital type. We will argue that this is related to the kinetic energy of the electrons, and explains the quantitative differences for the tilt of the domain wall between the isotropic and anisotropic models.

4.1 Polarization

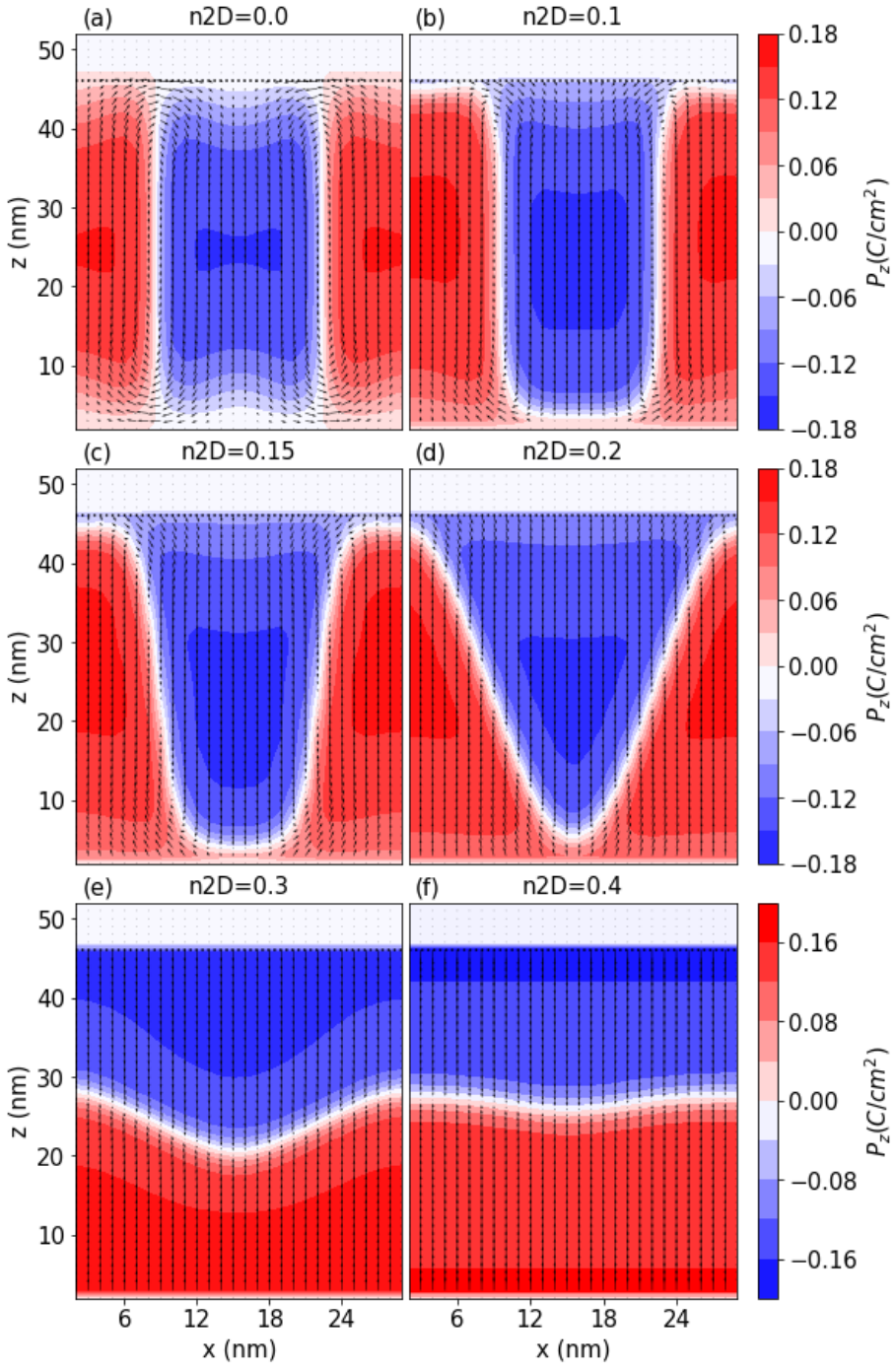

Figure 4.1: Polarization for the anisotropic model for different n_{2D}. These figures represent the polarization along a cut through the model in the x-z plane. The arrows represent the orientation and magnitude of the polarization vector. The colour is determined by the value of the polarization component along the z-axis (P_z). (a) We have the expected vertical 180° (or Kittel) domains when there are no electrons present ($n_{2D} = 0.0$). (b) - (f) As n_{2D} increases, the domain walls tilt towards the horizontal. This becomes especially pronounced when $n_{2D} \geq 0.3$.

In Fig 4.1, we present the polarizations across the ferroelectric for different values of n_{2D}. The arrows represent the direction of the polarization, while the color is based on the z-component of polarization, P_z. We will examine the shape of the domain wall as a function of n_{2D}, compare them against the isotropic model, and consider their widths. For convenience, we will denote the positive end of the domain to be the region towards which the polarization is pointing.

When there are no free electrons present, we observe the well-known 180^o domains with vertical domain walls [see Fig 4.1, (a)]. The so-called Kittel domains minimize the energy because the alternating domains lead to concentrations of bound charge along the interface with alternating signs. The electric fields extend between adjacent charge centres along the surfaces, instead of stretching across the bulk. This leaves the bulk ferroelectric isolated from the electric fields generated by the bound charge along the boundary [see Fig 4.8, (a)] [50].

As n_{2D} increases, the positive ends of the domains begin to shrink. In Fig 4.1 (b), $n_{2D} = 0.1$, and there is a clear separation between the positive ends of the domains, and the interfaces. The region in white is the domain wall. We denote the arms of the domain wall to mean the regions of the domain wall stretching between the positive ends of two adjacent domains. The arms of the domain wall are nearly vertical, with minor curvature where they intersect with the positive ends of the domain.

In Fig 4.1 (c), $n_{2D} = 0.15$, and the positive ends of the domains have shrunk further, causing the arms of the domain walls to tilt noticeably away from the vertical. The positive ends of the domains also move incrementally away from the interface.

By $n_{2D} = 0.2$, the positive ends of the domains are more readily described as vertices since they are no longer flat. The arms of the domain wall have tilted further away from the vertical, and the domain wall is noticeably detached from the interface [see Fig 4.1, (d)]. This domain wall is referred to as a *zig-zag* domain wall due to its shape.

The difference between $n_{2D} = 0.2$ and 0.3 is stark. The domain wall for the latter is very nearly horizontal. There remains a vertex, but it is less sharp than earlier, and the domain wall occupies the center of the ferroelectric, far away from the interfaces [see Fig 4.1, (e)]. By $n_{2D} = 0.4$, the flattening of the domain wall is nearly complete, and the vertex

is almost subsumed into the arms of the domain wall [see Fig 4.1, (f)].

Overall, we see that for increasing n_{2D}, the positive ends of the domains shrink, and the arms of the domain walls tilt away from the vertical. For values of $n_{2D} \gtrsim 0.3$, the domain wall is almost horizontal, and we have a 180° head-to-head charged domain wall [see Fig 1.2, (b)].

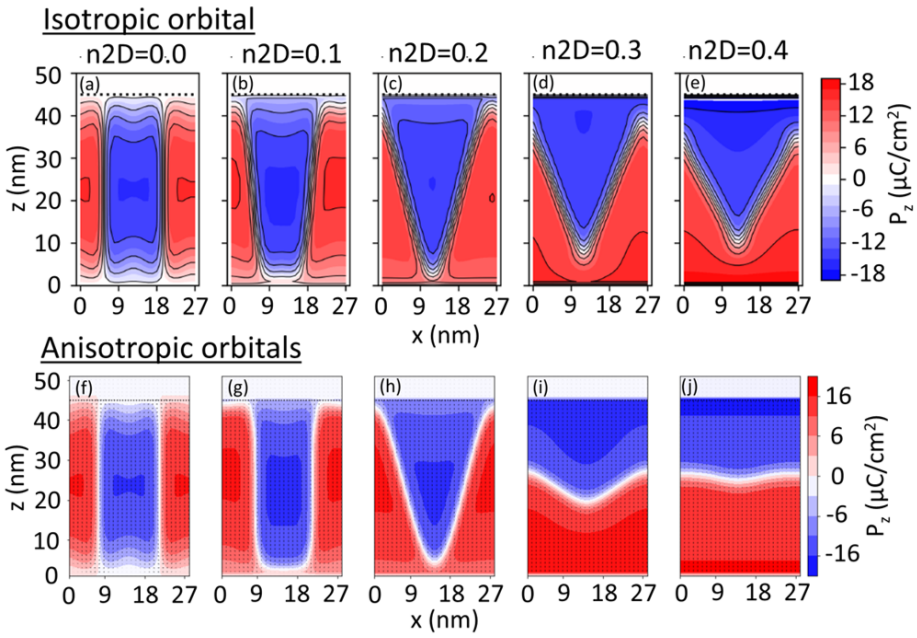

Figure 4.2: Comparison of polarization between the isotropic and anisotropic orbitals. These figures represent the polarization along a cut through the model parallel to the x-z plane. The colour is determined by the value of the polarization component along the z-axis (P_z). (a) – (e) This collection of figures corresponds with the isotropic orbital. It is reprinted with permission from [1]. As n_{2D} increases, the domain walls tilt towards the horizontal, eventually separating from the interface when $n_{2D} \geq 0.2$. (f) – (j) This collection of figures is for the anistropic model. Compared with (a) – (e), the domain wall remains more vertical at $n_{2D} = 0.1$, looks similar at $n_{2D} = 0.2$, and is much more horizontal for $n_{2D} \geq 0.3$.

In Fig 4.2, we contrast this behaviour with the isotropic model. The same relationship is observed between increasing n_{2D} and increasing tilt of the domain wall in the isotropic model, as well. However, the rate at which the domain wall tilts is noticeably different in the two models. At $n_{2D} = 0.1$, the domain wall in the anisotropic model is steeper than the isotropic model [see Figs 4.2, (b) and (g)]. At $n_{2D} = 0.2$, both models look the same [see Figs 4.2, (c) and (h)]. For $n_{2D} \geq 0.3$, the domain wall is noticeably more horizontal in the anisotropic model [see Figs 4.2, (d) – (e) and (i) – (j)]. This suggests that the tilting of the

domain wall is a feature of overall free charge density, regardless of the orbitals they occupy. However, it is clear that the presence of multiple anisotropic bands in the anisotropic model influences the rate at which the domain wall tilts. Specifically, the domain walls tilts more slowly for $n_{2D} \leq 0.2$, and more quickly for $n_{2D} \geq 0.2$ compared with the isotropic model.

4.2 Domain Wall Width

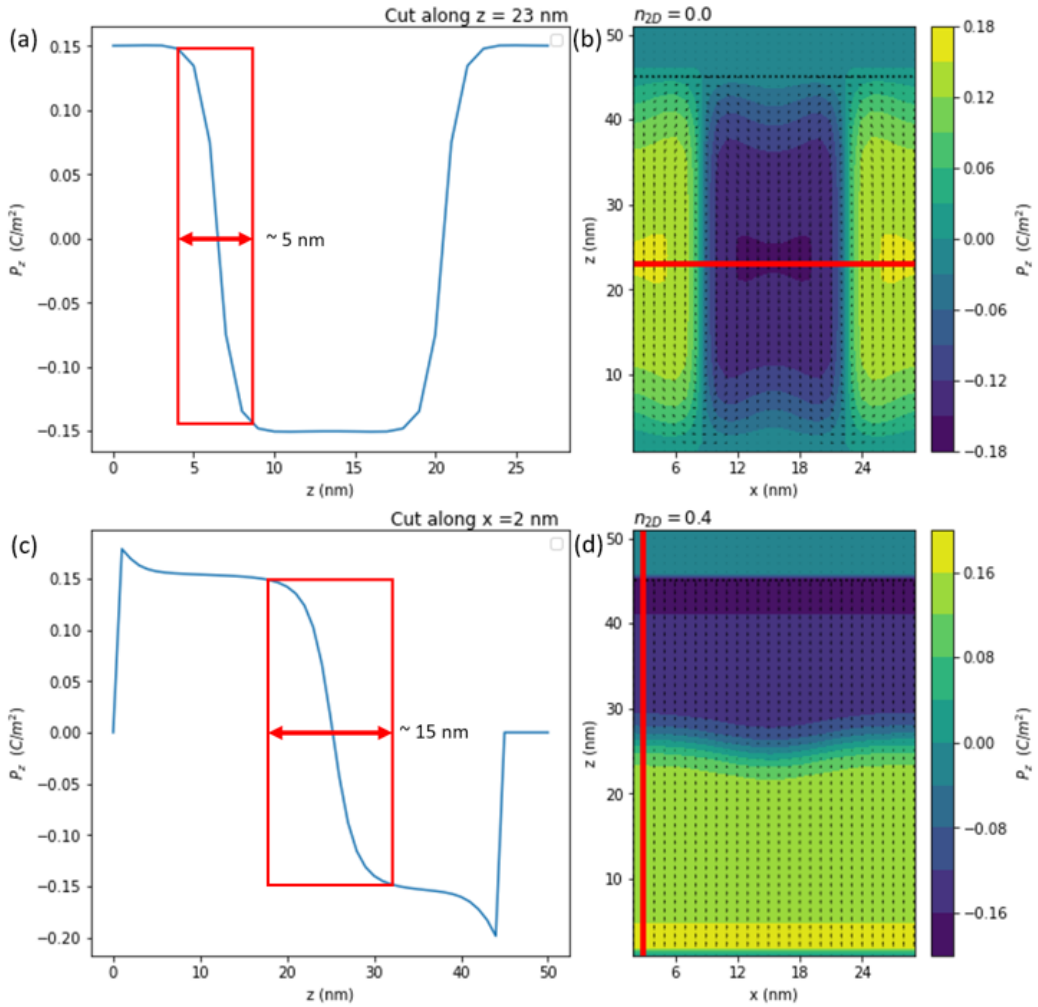

Figure 4.3: Widths of neutral and charged domain walls. (a) The P_z component of polarization along $z = 23$ nm for $n_{2D} = 0.0$. This position is chosen because the horizontal line is perpendicular to the domain wall. The width is ~ 5 nm. (b) A representation of the cut with respect to position in the ferroelectric. The color is determined by the value of P_z. (c) The P_z component of polarization along $x = 2$ nm for $n_{2D} = 0.4$. We chose this position because the vertical line is perpendicular to the domain wall. The width is ~ 15 nm. (d) A representation of the cut with respect to position in the ferroelectric. The color is determined by the value of P_z.

The width of the domain wall depends on whether it is neutral or charged [5, 7, 24]. For $n_{2D} = 0$, the domain wall is neutral and vertical, and it is easy to look at the change in polarization along a cut for a fixed value of z. In Fig 4.3 (a), we see that the width of the neutral domain wall is $\lesssim 5$ nm. The charged domain wall is more challenging because we cannot easily take a line perpendicular to the orientation of the wall. However, for $n_{2D} = 0.4$, the wall is very close to horizontal, and we estimate the domain width where the wall is nearly flat. In Fig 4.3 (c), the width of the charged domain wall is $\lesssim 15$ nm. These values are high compared to the literature (1 – 10 nm [5, 7, 24]), but there is no consensus on the criteria by which the domain wall width is determined (e.g. 95% of bulk polarization), so our values are not unreasonable for upper bounds. Moreover, they agree with the observation that neutral domain walls are narrower than charged domain walls by approximately an order of magnitude in perovskites [7].

4.3 Charge Distribution

We turn our attention to the charge density across the ferroelectric. This consists of bound charge generated by the polarization, and free electrons determined by n_{2D}. We begin by examining the bound charge generated by the polarization at the interfaces and across the domain wall. We will observe that the polarization generates a positive bound charge along the domain wall which is consistent with a head-to-head domain wall. We will find that the free electrons become concentrated along the domain wall, compensating $\sim 99\%$ of the bound charge, and leaving a small, residual positive charge along the domain wall.

The gradient of polarization gives rise to the bound charge [see Eq (2.48)]. Within the ferroelectric, the polarization changes sharply along the interfaces, and across the domain wall. At the interfaces, the change in polarization is abrupt due to the boundary conditions, and we obtain a band of negative bound charge confined along the row of adjacent lattice points [see Figs A.2 – A.6, (e)]. At the domain wall, the polarization meets head-to-head along the z-axis, and we observe a positive bound charge along the domain wall [see Fig 4.5].

By design, our selection of $a_1 > 0$ and $a_3 < 0$ in Eqs (2.13) and (2.14) led to the

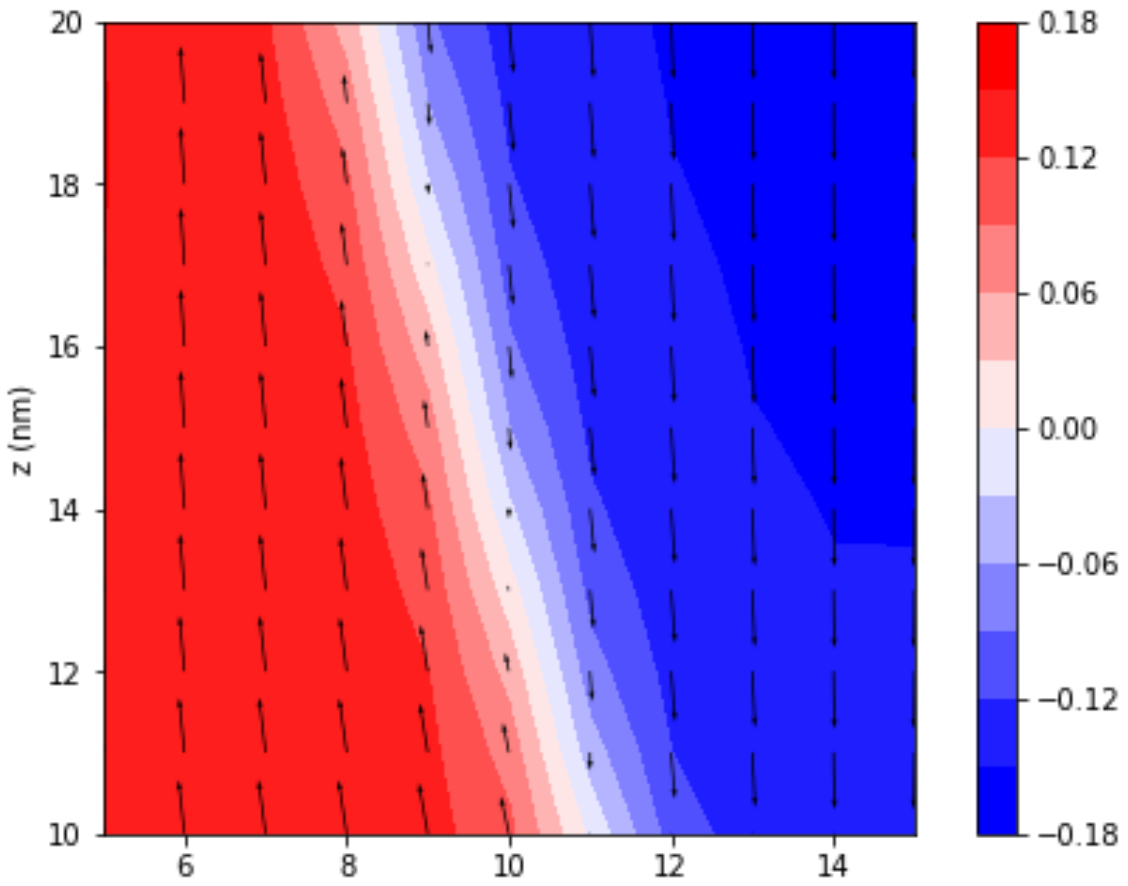

Figure 4.4: Polarization near the domain wall for $n_{2D} = 0.2$ between $5 \leq x \leq 15$ and $10 \leq z \leq 20$. The ratio of x:z is 1:1 so that the orientation of the vector is scaled correctly. The colour is determined by the polarization component along the z-axis (P_z). The length of the polarization vector has been exaggerated for ease-of-reading. The polarization vector rotates to lie roughly parallel to the domain wall as it approaches, and before it shrinks to zero length.

emergence of polarization along z-axis, but not the x-axis. We find that P_z is typically an order of magnitude larger than P_x across the ferroelectric. Consequently, we expect that the bound charge arising from the change in P_z, denoted ρ_z^b, will be larger than the bound charge generated by the change in P_x, denoted ρ_x^b. These axial bound charge densities are given by

$$\rho_x^b = -\frac{\partial P_x}{\partial x}, \tag{4.1}$$

$$\rho_z^b = -\frac{\partial P_z}{\partial z}, \tag{4.2}$$

where the total bound charge in Eq (2.48) can be re-written as

$$\rho^b = \rho^b_x + \rho^b_z. \tag{4.3}$$

We observe very slight rotation of the polarization adjacent to the domain wall across all values of n_{2D}. (e.g., see Fig 4.4 for $n_{2D} = 0.2$.) This generates a small bound charge contribution from P_x. When the domain wall is vertical, there is no domain wall for P_z to cross, so it contributes nothing to the bound charge. In fact, for low values of $n_{2D} \lesssim 0.15$, the bound charge density arising from P_x is of the same order as that generated from P_z [see Fig 4.5]. Moreover, the bound charge from the P_x component is negative, cancelling the positive bound charge generated from P_z. This reduces the net bound charge at the domain wall.

In the case of the Kittel domains [see Fig 4.5, (a) – (c)], the charge densities arising from P_x and P_z are nearly equal and opposite in the bulk of the ferroelectric, leaving only a narrow, alternating, band of charge along the interface. Since the Kittel domains are the stable solution for polarization whenever $n_{2D} = 0.0$, this suggests that a bound charge from P_x is always present and important when the electron density is very low, regardless of a_1. As n_{2D} increases, the charge contribution from P_x continues to play a role, reducing the net bound charge density in the arms of the domain walls [see Fig 4.5, (d) – (f)]. However, as the arms of the domain wall tilt further, the contribution to the bound charge density from P_x decreases relative to P_z. By $n_{2D} = 0.2$, the magnitude of the contributions differ by an order of magnitude. This increases to two orders of magnitude by $n_{2D} = 0.3$ and beyond. We conclude that although P_x is generally an order of magnitude smaller than P_z, we cannot discount its contribution to the bound charge when the domain wall is close to vertical, which corresponds with n_{2D} being small.

Having considered the bound charge, we turn our attention to the free charge density made up of contributions from each of the three orbital types. We will begin by considering the total charge density, $\rho^{\text{total}} = \rho^{\text{free}} + \rho^{\text{bound}}$. In Fig 4.6, we observe near complete charge cancellation across the domain wall for all values of n_{2D} . We find that the bound charge is compensated by the free charge to $\sim 99\%$. There is a small, residual, and positive charge

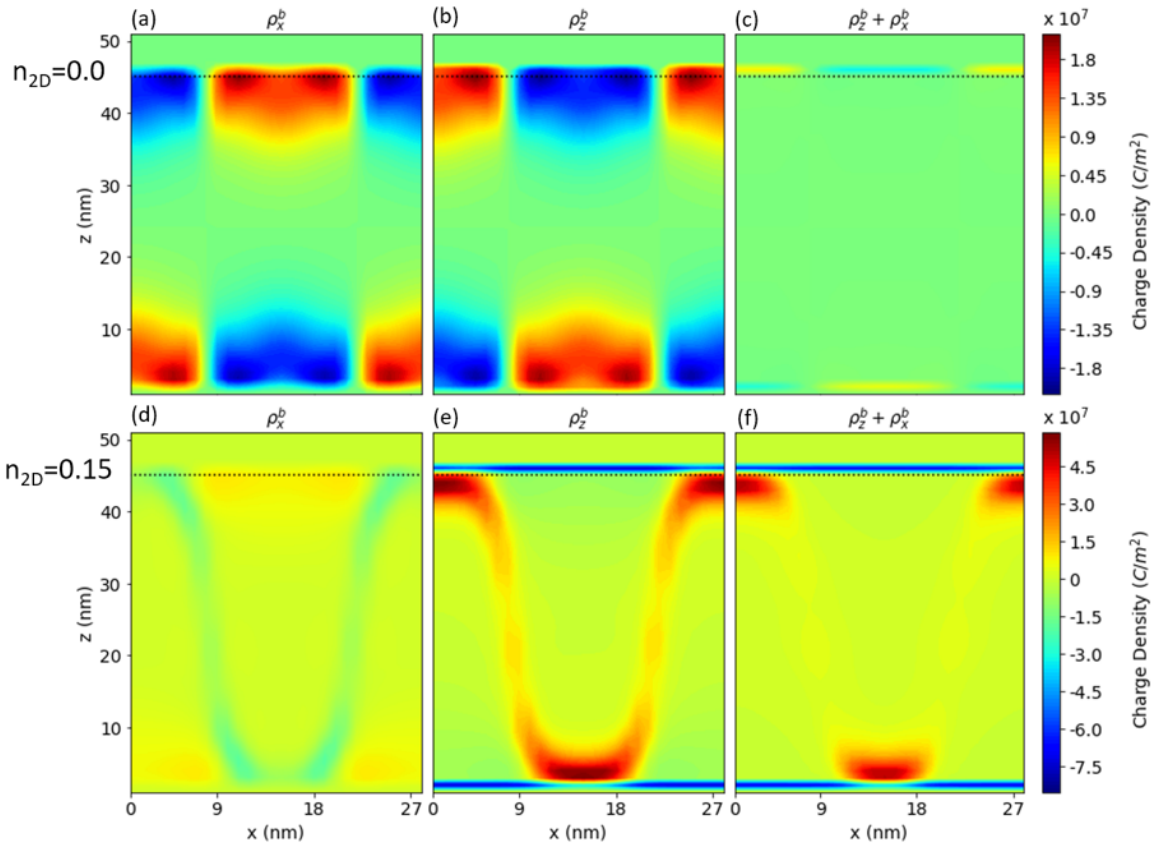

Figure 4.5: Bound charge densities. (a) - (b) The bound charge densities arising from P_x and P_z respectively (denoted ρ_x^b and ρ_z^b) for $n_{2D} = 0.0$. They are nearly mirror images of each other ($\rho_x^b \sim -\rho_z^b$). (c) The total bound charge ($\rho_x^b + \rho_z^b$). The bound charges in the bulk cancel each other, except along the interface. This is the expected behaviour for Kittel domains. (d) The bound charge density arising from P_x for $n_{2D} = 0.15$. The arms of the domain walls are negatively charged. (e) The bound charge density arising from P_z for $n_{2D} = 0.15$. The arms of the domain walls are positively charged. (f) The total bound charge density for $n_{2D} = 0.15$. The contributions from P_x and P_z compensate for each other in the arms of the domain wall leaving a much smaller residual charge.

consistent with a head-to-head domain wall [see Fig 1.2, (b)] albeit where the polarization meets the domain wall at some angle other than 180° or 90°. Away from the domain wall, we see no significant free electrons until $n_{2D} \geq 0.3$ when they begin to spill-over to the interface.

The residual charge on the domain wall is important. It allows the wall to be manipulated by an external field. When a bias voltage, ΔV, is applied across the capacitor plates, the free and bound charges feel a force from the internal and external fields. In Ref [1], a bias voltage was applied to the isotropic model for $n_{2D} = 0.2$, and the shape of the zig-zag

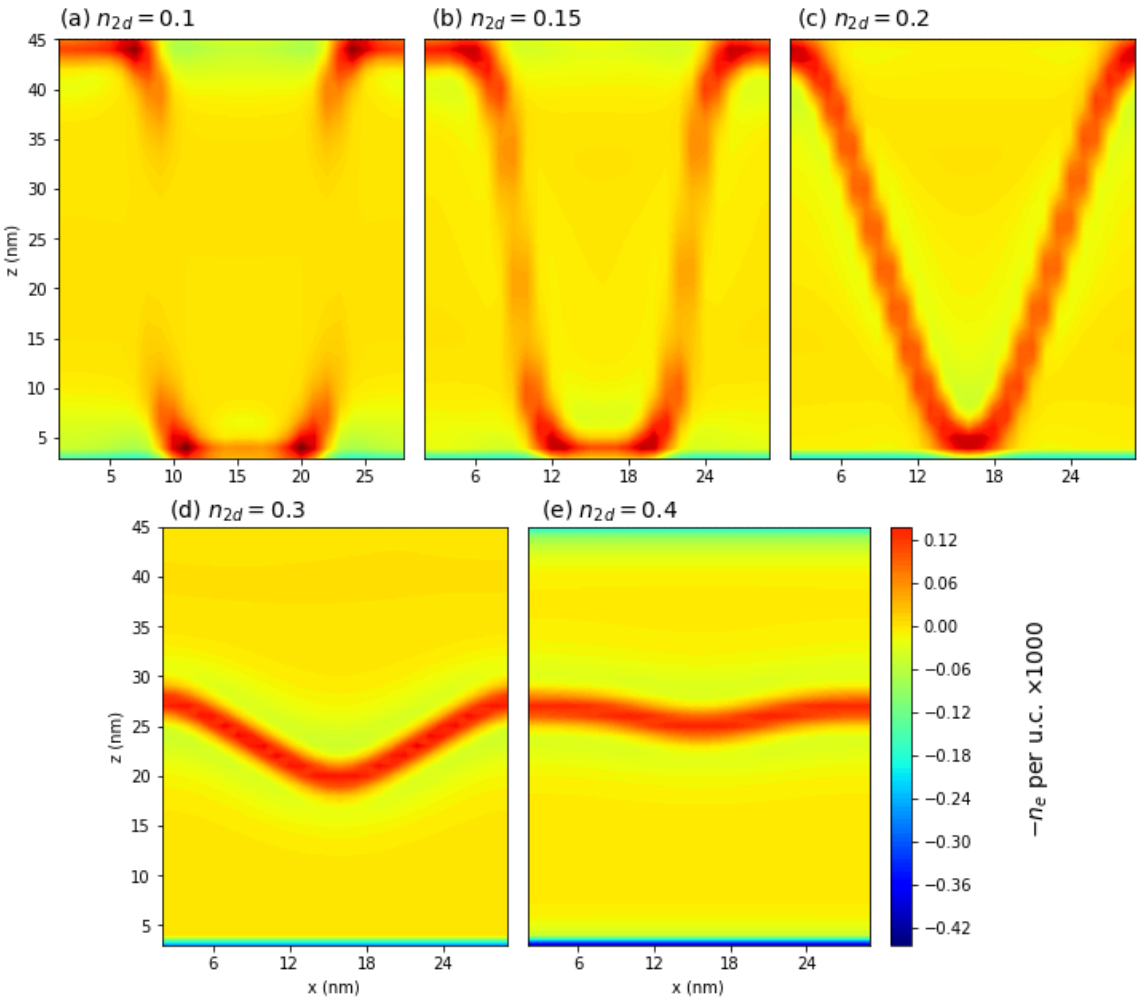

Figure 4.6: The total charge densities (n_e per unit cell). Since e is negatively charged, we multiply the scale by -1 so that the positive regions correspond to a positive charge density and vice-versa. We remove the rows near the interfaces because they overwhelm the values near the domain walls when $n_{2D} \geq 0.3$. There is $\sim 99\%$ charge cancellation between the free and bound charge densities across the domain walls.

domain wall was manipulated when $|\Delta V| \leq 2$. For larger values of ΔV, the polarization became a single domain, confining the electrons along the interface. The effects of a bias voltage remain to be tested for the anistropic model.

4.4 Domain Wall Neutrality

The (near) neutrality of the domain wall is expected since strongly charged domain walls are inherently unstable. Neutral domain walls do not generate electric fields, and consequently,

reduce the electrostatic energy in the free energy equation [see Eq (1.2) and Eq 2.10)]. We consider a model for a charge-neutral ferroelectric, and compare it against our results.

Let's consider a system with complete charge compensation, $Q_{\text{total}} = 0$. We must have that

$$\begin{aligned} Q_{\text{total}} &= \int_{\text{Ferroelectric}} d^3\mathbf{r}\ \ \rho^{\text{free}}(\mathbf{r}) + \int_{\text{Ferroelectric}} d^3\mathbf{r}\ \ \rho^{\text{bound}}(\mathbf{r}) \\ &= Q_{\text{free}} - \int_{\text{Ferroelectric}} d^3\mathbf{r}\ \ (\nabla \cdot \mathbf{P}(\mathbf{r})) \\ &= -e\frac{n_{2D}}{a^2}A - \oint_{\text{Surface}} dA\ \ (\hat{n} \cdot \mathbf{P}(\mathbf{r}))\,, \end{aligned} \tag{4.4}$$

where a is the lattice constant, A is the area of the ferroelectric surface, $\hat{n}$ is the unit vector normal to the surface bounding the ferroelectric, and we used the divergence theorem. If $Q_{\text{total}} = 0$,

$$-e\frac{n_{2D}}{a^2} = \frac{1}{A}\oint_{\text{Surface}} dA\ \ (\hat{n} \cdot \mathbf{P}(\mathbf{r}))\,. \tag{4.5}$$

The bounding surface is the x-y planes with area $A = L_x L_y$ at the top and bottom of the ferroelectric. The unit normal to the surface, $\hat{n}$, is just $\pm\hat{z}$, so we only need to consider P_z. Assume that P^{surf} is the average magnitude of the z-component of the polarization along the top and bottom of the ferroelectric. It is oriented inwards from the surface. Then,

$$\begin{aligned} -e\frac{n_{2D}}{a^2} &= \frac{1}{A}\left[\int_{\text{Top}} dA\ \ (+\hat{z}) \cdot \left(P^{\text{surf}}(-\hat{z})\right) + \int_{\text{Bottom}} dA\ \ (-\hat{z}) \cdot \left(P^{\text{surf}}\hat{z}\right)\right] \\ &= -2P^{\text{surf}}. \end{aligned}$$

$$\Rightarrow 2P^{\text{surf}} = e\frac{n_{2D}}{a^2} \tag{4.6}$$

From Table 2.1, the lattice constant, $a \approx 4 \times 10^{-10}$ m, so $\frac{e}{a^2} \approx 1.6 \times 10^{-19}$ C/(16×10^{-20})m$^2 \approx 1$ C/m^2. For a fully-compensated charged domain wall, we expect

$$P^{\text{surf}} = \frac{1}{2}n_{2D} \times \frac{C}{m^2}, \tag{4.7}$$

where n_{2D} is in units of electrons per unit cell.

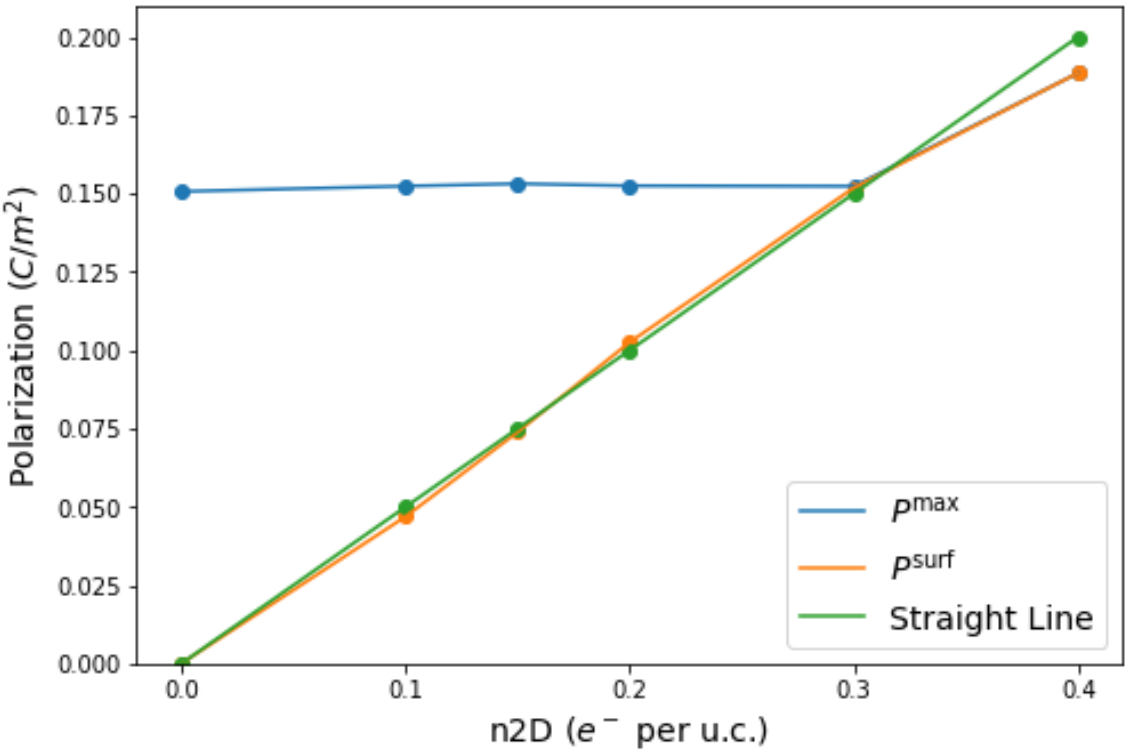

Figure 4.7: The maximum polarization ($P^{\max}$), the average surface polarization (P^{surf}), and the straight line $P = \frac{1}{2}n_{2D}$ are plotted versus n_{2D}. The maximum polarization within the FEM is the expected bulk polarization $P^{\text{bulk}} = 0.15$ C/m^2 through $n_{2D} = 0.3$. The average surface polarization grows linearly as a function of n_{2D}, and coincides with the straight line until n_{2D}=0.3. Above n_{2D}=0.3, the values for maximum polarization and average surface polarization are nearly identical, but deviate from the straight line.

We calculate P^{surf} from our results by averaging P_z along the surface

$$P^{\text{surf}} = \frac{1}{2N_x}\sum_{1}^{N_x}\left[P_{(n,1),z} - P_{(n,N_z),z}\right] \tag{4.8}$$

where N_x and N_z are the number of secondary lattice points along the x- and z-axes in the ferroelectric.

In Fig 4.7, we plot our value for P^{surf} against the line predicted in Eq (4.7). For $n_{2D} \leq 0.3$, we see a very close match. We do observe $\sim 2\%$ difference in our P^{surf} and the predicted value. This error does not appear to be systematic, and we attribute it to uncertainty in our model inherent in the lattice approximation, and the computational

difficulties of achieving convergence.

This relationship shows that the ferroelectric is overall very close to charge neutral. In the previous section, we observed that the domain wall has a net positive charge. Since we do not observe any meaningful concentration of electrons in the bulk of the ferroelectric, the residual charge along the domain wall must be compensated by the narrow band of negative bound charge along the interfaces. This is interesting, since it suggests that the net surface charge, and the net charge along the domain wall are equal and opposite.

Unmentioned in our earlier discussion of polarization was the bulk polarization predicted from the simplified LGD equation in section 1.7 [see Eq (1.4)]. For our coefficients, the predicted bulk polarization is approximately $P_0 = \sqrt{\frac{-a_3}{b}} \sim 0.15$ C/m^2. This value is equal to the maximum polarization, $P^{\max}$, observed in the ferroelectric for $n_{2D} \leq 0.3$. In Fig 4.1, we observe that the maximum value for the polarization is found within the centre of the domain, away from the interface when $n_{2D} < 0.3$. As n_{2D} approaches 0.3, $P^{\max}$ migrates towards the interface, and $P^{\text{surf}} = P^{\max} = P_0$. For $n_{2D} \geq 0.3$, we see that $P^{\text{surf}} > P_0$, and that P^{surf} is lower than the predicted value from Eq (4.7). This suggests that we are no longer getting complete charge compensation across the ferroelectric. We also observe a spill-over of electrons along the interfaces [see Figs A.5 and A.6] while still possessing an uncompensated residual positive charge along the domain wall. Understanding the dynamics of the system near the transition point $P^{\text{surf}} = P_0$ looks interesting, but was not further explored.

4.5 Electric Fields

Given the residual charge remaining along the domain wall, we expect residual electrical fields to be present. In Fig 4.8, for $n_{2D} \leq 0.15$ [(a) – (c)], very small fields are present along the arms of the domain wall. This is expected since the bound charge density is very small. The bound polarization along the positive ends of the domain, and along the interfaces generate the largest electric fields. At $n_{2D} = 0.2$, the domain wall is clearly visible, and it is surrounded by a small electric field. However, it remains much smaller than the fields along the interfaces. It is only when $n_{2D} \geq 0.3$ that we see fields along the domain wall that

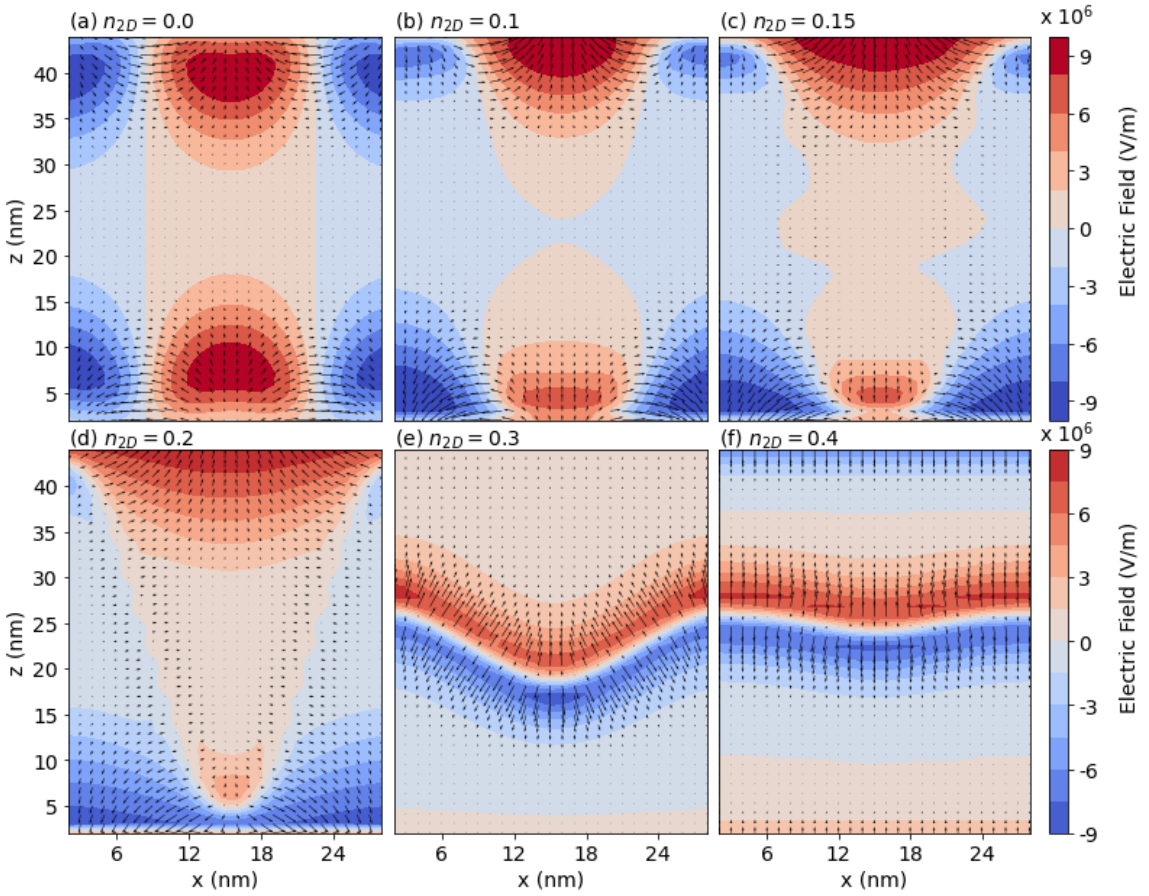

Figure 4.8: Electric fields. We have removed the regions near the boundaries because the bound charge swamps the scale [for (a) – (d) $z \in [2, 44]$ nm; (e) – (f) $z \in [3, 43]$ nm]. The color is based on the z-component of the electric field, E_z. (a) – (c) The electric field originates or terminates at areas of bound charge near the boundaries. There is negligible field within the bulk of the ferroelectric. (d) The arms of the domain wall generate a small, local electric field that permeates ~ 4 nm into the bulk. The largest fields are along the boundary between centers of bound charge. (e) – (f) The domain wall is generating an electric field that extends $\sim 8 - 10$ nm into the film. Elsewhere, the fields within the bulk are up to an order of magnitude smaller.

match the interfacial fields. These fields extend $\sim 8 - 10$ nm into the film perpendicular to the orientation of the domain wall before falling off. In all cases, regions of the ferroelectric more than ~ 10 nm away from the interfaces or the domain walls possess electric fields that are almost an order of magnitude smaller.

We can calculate the impact of the residual field on the polarization. For $|\mathbf{E}| \sim 10^7$ V/m, the background polarization arising from the residual field is $P^{\text{back}} = \epsilon_0 \chi |\mathbf{E}| \sim 4.4 \times 10^{-4}$ C/m^2. This is two orders of magnitude smaller than the bulk polarization, $P_0 \sim 0.15$ C/m^2.

We can also revisit our LGD equation to calculate the polarization directly. Consider a very simplified 1D version of Eq (2.14),

$$E_z \sim a_3 P_z, \tag{4.9}$$

whose solution is $P_z \sim 0.062$ C/m^2. This is $\sim 40\%$ of the bulk polarization, implying that the residual field can still be considered fairly weak.

4.6 Orbital Selectivity

In sections 4.3 and 4.4, we focused on the total free charge density. However, we know from our comparison of the isotropic and anisotropic models that the presence of multiple orbital types changes the rate at which the domain wall tilts. The absolute electron densities for the different orbitals are plotted in Appendix A. However, we find that it is more informative to look at their relative differences across the ferroelectric. In Fig 4.9, we plot the differences in electron density across the ferroelectric for the three orbital types.

Different orbital types have higher concentrations of electrons in different parts of the domain wall. The d_{xy} orbital always has the highest relative concentration wherever the domain wall is flat ($n_{2D} \leq 0.2$) or within the vertex ($n_{2D} \geq 0.2$) [sub-figures (a) – (i)]. Meanwhile, the arms of the domain wall have an excess of electrons in the d_{yz} orbital when $n_{2D} \leq 0.2$ [sub-figures (e), (f)]. However, when $n_{2D} \geq 0.3$, the d_{xy} orbital has the highest concentration of electrons within the arms, while the d_{xz} and d_{yz} orbitals have higher concentrations along its edges [sub-figures (g) – (i)]. Away from the domain walls, the concentrations of the different orbitals types are virtually identical.

We quantify these differences by summing the orbital charge densities over small areas where the differences manifest (i.e. positive ends of domains, vertices, and arms of the domain wall). When $n_{2D} \leq 0.15$, the d_{xy} orbitals have $\sim 20-30\%$ more charge than either other orbital type along the positive end of the domain. However, by $n_{2D} = 0.2$, this gap has narrowed to $\sim 5\%$ at the vertex, and only $\sim 1\%$ for $n_{2D} \geq 0.3$. In the arms of the domain wall, the d_{yz} orbital has $\sim 20-25\%$ more charge than either other orbital type at

$n_{2D} = 0.15$ before narrowing to $\sim 5\%$ at $n_{2D} = 0.2$. By $n_{2D} \geq 0.3$, the differences between all orbitals are very small and only amount to around $\sim 1\%$.

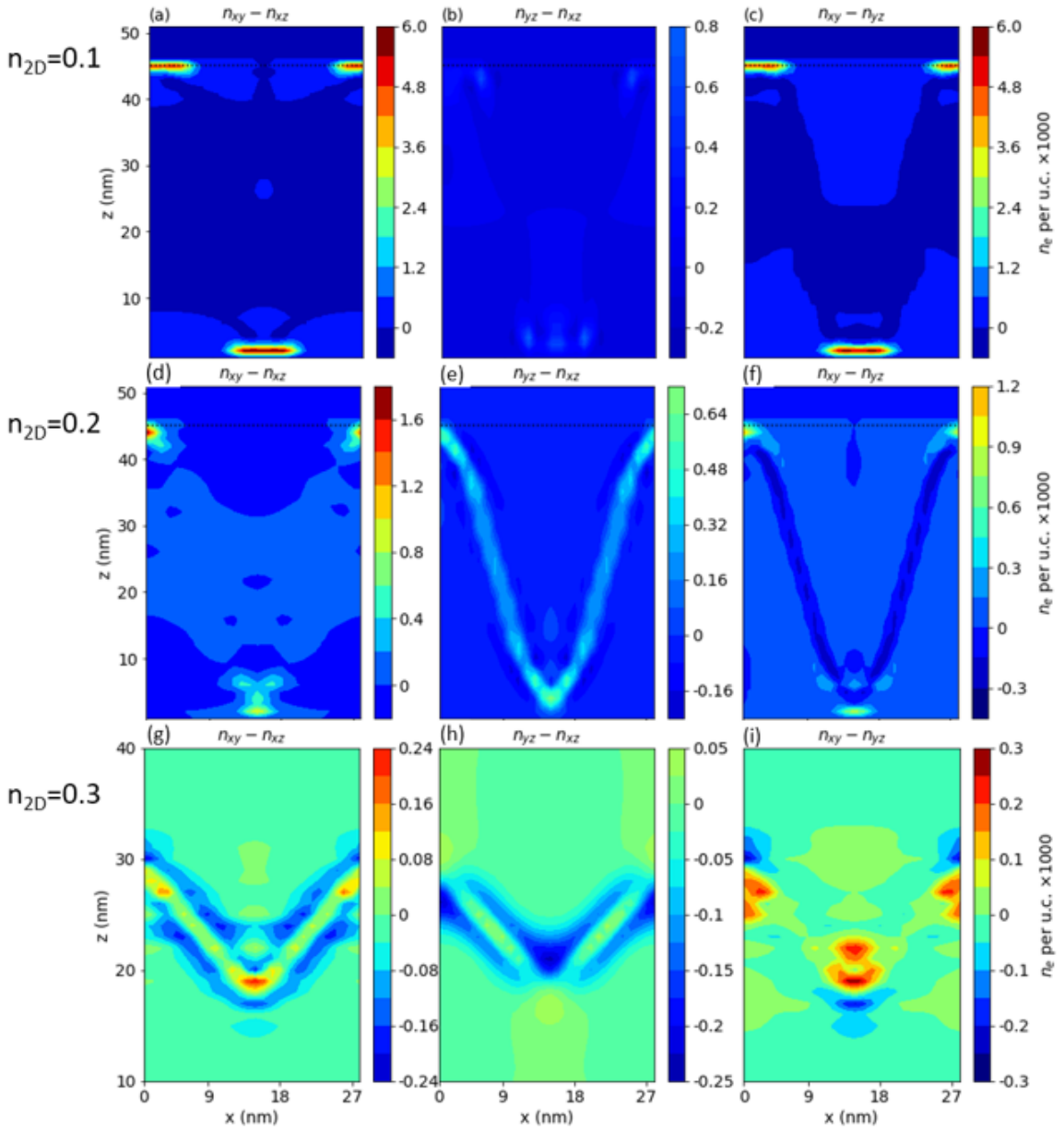

Figure 4.9: Orbital selectivity near the domain wall. $n_{2D} = 0.1$, (a), (c) The d_{xy} orbitals have more electrons than the d_{xz} and d_{yz} orbitals at the positive end of the domain. (b) The electrons in the d_{xz} and d_{yz} orbitals are approximately equal. $n_{2D} = 0.2$, (d) The d_{xy} orbitals have more electrons compared with d_{xz} orbitals in the vertices, with a smaller advantage along the arms of the domain walls. (e) The d_{yz} orbitals have a clearly defined, but only slightly higher concentration of electrons than do the d_{xz} orbitals within the domain wall. (f) The d_{yz} orbitals have a higher concentration of electrons than the d_{xy} orbitals except near the vertices. $n_{2D} = 0.3$. We restrict the z-axis to remove the interfaces. (f) – (g) We see that the d_{xy} and d_{yz} orbitals have more electrons than the d_{xz} orbitals in the centre of the domain wall, but that the d_{xz} orbitals have more electrons along the edges. (h) The d_{xy} orbitals have more electrons than the d_{yz} orbitals along the domain wall. The d_{yz} orbitals have more electrons than the d_{xy} orbitals on the outside of the vertex nearest the interface.

For $n_{2D} \geq 0.3$, we observe spill-over of charge from the domain wall to the interfaces. The interfacial electrons only occupy the d_{xy} orbital at $n_{2D} = 0.3$, but all three orbitals have noticeable free electron densities along the interface by $n_{2D} = 0.4$. Unlike the orbital selectivity observed in the domain wall, there are significant differences in density at the interface. In Fig 4.10, we plot the negative charge density for each orbital type across the ferroelectric for x = 15 nm. Summing the charge densities across the first five cells of the lattices, the ratio of $d_{xy} : d_{xz} : d_{yz}$ is $\sim 3 : 1 : 1$. We see that the peak d_{xy} concentration is closest to the interface before falling off rapidly, while the d_{xz} and d_{yz} orbital concentrations peak further out, and fall off more slowly. Simulations for paraelectric strontium titanate show an even larger orbital selectivity for the d_{xy} orbitals near the interface with a ratio of $\sim 8 : 1 : 1$ [61]. Meanwhile, the concentrations of electrons away from the interfaces are very similar throughout the ferroelectric. This corresponds with our previous result that the electron densities along the domain wall only differ by $\sim 1\%$ for large values of n_{2D}.

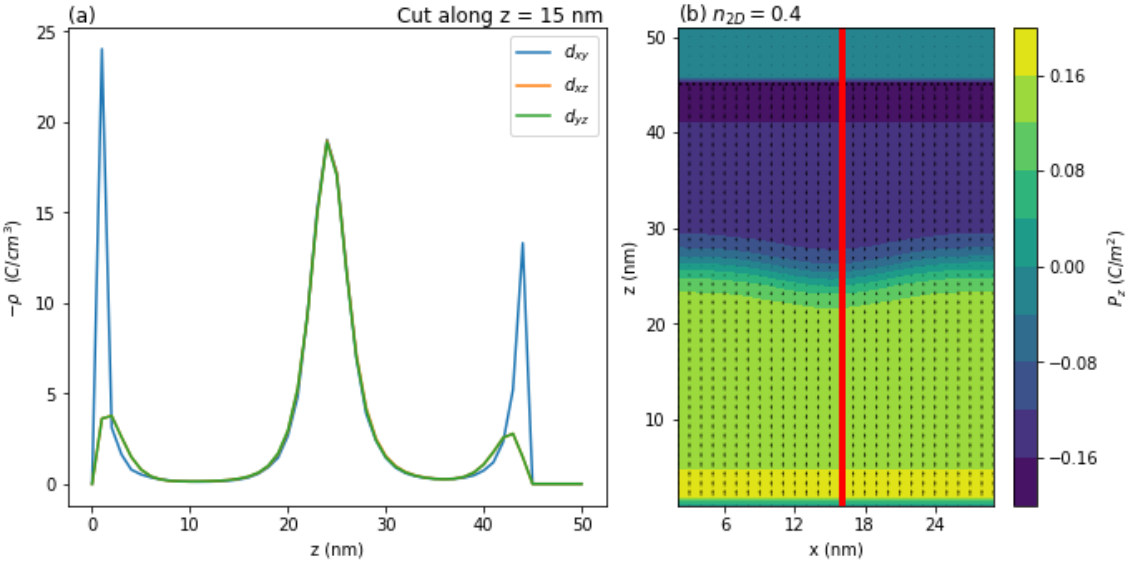

Figure 4.10: Charge density cut for $n_{2D} = 0.4$ and x=15 nm. (a) Plot of the negative charge densities for the orbital types along x = 15 nm. The d_{xy} orbital has the highest concentration of electrons along the interface before falling off. The d_{xz} and d_{yz} orbital concentrations peak further away from the interface, and fall off more slowly. The d_{xz} and d_{yz} orbital concentrations are identical to within the width of the line. We also see that that all three orbital types are identical to within the width of the line across the domain wall. (b) Visual representation of the cut across the ferroelectric. The color is determined by the P_z value.

The similarity in the electron densities across the domain wall is explained by the large number of occupied sub-bands in our system. In a bulk STO crystal, there are three conduction bands corresponding with the d_{xy}, d_{xz} and d_{yz} orbitals. The domain wall breaks the translational symmetry along the x- and z-axes. This only leaves the wavenumbers along the y-axis, k_y, as good quantum numbers. For each band, we have a collection of $N_x \times N_z$ sub-bands as a function of k_y where N_x, N_z are the number of lattices points along the x- and z-axis respectively within the ferroelectric.

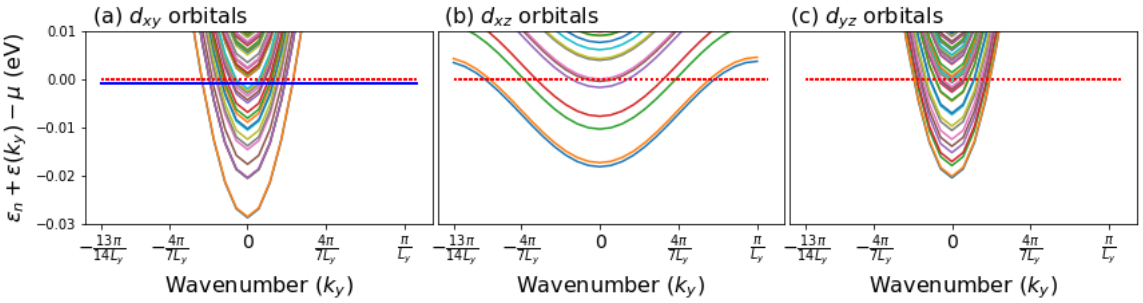

Figure 4.11: The sub-band structure for $n_{2D} = 0.1$. The red-dashed line is the zero value of energy. The energy scale has been normalized so that the zero corresponds with the chemical potential, μ. The blue line [sub-plot (a)] is the thermal energy relative to zero.

In Fig 4.11, we show the sub-band structure for $n_{2D} = 0.1$. The parabolic shape of the sub-bands shows that the effective mass along the y-axis is light for electrons in the d_{xy} and d_{yz} orbitals, and heavy for the d_{xz} orbital. When the effective mass is light, the wavefunction is more likely to spread out. Although we can not construct similar sub-bands along the x- and z-axes, the behaviour will be the same. Electrons will be light in the orbital plane, but heavy along the perpendicular axis (i.e. electrons in the d_{xy} orbital will spread out more in the xy-plane, but be more concentrated along the z-axis). In Fig 4.9 (g) – (i), we observe more electron in the d_{yz} and d_{xz} orbitals above and below the d_{xy} orbitals since they are light along the z-axis. In Fig 4.10 (a), the electrons in the d_{xy} orbital are more tightly held along the interface since they are heavy along the z-axis.

Even though $n_{2D} = 0.1$ is the lowest non-zero electron density we examined, we see numerous sub-bands lie below the chemical potential. For higher values of n_{2D}, the number of sub-bands increases further. At 10 K, the thermal energy is only ~ 0.4 meV. The difference in energy between the bottom of the bands and the chemical potential is approximately 20

– 30 meV depending on the orbital type. This is true for all values of n_{2D} in our range. This difference is almost two orders of magnitude larger than the thermal energy [see 4.11, (a) the blue line is the thermal energy relative to the chemical potential]. The chemical potential is therefore effectively the Fermi energy, and separates our occupied and unoccupied states.

We see the largest orbital selectivity when n_{2D} is smaller, and we have the lowest number of occupied sub-bands. For $n_{2D} \leq 0.2$, at least one orbital type had a noticeably larger concentration of charge in some area of the domain wall. (e.g., d_{xy} at the positive ends of the domain or the vertices, d_{yz} in the arms of the domain wall). As the electron density increased, these differences disappeared. There are too many occupied sub-bands for each orbital type, and the electrons are all equally attracted to the bound charge along the domain wall, such that the electron densities approach uniformity.

4.7 Kinetic Energy

We have still not explained how orbital selectivity and the domain wall are related. Since the potential acts on each orbital type equally, it cannot explain why the rate of tilt changes based on the type of orbitals present. We will therefore consider the contribution of kinetic energy to the orbital selectivity at the domain wall.

We construct a series of toy models for different orientations of the domain wall. The domain wall is represented by a periodic 1D chain of lattice points, where the hopping matrix elements between lattice points in the tight-binding Hamiltonian depend on the orbital type and the orientation of the edge between adjacent points (e.g., horizontal (x-axis), or vertical (z-axis)). We consider three different models:

1. A box model [see Fig 4.12, (a)] representing $n_{2D} = 0.1$, where the tops of the domains are flat, and the domain walls are vertical.

2. A steep pyramid model (Fig 4.12, (b)] representing $n_{2D} = 0.15$, where the domain wall is still flat at the top and bottom, but the arms of the domain wall have some tilt.

3. A shallow pyramid model [Fig 4.12, (c)] representing $n_{2D} = 0.3$, where the domain wall is mostly horizontal with small rises.

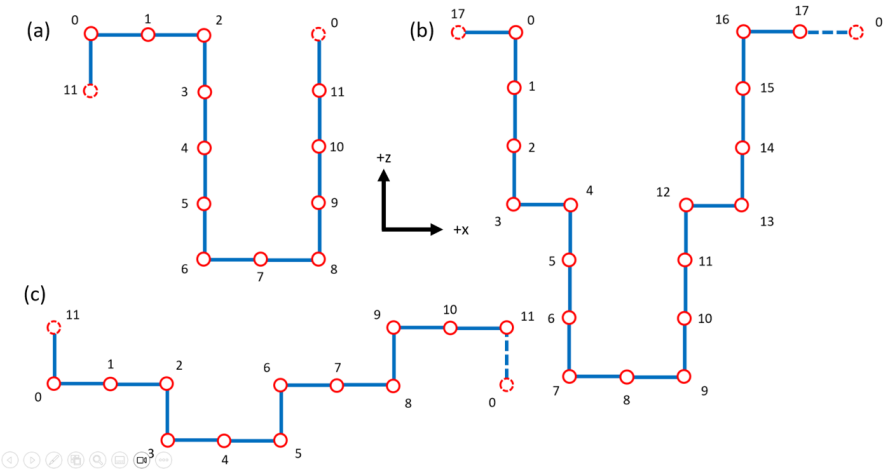

Figure 4.12: Toy Models for kinetic energy. The domain wall is represented by a 1D chain of lattice points, where the hopping matrix elements between lattice points in the tight-binding Hamiltonian depends on the orbital type and orientation of the transition. (a) The box model representing $n_{2D} = 0.1$. (b) The steep pyramid model representing $n_{2D} = 0.15$. (c) The shallow pyramid model representing $n_{2D} = 0.3$.

For clarity, we show the tight-binding Hamiltonian for orbital type α [see Eq 2.29] for

the 1D box model with potential, $\phi = 0$,

$$\mathbf{H}^{\alpha} = \begin{bmatrix} t_0 & t_x^\alpha & 0 & 0 & 0 & 0 & 0 & 0 & 0 & 0 & 0 & t_z^\alpha \\ t_x^\alpha & t_0 & t_x^\alpha & 0 & 0 & 0 & 0 & 0 & 0 & 0 & 0 & 0 \\ 0 & t_x^\alpha & t_0 & t_z^\alpha & 0 & 0 & 0 & 0 & 0 & 0 & 0 & 0 \\ 0 & 0 & t_z^\alpha & t_0 & t_z^\alpha & 0 & 0 & 0 & 0 & 0 & 0 & 0 \\ 0 & 0 & 0 & t_z^\alpha & t_0 & t_z^\alpha & 0 & 0 & 0 & 0 & 0 & 0 \\ 0 & 0 & 0 & 0 & t_z^\alpha & t_0 & t_z^\alpha & 0 & 0 & 0 & 0 & 0 \\ 0 & 0 & 0 & 0 & 0 & t_z^\alpha & t_0 & t_x^\alpha & 0 & 0 & 0 & 0 \\ 0 & 0 & 0 & 0 & 0 & 0 & t_x^\alpha & t_0 & t_x^\alpha & 0 & 0 & 0 \\ 0 & 0 & 0 & 0 & 0 & 0 & 0 & t_x^\alpha & t_0 & t_z^\alpha & 0 & 0 \\ 0 & 0 & 0 & 0 & 0 & 0 & 0 & 0 & t_z^\alpha & t_0 & t_z^\alpha & 0 \\ 0 & 0 & 0 & 0 & 0 & 0 & 0 & 0 & 0 & t_z^\alpha & t_0 & t_z^\alpha \\ t_z^\alpha & 0 & 0 & 0 & 0 & 0 & 0 & 0 & 0 & 0 & t_z^\alpha & t_0 \end{bmatrix}, \tag{4.10}$$

where t_0 is the on-site matrix element, t_x^α and and t_z^α are the hopping matrix element along the x-axis and z-axis respectively. We have suppressed the potential in order to isolate the kinetic energy. We solve the Hamiltonian for each orbital type where the different hopping matrix elements correspond with values for the tight binding models [see Eqs 2.30 - 2.39].

For a given n_{2D}, we calculate the chemical potential, and charge densities for the different orbitals using the same techniques discussed in Chapters 2 and 3. We use the same values for the lattice constant, and lattice spacing making our toy models significantly smaller than our anisotropic model (i.e. (x $\times$ z dimensions) box model = 4×6 nm^2, steep pyramid = 6×6 nm^2, shallow pyramid = 8×2 nm^2). These small sizes mean that there are very few electrons in our models. For the box and steep pyramid models, the d_{xz} orbital is unoccupied because the few electrons present in the system fill the lower energy d_{xy} and d_{yz} orbital sub-bands. Fortunately, this proves not to be affect our observations. We crudely plot the charge densities for each orbital type in Fig 4.13. We see that electrons prefer to lie at lattice points where the nearest neighbours lie in the same plane as the orbital type (i.e. when lattice points are aligned horizontally, electrons in the d_{xy} orbital are more likely to

be present). The kinetic energy is minimized when the orbital plane and the domain wall are parallel.

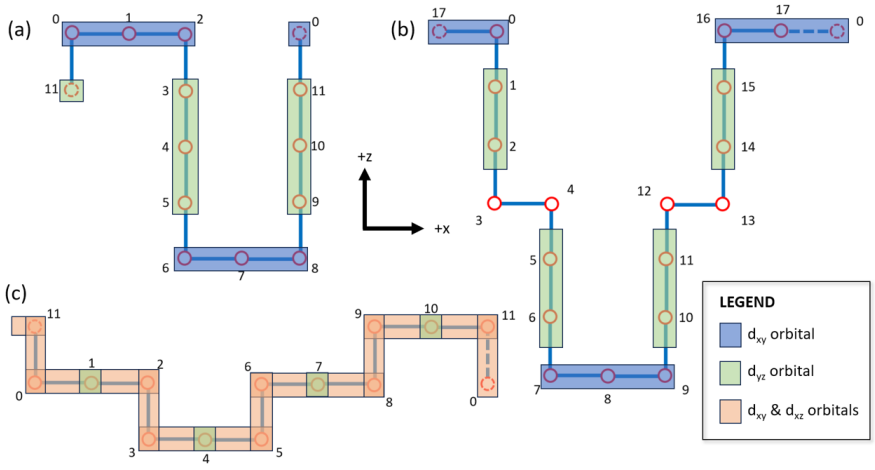

Figure 4.13: Orbital preferences for the different toy models. The coloured boxes collect the lattice points with the highest probability of occupancy for a given type of orbital. The orbitals with their plane parallel to the domain wall have a higher probability of occupancy. The d_{xz} orbital is missing from (a) and (b) because its lowest energy state was above the chemical potential. For (c), like d_{xy}, it was uniformly spread across the domain wall.

Revisiting Fig 4.1 for the polarizations, for $n_{2D} < 0.2$, the top of the domain is horizontal, and the arms of the domain wall are near vertical [(b) – (c)]. Since the kinetic energy is minimized when the orbital plane and the domain wall are parallel, we should find more electrons in the d_{xy} orbitals along the positive end of the domain and in the d_{yz} orbitals in the arms of the domain wall. For $n_{2D} = 0.1$, we did see that the d_{xy} orbital had the highest overall charge density along the positive end of the domain, but we did not see meaningful differences along the arms of the domain wall [see Fig 4.9 (a) – (c)]. However, the bound charge along the arms of the domain walls is tiny, so any differences are too small to observe. If we take a horizontal cut across the domain wall for the charge density at $n_{2D} = 0.15$ (not shown), we do observe that d_{yz} has the highest charge density within the arm compared with the other orbitals by around 20%. By $n_{2D} = 0.2$, the top of the domain has shrunk to a vertex, and the arms have tilted away from the vertical ($\theta \sim 20^{\circ}$). Although the arm is no longer vertical, the d_{yz} orbital plane is the closest in terms of orientation. We see that the electrons in the d_{xy} orbitals remain the most concentrated in the vertices, while the

electrons in the d_{yz} orbitals do have the highest concentration in the arms [see Fig 4.9, (d) – (f)]. For $n_{2D} \geq 0.3$, the domain wall is flattening, and the tilt angle is $\sim 65^{o} - 80^{o}$. The d_{xy} orbital plane is the most parallel with the domain wall, and we see that the electrons in the d_{xy} orbital do have the highest concentration at the vertices, and along the centre of the domain wall [see Figs 4.9 (g) – (i)]. We expect the concentrations of the d_{xz} and d_{yz} orbitals to be the same when the domain wall is flat due to rotational symmetry around the z-axis. This equality is almost observed when $n_{2D} = 0.4$ [see Fig 4.14].

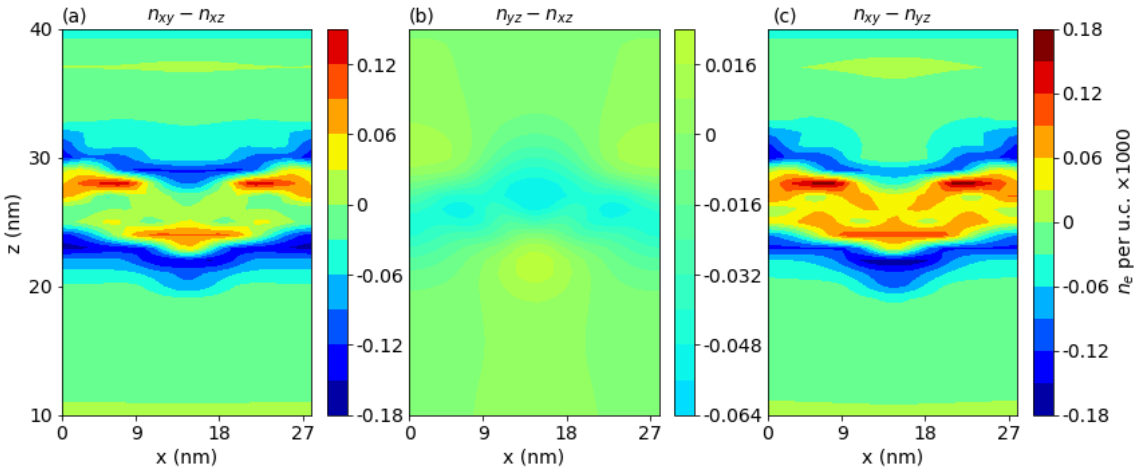

Figure 4.14: The difference between the electron densities for $n_{2D} = 0.4$. (a), (c) The d_{xy} orbitals have more electrons than the d_{xz} and d_{yz} orbitals in the vertices of the domain wall, with a smaller advantage along the arms of the domain walls. (b) The d_{xz} and d_{yz} orbitals are very close to being equal. This equality is expected for symmetry reasons.

Based on these observations, we argue that the rate of tilt of the domain wall is related to the kinetic energy of the different orbital types along the domain wall. When $n_{2D} \sim 0.1$, the top of the domain is wide and the domains walls are close to vertical. The system wants to tilt the domain wall to generate bound charge in order to reduce the electrostatic energy, but it can also lower its energy by keeping parts of the domain wall aligned with the d_{xy} and d_{yz} orbitals in order to minimize their kinetic energy. This tension slows the rate of tilting when $n_{2D} \leq 0.2$. As the charge density increases, the wall must tilt in order to generate additional charge. As it tilts, the positive end of the domain shrinks to a vertex, and a higher percentage of the overall bound charge is found in the arms of the domain wall. More of the free charge must move into the arms to compensate. As it tilts through

45°, the electrons in the d_{xy} orbitals will have lower kinetic energy than those in d_{yz}. Now, the tilt is accelerated because the system can lower its kinetic energy for the electrons in the d_{xy} orbitals by flattening further.

While this argument is suggestive, we were unable to develop a quantitative relationship between n_{2D}, the tilt angle of the domain wall, and the relative ratios of electrons in the different orbitals. Although we see a clear preference for different orbitals being filled for different values of n_{2D}, the differences between orbital selectivity is a matter of a few percent, and not orders of magnitude. Since there is already an inherent tilt associated with increasing n_{2D}, it is difficult to disentangle how the total charge, and the distribution of charge across the orbitals interact to determine the final angle. A more rigorous energy calculation is probably required, but was beyond the scope of this thesis.

4.8 Summary

We are now in a position to answer our two questions more definitively.

1. *How does the electron density, n_{2D}, affect the domain wall?* We observed that increasing n_{2D} corresponds with an increasing tilt in the domain wall. This was the same behaviour observed in the isotropic model. However, the rate of tilt was very different between the two. We argue that this is related to the kinetic energy of the different orbitals types. We also observed that our ferroelectric satisfied near net charge neutrality. This led to the average P_z component of the surface polarization being linearly related to n_{2D}. In this scenario, the residual positive charge along the domain wall is a requirement to neutralize the negative bound charge along the interfaces generated by our boundary conditions.

2. *How do the t_{2g} orbitals and the domain wall interact?* The t_{2g} orbitals undergo orbital selectivity along the domain wall related to the relative orientations of their orbital planes, and the domain wall. When the two planes are aligned, the kinetic energy is minimized, and they have higher charge concentrations in that region. By trying to minimize the kinetic energy, the rate of tilt for the domain wall is slower when $n_{2D} \leq 0.2$, and faster when $n_{2D} \geq 0.3$.

Chapter 5

Conclusion

Electron-doped ferroelectrics are receiving renewed interest at the moment because of their potential utility in nano-electronic devices. They can contain charged domain walls at the interface between two domains [6–8]. Free electrons can become concentrated along the domain wall, which acts like a conductive wire or plane [4,5,9]. The location of the domain wall can be manipulated using an external electric field providing a novel mechanism for re-writable circuitry. We explored how the charged domain wall was influenced by free electrons occupying the t_{2g} orbitals in an electron-doped perovoskite ferroelectric, modeled on STO and the LAO-STO interface.

We built an analytical model based on Landau-Ginzburg-Devonshire (LGD) theory, and a tight-binding Hamiltonians for free electrons occupying the t_{2g} orbitals (d_{xy}, d_{xz}, d_{yz}). We self-consistently solved for polarization, potential, and electron density in an iterative manner using a finite-difference approximation. We minimized the LGD free energy equation to find the polarization. We solved a trio of Hamiltonians, and used a two-dimensional electron density, n_{2D}, to determine the chemical potential and free electron densities for each orbital type. Finally, we solved Gauss' equation for the electric potential using our free and bound charges, and calculated the electric field. Our results cover a range of n_{2D} corresponding with different quantities of charge transfer across the LAO-STO interface.

We set out to investigate two broad questions:

1. How does the electron density, n_{2D}, affect the domain wall?

2. How do the t_{2g} orbitals and the domain wall interact?

In terms of the electron density and n_{2D}, we observed the same qualitative behaviour as the isotropic model. As n_{2D} increased, the domain wall tilted away from the vertical in order to generate bound charge with which to compensate the free charge. However, there were noticeable differences in the rate of tilt between the two models. For $n_{2D} \leq 0.2$, the rate of tilt was slower in the anisotropic model, while for values of $n_{2D} \geq 0.3$, the rate of tilt was faster.

Since each orbital feels the potential equally, we argue that the difference can be attributed to the kinetic energy of the electrons across the different orbital types. From our toy models, when the orbital plane (e.g., x-y plane for the d_{xy} orbital) is parallel with the plane of the domain wall, the electrons have a lower kinetic energy, and higher probability of occupancy. To minimize its energy, the domain wall tries to stay aligned with the orbital planes. For $n_{2D} \leq 0.2$, the top of the domain is flat and aligned with the d_{xy} orbitals, while the the arms of the domain wall are close to vertical, and aligned with the d_{yz} orbitals. The domain wall tries to preserve this orientation by slowing the rate of tilt. However, as the electron density increases, the positive end of the domain eventually shrinks, and the arms of the wall tilt to generate additional bound charge. This pushes more electrons into the arms of the domain wall. Eventually, the wall tilts through 45^{o}, and the kinetic energy for the d_{xy} orbital is lower than the d_{yz} orbital. To minimize the kinetic energy, the domain wall now accelerates its tilt to lie along the x-y plane.

Orbital selectivity is also tied to kinetic energy. Orbital types have their highest concentration of electrons when the orbital plane is aligned with the plane of the domain wall. Selectivity was most pronounced at low values of n_{2D} (≤ 0.2) with differences in electron density between orbital types of $\sim 20 - 30\%$. As the electron density increased, the large number of occupied sub-bands for each orbital type eventually gave rise to nearly uniform electron densities across the domain walls. There are still differences, but they are an increasingly small percentage of the overall electron densities ($\sim 1\%$).

Our ferroelectric was found to be close to charge neutral. This was related to the average P_z component of the surface polarization being linearly proportional to n_{2D} to ensure charge

compensation. Our domain walls were slightly positively charged across our range of n_{2D}. The small, residual positive charge along the domain wall was offset by a narrow, negative bound charge along the interface. The positive bound charge produced a weak depolarizing field that only penetrated ~ 10 nm into the bulk.

We found that our maximum polarization also equaled the bulk polarization, P_0, predicted from a simplified free energy equation [see Eq (1.4]. The bulk polarization was found within the centre of the domains before migrating to the surface when $n_{2D} \sim 0.3$. This is also the value at which the relationship between the average P_z component of surface polarization and n_{2D} broke down, and we first observed electrons began to spill-over to the interface. However, this was not further explored.

As a parting comment, we identified several areas for further investigation. Some were part of the original research roadmap, but others emerged naturally due to unexpected observations. Some open questions are:

1. How is the rotation of the polarization related to a_1? Can it be fully supressed? Does it impact the speed at which the domain wall tilts?

2. What is happening at the cross-over between the bulk polarization and the average P_z component of the surface polarization in Fig 4.7? Can we find a new relationship between them when $P_z^{\text{surf}} > P^{\text{bulk}}$?

3. Is there anything interesting happening when the domain wall disconnects from the interface? There should be a sudden change in the bound charge near the vertices since they are no longer constrained by the values along the interface. Results in the gap between $n_{2D} = 0.2$ and 0.3 were difficult to converge.

4. How does the domain wall react if we apply a voltage bias across the capacitors? Do we observe the same behaviour as the isotropic model?

5. What happens if we add coupling between polarization and charge density in the free energy equation?

Bibliography

[1] W. A. Atkinson. Evolution of domain structure with electron doping in ferroelectric thin films. *Physical Review B*, 106:134102, Oct 2022.

[2] W.X. Zhou and A. Ariando. Review on ferroelectric/polar metals. *Japanese Journal of Applied Physics*, 59(SI):SI0802, 2020.

[3] O. Auciello, J.F. Scott, R. Ramesh, et al. The physics of ferroelectric memories. *Physics Today*, 51(7):22–27, 1998.

[4] P.S. Bednyakov, T. Sluka, A.K. Tagantsev, D. Damjanovic, and N. Setter. Formation of charged ferroelectric domain walls with controlled periodicity. *Scientific Reports*, 5(1):15819, 2015.

[5] P.S. Bednyakov, B.I. Sturman, T. Sluka, A.K. Tagantsev, and P.V. Yudin. Physics and applications of charged domain walls. *npj Computational Materials*, 4(1):65, 2018.

[6] M.Y. Gureev, P. Mokrỳ, A.K. Tagantsev, and N. Setter. Ferroelectric charged domain walls in an applied electric field. *Physical Review B*, 86(10):104104, 2012.

[7] M.Y. Gureev, A.K. Tagantsev, and N. Setter. Head-to-head and tail-to-tail 180^o domain walls in an isolated ferroelectric. *Physical Review B*, 83(18):184104, 2011.

[8] T. Sluka, A.K. Tagantsev, P. Bednyakov, and N. Setter. Free-electron gas at charged domain walls in insulating $BaTiO_3$. *Nature Communications*, 4(1):1808, 2013.

[9] B. Sturman, E. Podivilov, M. Stepanov, A.K. Tagantsev, and N. Setter. Quantum properties of charged ferroelectric domain walls. *Physical Review B*, 92(21):214112, 2015.

[10] T. Xu, T. Shimada, Y. Araki, J. Wang, and T. Kitamura. Multiferroic domain walls in ferroelectric $PbTiO_3$ with oxygen deficiency. *Nano Letters*, 16(1):454–458, 2016.

[11] J. Wang, X-L. Xu, X. Li, J. Wang, X-L. Xu, and X. Li. Recent progress of multiferroicity and magnetoelectric effects in ABX_3-type perovskite metal–organic frameworks. *Advanced Materials Interfaces.*, 2023-07-20.

[12] J. Zhu, H. Zhao, and W. Hu. Coexistence of ferroelectricity and ferromagnetism in hex-GeS nanowires. *Physical Chemistry Chemical Physics*, 2023.

[13] C.W. Rischau, X. Lin, C.P. Grams, D. Finck, S. Harms, J. Engelmayer, T. Lorenz, Y. Gallais, B. Fauque, J. Hemberger, et al. A ferroelectric quantum phase transition inside the superconducting dome of $Sr_{1-x}Ca_xTiO_{3-\delta}$. *Nature Physics*, 13(7):643–648, 2017.

[14] J.M. Edge, Y. Kedem, U. Aschauer, N.A. Spaldin, and A.V. Balatsky. Quantum critical origin of the superconducting dome in $SrTiO_3$. *Physical Review Letters*, 115(24):247002, 2015.

[15] J.G. Bednorz and K.A. Müller. $Sr_{1-x}Ca_xTiO_3$: An XY quantum ferroelectric with transition to randomness. *Physical Review Letters*, 52(25):2289, 1984.

[16] M. Itoh, R. Wang, Y. Inaguma, T. Yamaguchi, Y.J. Shan, and T. Nakamura. Ferroelectricity induced by oxygen isotope exchange in strontium titanate perovskite. *Physical Review Letters*, 82(17):3540, 1999.

[17] V.V. Lemanov, E.P. Smirnova, P.P. Syrnikov, and E.A. Tarakanov. Phase transitions and glasslike behavior in $Sr_{1-x}Ba_xTiO_3$. *Physical Review B*, 54(5):3151, 1996.

[18] J.H. Haeni, P. Irvin, W. Chang, R. Uecker, P. Reiche, Y.L. Li, S. Choudhury, W. Tian, M.E. Hawley, B. Craigo, et al. Room-temperature ferroelectricity in strained $SrTiO_3$. *Nature*, 430(7001):758–761, 2004.

[19] H. Uwe and T. Sakudo. Stress-induced ferroelectricity and soft phonon modes in $SrTiO_3$. *Physical Review B*, 13(1):271, 1976.

[20] R.E. Cohen. Origin of ferroelectricity in perovskite oxides. *Nature*, 358(6382):136–138, 1992.

[21] W-Y. Pan, Y-C. Tang, Y. Yin, A-Z. Song, J-R. Yu, S. Ye, B-P. Zhang, and J-F. Li. Ferroelectric and photovoltaic properties of (Ba, Ca)(Ti, Sn, Zr)O_3 perovskite ceramics. *Ceramics International*, 47(16):23453–23462, Aug 15 2021.

[22] G.H. Kwei, A.C. Lawson, S.J.L. Billinge, and S.W. Cheong. Structures of the ferroelectric phases of barium titanate. *The Journal of Physical Chemistry*, 97(10):2368–2377, 1993.

[23] P. Marton, M.A.P. Gonçalves, M. Paściak, S. Körbel, V. Chumchal, M. Plešinger, A. Klíč, and J. Hlinka. Zigzag charged domain walls in ferroelectric $PbTiO_3$. *Physical Review B*, 107(9):094102, 2023.

[24] C-L. Jia, S-B. Mi, K. Urban, I. Vrejoiu, M. Alexe, and D. Hesse. Atomic-scale study of electric dipoles near charged and uncharged domain walls in ferroelectric films. *Nature Materials*, 7(1):57–61, 2008.

[25] P.W. Anderson and E.I. Blount. Symmetry considerations on martensitic transformations: "ferroelectric" metals? *Physical Review Letters*, 14(7):217, 1965.

[26] T.H. Kim, D. Puggioni, Y. Yuan, L. Xie, H. Zhou, N. Campbell, P.J. Ryan, Y. Choi, J-W. Kim, J.R. Patzner, et al. Polar metals by geometric design. *Nature*, 533(7601):68–72, 2016.

[27] H.J. Zhao, A. Filippetti, C. Escorihuela-Sayalero, P. Delugas, E. Canadell, L. Bellaiche, V. Fiorentini, and J. Íñiguez. Meta-screening and permanence of polar distortion in metallized ferroelectrics. *Physical Review B*, 97(5):054107, 2018.

[28] J. Fujioka, A. Doi, D. Okuyama, D. Morikawa, T. Arima, K.N. Okada, Y. Kaneko, T. Fukuda, H. Uchiyama, D. Ishikawa, et al. Ferroelectric-like metallic state in electron doped $BaTiO_3$. *Scientific Reports*, 5(1):13207, 2015.

[29] T. Kolodiazhnyi, M. Tachibana, H. Kawaji, J. Hwang, and E. Takayama-Muromachi. Persistence of ferroelectricity in $BaTiO_3$ through the insulator-metal transition. *Physical Review Letters*, 104(14):147602, 2010.

[30] K.S. Takahashi, Y. Matsubara, M.S. Bahramy, N. Ogawa, D. Hashizume, Y. Tokura, and M. Kawasaki. Polar metal phase stabilized in strained La-doped $BaTiO_3$ films. *Scientific Reports*, 7(1):4631, 2017.

[31] C. Collignon, X. Lin, C.W. Rischau, B. Fauqué, and K. Behnia. Metallicity and superconductivity in doped strontium titanate. *Annual Review of Condensed Matter Physics*, 10:25–44, 2019.

[32] C.S. Werner, S.J. Herr, K. Buse, B. Sturman, E. Soergel, C. Razzaghi, and I. Breunig. Large and accessible conductivity of charged domain walls in lithium niobate. *Scientific Reports*, 7(1):9862–8, 2017.

[33] Y. Shi, Y. Guo, X. Wang, A.J. Princep, D. Khalyavin, P. Manuel, Y. Michiue, A. Sato, K. Tsuda, S. Yu, et al. A ferroelectric-like structural transition in a metal. *Nature Materials*, 12(11):1024–1027, 2013.

[34] T. Sluka, A.K. Tagantsev, P.S. Bednyakov, and N. Setter. Free-electron gas at charged domain walls in insulating $BaTiO_3$. *Nature Communications*, 4(1):1808–, 2013.

[35] G.M. Guro, I.I. Ivanchik, and N.F. Kovtonyu. c-domain barium titanate crystal in a short-circuited capacitor. *Soviet Physics Solid State, USSR*, 11(7):1574–+, 1970.

[36] R. Pentcheva and W.E. Pickett. Avoiding the polarization catastrophe in $LaAlO_3$ overlayers on $SrTiO_3$ (001) through polar distortion. *Physical Review Letters*, 102(10):107602, 2009.

[37] N. Nakagawa, H.Y. Hwang, and D.A. Muller. Why some interfaces cannot be sharp. *Nature Materials*, 5(3):204–209, 2006.

[38] N.C. Bristowe, P. Ghosez, P.B. Littlewood, and E. Artacho. The origin of two-dimensional electron gases at oxide interfaces: insights from theory. *Journal of Physics: Condensed Matter*, 26(14):143201, 2014.

[39] M. Salluzzo, J.C. Cezar, N.B. Brookes, V. Bisogni, G.M. De Luca, C. Richter, S. Thiel, J. Mannhart, M. Huijben, A. Brinkman, et al. Orbital reconstruction and the two-dimensional electron gas at the $LaAlO_3/SrTiO_3$ interface. *Physical Review Letters*, 102(16):166804, 2009.

[40] A. Ohtomo and H.Y. Hwang. A high-mobility electron gas at the $LaAlO_3/SrTiO_3$ heterointerface. *Nature*, 427(6973):423–426, 2004.

[41] S. Thiel, G. Hammerl, A. Schmehl, C.W. Schneider, and J. Mannhart. Tunable quasi-two-dimensional electron gases in oxide heterostructures. *Science*, 313(5795):1942–1945, 2006.

[42] S. Gariglio, A. Fête, and J-M. Triscone. Electron confinement at the $LaAlO_3/SrTiO_3$ interface. *Journal of Physics: Condensed Matter*, 27(28):283201, 2015.

[43] D.A. Dikin, M. Mehta, C.W. Bark, C.M. Folkman, C.B. Eom, and V. Chandrasekhar. Coexistence of superconductivity and ferromagnetism in two dimensions. *Physical Review Letters*, 107(5):056802, 2011.

[44] J.A. Bert, B. Kalisky, C. Bell, M. Kim, Y. Hikita, H.Y. Hwang, and K.A. Moler. Direct imaging of the coexistence of ferromagnetism and superconductivity at the $LaAlO_3/SrTiO_3$ interface. *Nature Physics*, 7(10):767–771, 2011.

[45] N. Reyren, S. Thiel, A.D. Caviglia, L.F. Kourkoutis, G. Hammerl, C. Richter, C.W. Schneider, T. Kopp, A-S. Ruetschi, D. Jaccard, et al. Superconducting interfaces between insulating oxides. *Science*, 317(5842):1196–1199, 2007.

[46] L. Li, C. Richter, J. Mannhart, and R.C. Ashoori. Coexistence of magnetic order and two-dimensional superconductivity at $LaAlO_3/SrTiO_3$ interfaces. *Nature Physics*, 7(10):762–766, 2011.

[47] A. Brinkman, M. Huijben, M. Van Zalk, J. Huijben, U. Zeitler, J.C. Maan, W.G. van der Wiel, G.J.H.M. Rijnders, D.H.A. Blank, and H. Hilgenkamp. Magnetic effects at the interface between non-magnetic oxides. *Nature Materials*, 6(7):493–496, 2007.

[48] N. Boudjada, G. Wachtel, and A. Paramekanti. Magnetic and nematic orders of the two-dimensional electron gas at oxide (111) surfaces and interfaces. *Physical Review Letters*, 120(8):086802, 2018.

[49] S. Davis, V. Chandrasekhar, Z. Huang, K. Han, T. Venkatesan, et al. Anisotropic multicarrier transport at the (111) $LaAlO_3/SrTiO_3$ interface. *Physical Review B*, 95(3):035127, 2017.

[50] P. Chandra and P.B. Littlewood. A landau primer for ferroelectrics. In *Physics of Ferroelectrics: A Modern Perspective*, pages 69–116. Springer, 2007.

[51] K.M. Rabe, C.H. Ahn, and J-M. Triscone. *Physics of ferroelectrics: A modern perspective*, volume 105. Springer Science & Business Media, 2007.

[52] K.S. Chapman and W.A. Atkinson. Mechanism for switchability in electron-doped ferroelectric interfaces. *Physical Review B*, 105(3):035307, 2022.

[53] R.K. Behera, C-W. Lee, D. Lee, A.N. Morozovska, S.B. Sinnott, A. Asthagiri, V. Gopalan, and S.R. Phillpot. Structure and energetics of 180^o domain walls in $PbTiO_3$ by density functional theory. *Journal of Physics: Condensed Matter*, 23(17):175902, 2011.

[54] B. Meyer and D. Vanderbilt. Ab initio study of ferroelectric domain walls in $PbTiO_3$. *Physical Review B*, 65(10):104111, 2002.

[55] Y. Gu, M. Li, A.N. Morozovska, Y. Wang, E.A. Eliseev, V. Gopalan, and L-Q. Chen. Flexoelectricity and ferroelectric domain wall structures: Phase-field modeling and dft calculations. *Physical Review B*, 89(17):174111, 2014.

[56] J. Seidel, L.W. Martin, Q. He, Q. Zhan, Y-H. Chu, A. Rother, M.E. Hawkridge, P. Maksymovych, P. Yu, M. Gajek, et al. Conduction at domain walls in oxide multiferroics. *Nature Materials*, 8(3):229–234, 2009.

[57] Z. Liu, H. Wang, M. Li, L. Tao, T.R. Paudel, H. Yu, Y. Wang, S. Hong, M. Zhang, Z. Ren, et al. In-plane charged domain walls with memristive behaviour in a ferroelectric film. *Nature*, 613(7945):656–661, 2023.

[58] G. Tuvia, Y. Frenkel, P.K. Rout, I. Silber, B. Kalisky, and Y. Dagan. Ferroelectric exchange bias affects interfacial electronic states. *Advanced Materials*, 32(29):2000216, 2020.

[59] J.M. Neuberger, D.R. Rice Jr, and J.W. Swift. Numberical solutions of a vector ginzburg-landau equation with a triple well potential. *International Journal of Bifurcation and Chaos*, 13(11):3295–3306, 2003.

[60] V. Eyert. A comparative study on methods for convergence acceleration of iterative vector sequences. *Journal of Computational Physics*, 124(2):271–285, 1996.

[61] A. Raslan, P. Lafleur, and W.A. Atkinson. Temperature-dependent band structure of $SrTiO_3$ interfaces. *Physical Review B*, 95(5):054106, 2017.

[62] V. Eyert. A comparative study on methods for convergence acceleration of iterative vector sequences. *Journal of Computational Physics*, 124(2):271–285, 1996.

Appendix A

Raw Data

The following figures show the polarization, electron densities (n_e), and bound charge density for individual n_{2D}. Each sub-figure has their own axes including colour bar. Analysis of these results is found in Chapter 4.

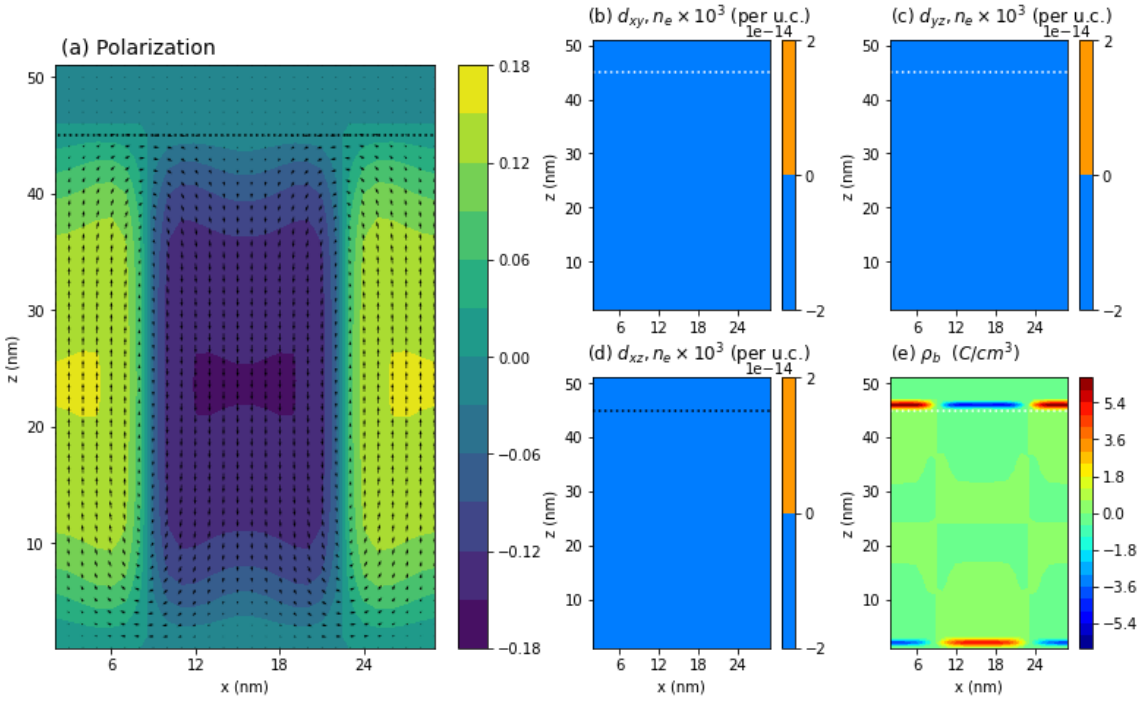

Figure A.1: Polarization, electron densities and bound polarization for n2D=0.0. These figures correspond with a cut through the model in the x-z plane. (a) The arrows correspond with the direction of the polarization vector. The color scale is based on the P_z component of polarization. There are two 180° domain walls separating two domains with the polarization aligned along the z-axis. (b) – (d) There is no free charge in the system. (e) A line of bound charge is found along the interface at the positive and negative ends of the domains.

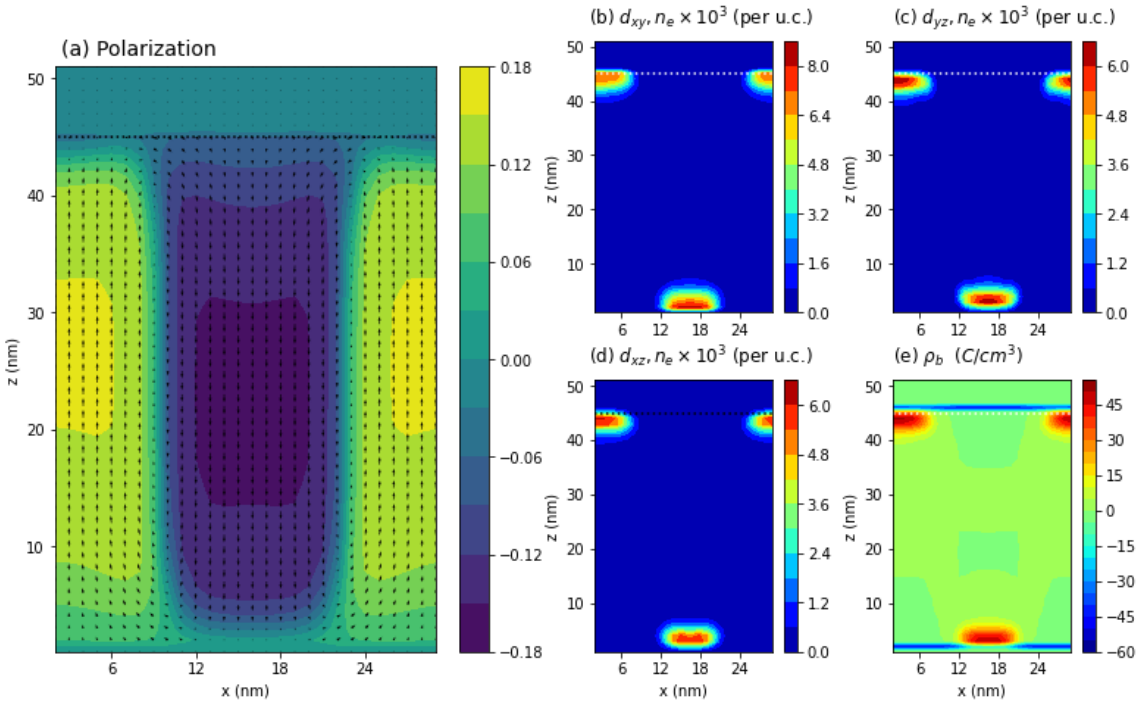

Figure A.2: Polarization, electron densities and bound polarization for n2D=0.1. These figures correspond with a cut through the model in the x-z plane. (a) The arrows correspond with the direction of the polarization vector. The color scale is based on the P_z component of polarization. The 180° domain walls have begun to tilt near the interfaces. (b) – (d) Free charge in the d_{xy}, d_{yz}, and (d) d_{xz} orbitals is concentrated at the tops of the domains. The d_{xy} orbital has the highest concentration of charge, and is more tightly held near the interfaces. (e) A line of bound charge is found along the interface at the top of the domain. Additional bound charge accumulates along the domain walls at the tops and bottoms where the polarization vectors rotate near the interface, and along the middle where the polarization is almost parallel to the domain wall.

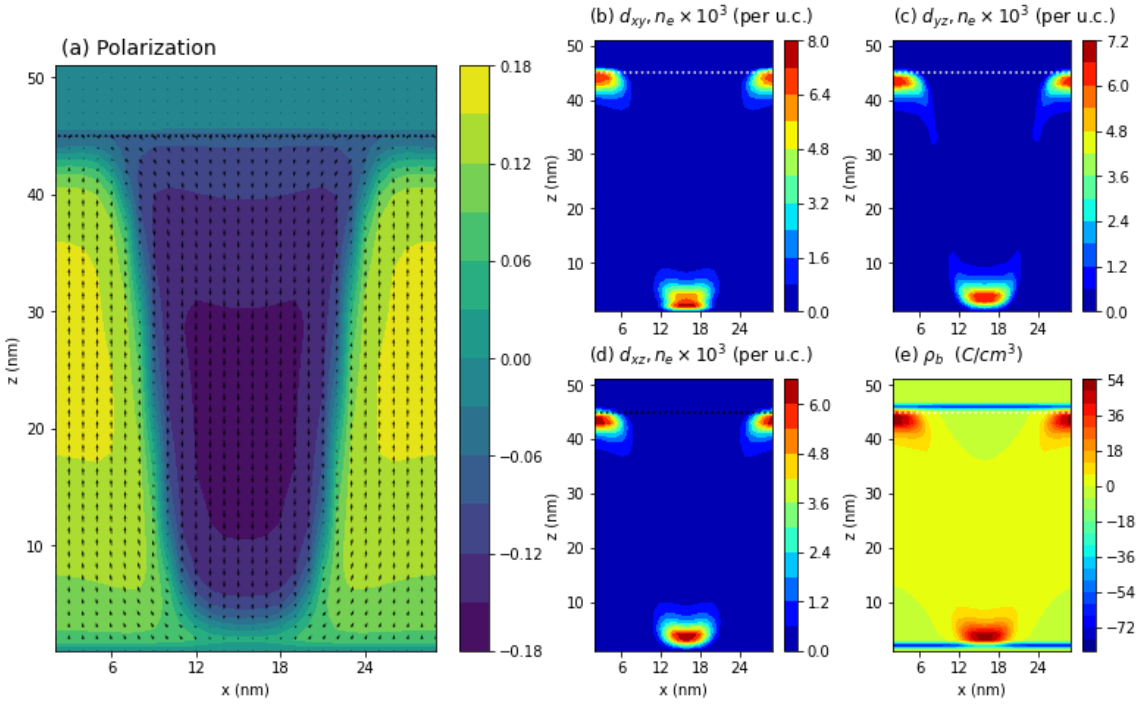

Figure A.3: Polarization, electron densities and bound polarization for n2D=0.15. These figures correspond with a cut through the model in the x-z plane. (a) The arrows correspond with the direction of the polarization vector. The color scale is based on the P_z component of polarization. The domain walls have a noticeable tilt. The positive ends of the domains have shrunk along the x-axis while the negative ends expanded. (b) Free charge in the d_{xy} orbital remains concentrated at the positive end of the domain, especially nearest the interface. (c) Free charge in the d_{yz} orbital is also concentrated at the positive end of the domain, although it is also beginning to noticeably stretch down into the arms of the domain wall. (d) Free charge in the d_{xz} orbitals has its highest concentration at the positive end of the domain, but is also spreading into the arms of the domain wall. (e) A line of bound charge is found along the interface at the top of the domain. Additional bound charge is concentrated along the positive end of the domain, and just reaching down into arms of the domain wall.

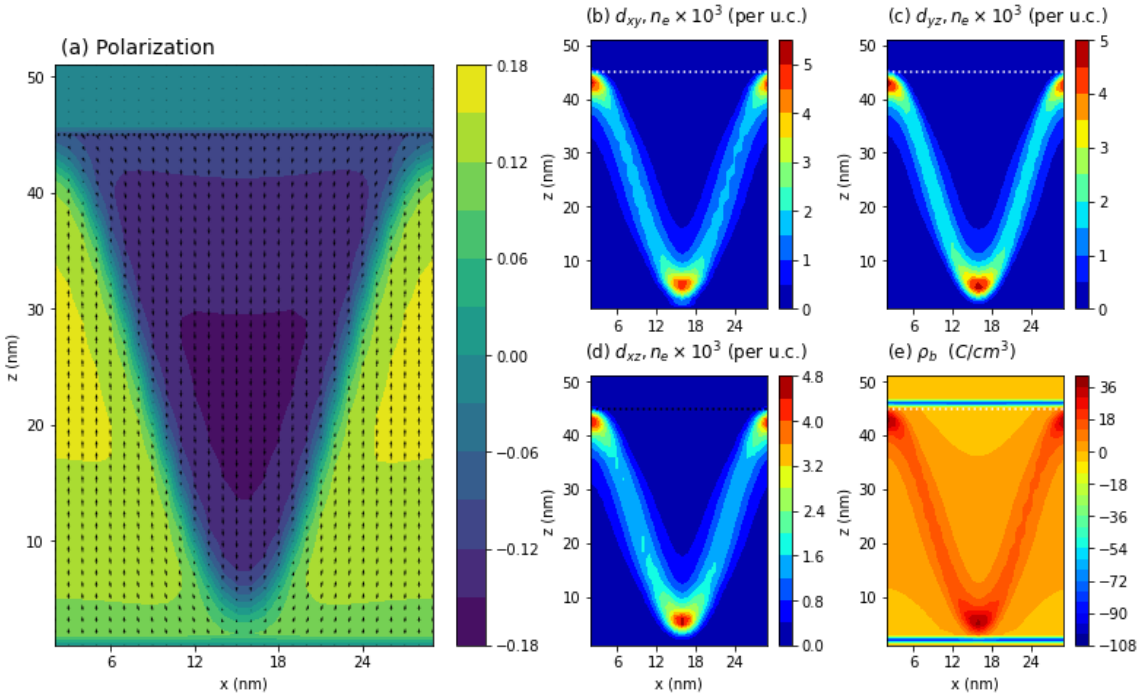

Figure A.4: Polarization, electron densities and bound polarization for n2D=0.2. These figures correspond with a cut through the model in the x-z plane. (a) The arrows correspond with the direction of the polarization vector. The color scale is based on the P_z component of polarization. The domain walls form a zig-zag pattern. The positive ends of the domain have narrowed to become vertices near the interface. (b) Free charge in the d_{xy} orbital remains most concentrated at the vertices, but has a clear concentration along the arms of the domain wall. (c) Free charge in the d_{yz} orbital is also concentrated at the vertices, but now has a noticeable, uniform concentration within the arms of the domain wall. (d) Free charge in the d_{xz} orbitals has its highest concentration in the vertices, but is also occupying the arms of the domain wall. From figure 4.9, the highest concentration of charge in the arms of the domain walls is in the d_{yz} orbitals. (e) Now that the vertices have pulled away slightly from the interface, a line of negative bound charge crosses the entire width of the interface. Bound charge is also clearly concentrated at the vertices, and along the arms of the domain wall.

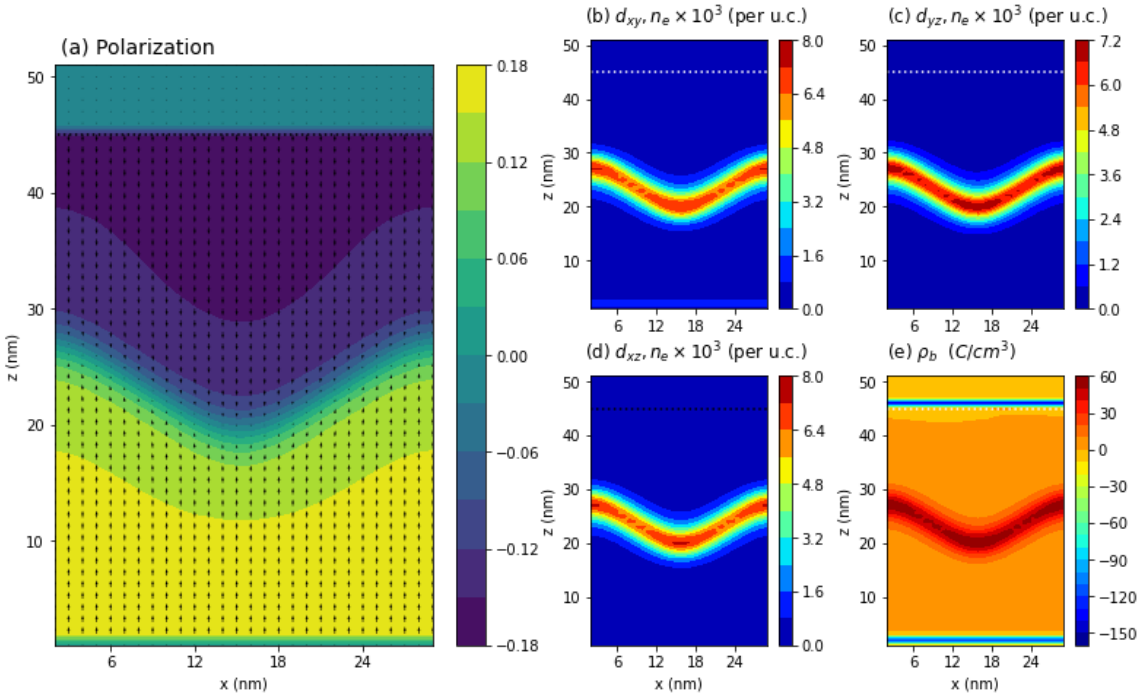

Figure A.5: Polarization, electron densities and bound polarization for n2D=0.3. These figures correspond with a cut through the model in the x-z plane. (a) The arrows correspond with the direction of the polarization vector. The color scale is based on the P_z component of polarization. The domain wall has flattened significantly, and looks like a sinusoidal wave. The wall is fully detached from the interfaces, and the maximum values for polarization now lie along the interfaces. (b) The bulk of the free charge in the d_{xy} orbital is concentrated within the domain wall. There is a small band of free charge along the bottom interface. (c) – (d) Free charge in the d_{yz} and d_{xz} orbitals is concentrated along the domain wall. The highest concentration is still found in the vertices. From figure 4.9, the highest concentration of charge in the arms of the domain walls is in the d_{xy} orbitals with d_{yz} and d_{xz} orbital types having higher concentrations along the outer edges. (e) A line of negative bound charge is still found along the interfaces. Positive bound charge is found along the domain wall with the highest concentration at the vertices.

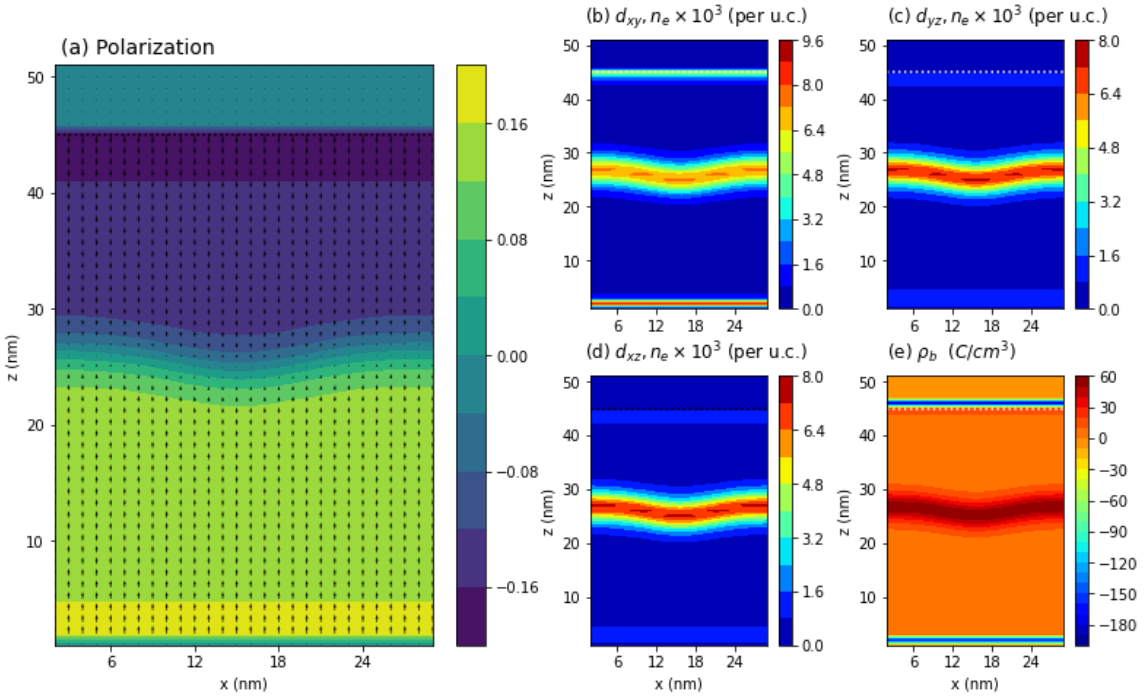

Figure A.6: Polarization, electron densities and bound polarization for n2D=0.4. These figures correspond with a cut through the model in the x-z plane. (a) The arrows correspond with the direction of the polarization vector. The color scale is based on the P_z component of polarization. The domain wall is nearly horizontal with a small dip in the center. The maximum polarization is found along the interfaces. (b) – (d) All three orbitals have bands of free charge along the interfaces, although only electrons in the d_{xy} orbital have a higher concentration than in the domain wall. The remainder of the free charge is concentrated within the domain wall in nearly equal amounts. (e) A line of negative bound charge is still found along the interfaces. Positive bound charge is found within the domain wall.

Appendix B

Code Discussion

B.1 Overview

The computational model was written in FORTRAN in order to take advantage of its speed, particularly in handling large matrices. The model was written on Windows 10 using Visual Studio Code (VSC) as the Integrated Development Environment (IDE). The selection of VSC was arbitrary, and no unique features of that software were used. It was compiled locally for testing using the Intel Classic FORTRAN Compiler (ifort) and linked with local copies of the Basic Linear Algebra Subprograms (BLAS) and Linear Algebra PACKages (LAPACK) libraries. Once the code was stable, it was uploaded and run on SHARCNet where it was compiled using the Intel Classic FORTRAN Compiler and the FlexiBLAS libraries. The Intel compiler supports multi-threading, so additional CPUs and memory were used to accelerate execution of the code on SHARCNet at the cost of overall CPU and memory efficiency.

The model consists of one program, nine modules, two libraries and up to three data files. They are described below:

1. Main.f90. This is the main program. It calls the other modules in sequence, and executes the computational algorithm described in Chapter 3 and shown in Figure 3.1.

2. Physical_Constants.f90. This module holds physical constants that can be referenced

by other programs or modules. e.g., the fundamental charge, Boltzmann's constant.

3. Coefficients.f90. This module holds all of the parameters for the model such as the width of the unit cell, width of the lattice, number of lattice points along each axis, the coefficients in the LGD equation, etc...

4. Initialize.f90. This module either (a) loads in data from an external file for the polarization (P_x, P_z), potential (ϕ), and charge densities ($\rho_{xy}, \rho_{xz}, \rho_{yz}$); or (b) generates an initial polarization and charge densities based on different configurations. e.g., uniform charge, 180^o domain walls, sinusoidal polarization.

5. LGD_Eqn_mod.f90. This module solves for the polarization that minimizes the LGD energy using the GNGA described in Chapter 3.

6. Potential_mod.f90. This module solves for the potential corresponding with the free, and bound charge densities.

7. Schrodinger_mod.f90. This modules solves for the energies and wavefunctions of the d_{xy}, d_{xz} and d_{yz} orbitals using the DSYEVD subroutine in the LAPACK library. It determines the chemical potential based on n_{2D}, and generates new free charge densities.

8. Convergence.f90. This module checks the convergence criteria. If convergence is not met, then it conducts a mixing routine and restarts the algorithm.

9. WriteToFile.f90. This module handles input and output of data with external files.

10. Anderson_Mix.f90. This module executes the Anderson Mixing algorithm described in Ref [62].

11. BLAS.lib. The Basic Linear Algebra Subprograms (BLAS) library. It works in combination with LAPACK to execute matrix algebra operations.

12. LAPACK.lib. The Linear Algebra PACKage (LAPACK) library. It works in combination with BLAS to execute matrix algebra operations.

13. data.dat. This is the main data file into which the model parameters, initial conditions, and final results are written.

14. import.dat. This is an optional file that is used to import pre-existing data into the model to act as the initial conditions.

15. archive.dat. This is an optional file into which intermediate data is appended at set intervals to observe the evolution of the model over multiple iterations.

B.2 Modules and Libraries

B.2.1 Main.f90

This is the main program that executes the computational algorithm described shown in Figure 3.1. It initializes the starting data for polarization, charge density, potential, and electric field. These values get passed into a WHILE loop that terminates when the convergence flag is true, or when it completes a set number of cycles. While in the loop, we maintain two sets of the primary variables to check for convergence, and allow for mixing. If they have not converged, we execute a mixing routine, increment the counter, and restart the loop. Once the loop terminates, we write the final results to an external file and end the program.

B.2.2 Physical_Constants.f90

This module has a collection of high-precision physical parameter that can be used by other modules. In our model, we used the following:

1. Permittivity of Free space, ϵ_0

2. Boltzmann's Constant, k_B

3. Planck's Constant, h

4. Fundamental Charge, e

5. Mass of the electron, m_e

B.2.3 Coefficients.f90

The model contains a large number of coefficients which can be adjusted to reflect different configurations They are primarily concentrated in this module, and are discussed in the following Tables B.1, B.2, B.3, B.4, B.5 and B.6. This module also contains two subroutines which convert arrays from the primary-to-secondary lattice and vice-versa.

Other parameters that can be adjusted, but aren't found in this module are:

1. Anderson Mixing parameters - simple_mix1 and simple_mix2. They are set by-hand in the Anderson_Mix.f90 module.

2. Simple or Anderson Mixing for potential in the Convergence.f90 module. Code for both is present, and the unused code needs to be commented out.

Parameter	**Value**	**Remarks**
version	2.3	Version number to track changes.
mixing_pol	0.001 – 1.0	Mixing parameter for simple mixing of polarization. Set to 1.0 when not being used.
mixing_pot	0.001 – 1.0	Mixing parameter for simple mixing of potential. Set to 1.0 when not being used.
mixing_rho	0.001 – 1.0	Mixing parameter for simple mixing of charge densities. Set to 1.0 when not being used.
mixing_background	0.001 – 1.0	Mixing parameter for simple mixing of background polarization. Set to 1.0 when not being used.
done	true or false	Set to true when convergence is reached.
eps_conv	10^{-4} – 10^{-6}	Determines convergence of the model from cycle-to-cycle. Final results were always in the 10^{-5} range for all values of n_{2D}.
conv_type	"pot" or "pol"	Determine the parameter on which to test convergence. Potential ("pot") was always used in this model.

Table B.1: Table of convergence parameters

Parameter	Value	Remarks
latt_dist	3.95×10^{-10}	Lattice constant, a. Based on STO.
cg_dist	1×10^{-9}	Lattice spacing, Δ.
dim_x	28	Number of lattice points along the x-axis.
dim_z_FEM	46	Number of lattice points along the z-axis in the FEM.
dim_z_PC	5	Number of lattice points along the z-axis in the polar cap.
dim_z_total	51	Total number of lattice points along the z-axis.
dim_y	28	Number of lattice points along the y-axis. For cubic symmetry, dim_y = dim_x.

Table B.3: Table of model geometry parameters

Parameter	Value	Remarks
counter_max	40,000 – 80,000	Total number of cycles to run before stopping if convergence not reached. Multiple runs were usually required to achieve convergence.
archive_threshold	100 – 1000	Number of cycles before data is output to an archiving file (archive.dat). Data is appended to observe behaviour over time throughout a run.
import	true or false	Determines whether initial data is imported (true) from a file (import.dat) or generated by routines within the Initialize.f90 module itself (false).
export	true or false	Determines whether data is appended (true) or not (false) to archive.dat.

Table B.2: Table of looping and import/export parameters

B.2.4 Initialize.f90

This module contains a subroutine that initializes the model. If the import flag is true, it will call the ImportFromFile subroutine in the WriteToFile.f90 module to import data from the import.dat file. Once imported, the Initialize.f90 module applies boundary conditions to ensure the data satisfies the model. If the import flag is false, then the Initialize.f90 module will generate polarization and/or charge density through one of the following models:

- Kittel Domains - Two regions are generated with the polarization aligned along the

Parameter	**Value**	**Remarks**
a1	1×10^{8}	Coefficient in the LGD equation for P_x^2.
a3	-8×10^{7}	Coefficient in the LGD equation for P_z^2.
b	5.88×10^{9}	Coefficient in the LGD equation for $\|\mathbf{P}\|^2$.
b'	-2.94×10^{9}	Coefficient in the LGD equation for $P_x^2 P_z^2$.
g11	1.0×10^{-10}	Coefficient in the LGD equation for $\left(\frac{\partial P_x}{\partial x}\right)^2 + \left(\frac{\partial P_x}{\partial z}\right)^2$.
g44	1.0×10^{-10}	Coefficients in the LGD equation for $\left(\frac{\partial P_x}{\partial z}\right)^2 + \left(\frac{\partial P_z}{\partial x}\right)^2$.
eta1	0	Not used. Future work.
eta2	0	Not used. Future work.
eta3	0	Not used. Future work.
eta4	0	Not used. Future work.
eta5	0	Not used. Future work.
eta6	0	Not used. Future work.
eta7	0	Not used. Future work.
eta8	0	Not used. Future work.
eta9	0	Not used. Future work.
P_x, P_z	Variable	(dim_x × dim_z_total) arrays for the x- and z-components of polarization.
P_x_old, P_z_old	Variable	(dim_x × dim_z_total arrays) for the x- and z-components of the old polarization.
Pbx, Pbz	Variable	(dim_x × dim_z_total) arrays for the x- and z-components of the background polarization.
Pbx_old, Pbz_old	Variable	(dim_x × dim_z_total) arrays for the x- and z-components of the old background polarization.
P_min	1×10^{-8}	The smallest possible value for polarization. Used to keep the GNGA from spending cycles converging to zero.
delta	0.5	Mixing term in the GNGA.
eps	1×10^{-8}	Convergence criteria for the GNGA.

Table B.4: Table of LGD module parameters

Parameter	Value	Remarks
potential	Variable	(dim_x × dim_z_total) array for the potential.
potential_old	Variable	(dim_x × dim_z_total) array for the old potential.
potential_free	Variable	(dim_x × dim_z_total) array for the potential arising from the free charge density.
potential_back	Variable	(dim_x × dim_z_total) array for the potential arising from the background polarization.
potential_ferro	Variable	(dim_x × dim_z_total) array for the potential arising from the ferroelectric polarization.
eps_p	10^{-8}	Convergence criteria for the relation method.
potential_bottom	0	Potential on the bottom capacitor plate.
potential_top	0	Potential on the top capacitor plate.
chi_PC	25.0	Dielectric susceptibility for the polar cap. Based on LAO.
chi_FEM	4.5	Dielectric susceptibility for the ferroelectric. Based on STO.

Table B.5: Table of Potential module parameters

z-axis (i.e. one region up, one region down) to simulate the $n_{2D} = 0.0$ case.

- Sinusoid - The P_z value is determined by the product of two sinusoids taking inputs from the x- and z-axes respectively. P_x is zero.
- Random - P_x and P_z are given random values between 0 and 1.
- Uniform - P_x and P_z are each given a uniform value.
- TANH - P_z is determined by a TANH equation along the z-axis. P_x is zero. The magnitude of the TANH equation is the value for the bulk polarization determined from Eq 1.4.

Additionally and/or alternately, the Initialize.f90 module can generate a free charge density through one of the following models:

- Plane of Charge - One or more of the orbitals has charge concentrated in the x-z plane for some value of z.

Parameter	**Value**	**Remarks**
hop_stay_xy	0	Hopping matrix element for remaining at the same lattice point in the d_{xy} orbital.
hop_stay_xz	0	Hopping matrix element for remaining at the same lattice point in the d_{xz} orbital.
hop_stay_yz	0	Hopping matrix element for remaining at the same lattice point in the d_{yz} orbital.
hop_parallel	-236×10^{-3}/J_to_eV	Hopping matrix element for moving to a lattice point in the same plane as the orbital. Conversion value found in Physical_Constants.f90 module.
hop_perp	-35×10^{-3}/J_to_eV	Hopping matrix element for moving to a lattice point that is perpendicular to the plane of the orbital. Conversion value found in Physical_Constants.f90 module.
SE_matrix_xy, SE_matrix_xz, SE_matrix_yz	Variable	$(\text{dim\_x} \times (\text{dim\_z\_FEM} - 2))^2$ arrays for the coarse-grained Hamiltonians for each orbital.
W_xy, W_xz, W_xy	Variable	(dim_x × (dim_z_FEM - 2)) arrays containing the energies from the coarse-grained Hamiltonians. Determined by DSYEVD subroutine in LAPACK.
temp	10	Temperature in Kelvin (K).
eps_mu	10^{-8} – 10^{-12}	Convergence criteria for the bisection method.
chem_pot	Variable	Chemical potential. Determined in Schrodinger_mod.f90.
n2D	0.0 - 0.4	2D electron density in units of electrons per unit cell.
rho_xy, rho_xz, rho_yz	Variable	(dim_x × dim_z_total) arrays for the free charge densities.
rho_xy_old, rho_xz_old, rho_yz_old	Variable	(dim_x × dim_z_total) arrays for the old free charge densities.
E_x, E_z	Variable	(dim_x × dim_z_total) arrays for the electric field. Calculated from potential.

Table B.6: Table of Schrodinger module parameters

- Uniform Density - One of more of the orbitals has a uniform charge density.

The potential is not initialized in this module. If the import flag is false, then the potential is generated through the Potential_mod.f90 module as a separate step in the Main.f90 program.

Once the data has been initialized (from either source), the WriteInitialize subroutine in the WriteToFile.f90 module is called to export the initial values into the data.dat file.

B.2.5 LGD_Eqn_mod.f90

The LGD_Eqn_mod.f90 module implements the GNGA through the Solve_LGD subroutine which is called by Main.f90. It executes a WHILE loop until the conv_lgd flag is true. The first and second order partial derivatives of the free energy have been implemented as subroutines.

B.2.6 Potential_mod.f90

The Potential_mod.f90 module solves for the potential through the Solve_Potential subroutine which is called by Main.f90. The background polarization is calculated based on the electric field. The background_charge subroutine generates the bound charge density from the polarization. The solve_phi subroutine uses the relaxation method to find the potential from the free and bound charge densities. A new electric field is determined from the new potential.

B.2.7 Schrodinger_mod.f90

The Schrodinger_mod.f90 module solves for the free charge densities through the Solve_Schrodinger subroutine which is called by Main.f90. It generates the SE_matrix for each of the orbital types based on the hopping matrix elements and the potential. The eigenvalues and eigenvectors of each SE_matrix are solved using the DSYEVD subroutine in the LAPACK library. The eigenvalues are output into the W arrays while the SE_matrix is replaced by a matrix of eigenvectors. The energies in W and n_{2D} are used to find the chemical potential using the bisection method. Once found, they are combined with the eigenvectors and the Fermi Function to generate the free charge densities.

Parameter	**Range**
Anderson Mixing, mix_1	0.001 - 0.003
Anderson Mixing, mix_2	0.001 - 0.003
Simple Mixing	0.01 - 0.001

Table B.7: Table of Mixing Parameters

B.2.8 Convergence.f90

The Convergence.f90 module tests for convergence through the Test_Convergence subroutine which is called by Main.f90. The parameter for which convergence is tested is determined by the conv_type value (e.g., potential or polarization). If the change in potential (or polarization) is below the threshold determined by eps_conv, then the done flag is set to true. If it is not below the threshold, then the potential (or polarization) is mixed using simple mixing or Anderson Mixing. The type of mixing is selected by hand in this module, and the appropriate code needs to be present while the other is commented out. If the potential is mixed, then a new electric field is calculated.

A range of values for the mixing parameters were tested. The most successful values are found in Table B.7.

B.2.9 WriteToFile.f90

The WriteToFile.f90 module tests is responsible for the import and export of data to files. It contains three subroutines:

- WriteInitialize - This subroutine is called by the Initialize.f90 module. It writes all of the coefficients from the Coefficients.f90 module, and the polarization, potentials, charge densities, and electric field after they have been initialized. The data is appended to the data.dat file.

- Write2File - This subroutine is called by Main.f90 when the computational algorithm is complete. It outputs the polarization, potentials, charge densities, and electric field to the data.dat file.

- Archive2File - This subroutine is called by Main.f90 whenever the cycle count is a

multiple of the archive_threshold. It appends the polarization, potentials, charge densities, and electric field to the archive.dat file.

- ImportFromFile - This subroutine is called by the Initialize.f90 module. It imports the polarization, potentials, charge densities, and electric field from the import.dat file.

B.2.10 Anderson_Mix.f90

The Anderson_Mix.f90 module executes the Anderson Mixing algorithm on an array described in Ref [62]. It is called by the Convergence.f90 module. It has two mixing parameters - simple_mix1 and simple_mix2 - which are set by hand. This module was provided by Dr. Bill Atkinson, Department of Physics and Astronomy, Trent University.

B.3 Compiler Commands

The compiler commands for the different environments are found in table B.8. The -O2 flag was used to optimize the code for runtime. The FlexiBLAS library needs to be pre-loaded in the SHARCNet environment. Local copies of BLAS and LAPACK were used on the local machine.

B.4 Git Hub

The code has been uploaded to GitHub at the following link: https://github.com/CornellBC/Electron-Doped-Perovskite-Ferroelectrics/tree/main

Activity	**Environment**	**Commands**
Compile Module	Local Machine & SHARCNet	ifort -c Anderson_Mix.f90 Physical_Constants.f90 Coefficients.f90 Initialize.f90 WriteToFile.f90 Coefficients.f90 LGD_Eqn_mod.f90 Potential_mod.f90 Schrodinger_mod.f90 Convergence.f90 Main.f90
Compile Program	Local Machine	ifort -c Anderson_Mix.f90 Physical_Constants.f90 Coefficients.f90 Initialize.f90 WriteToFile.f90 Coefficients.f90 LGD_Eqn_mod.f90 Potential_mod.f90 Schrodinger_mod.f90 Convergence.f90 Main.f90
	SHARCNet	load module flexiblas ifort -O2 Main.o Anderson_Mix.o Physical_Constants.o Coefficients.o WriteToFile.o Coefficients.o Initialize.o LGD_Eqn_mod.o Potential_mod.o Schrodinger_mod.o Convergence.o -lflexiblas

Table B.8: Table of compiler commands

Appendix C

Generating the LGD Equation

The process of generating a free energy equation that respects a symmetry is straightforward, but tedious. Our LGD equation was determined from the application of the cubic symmetries (see table C.1) to a generalized fourth-order equation in the order parameter. We won't repeat the process here, but do provide an example of the steps for a slightly simpler, fourth order equation in the order parameter, **P**.

1. Write down all terms in a free energy equation in the order parameter up to fourth-order.

$$\begin{aligned}
\mathcal{F} =& P_0 + a_1 P_x + a_2 P_y + a_3 P_z \\
&+ \frac{b_1}{2} P_x^2 + \frac{b_2}{2} P_y^2 + \frac{b_3}{2} P_z^2 \\
&+ b_1' P_x P_y + b_2' P_x P_z + b_3' P_y P_z \\
&+ \frac{c_1}{3} P_x^3 + \frac{c_2}{3} P_y^3 + \frac{c_3}{3} P_z^3 \\
&+ c_1' P_x^2 P_y + c_2' P_x^2 P_z + c_3' P_x P_y^2 + c_4' P_y^2 P_z \\
&+ c_5' P_x P_z^2 + c_6' P_y P_z^2 + c_7' P_x P_y P_z \\
&+ \frac{d_1}{4} P_x^4 + \frac{d_2}{4} P_y^4 + \frac{d_3}{4} P_z^4 \\
&+ d_1' P_x^3 P_y + d_2' P_x^3 P_z + d_3' P_x P_y^3 \\
&+ d_4' P_y^3 P_z + d_5' P_x P_z^3 + d_6' P_y P_z^3 \\
&+ d_7' P_x^2 P_y^2 + d_8' P_x^2 P_z^2 + d_9' P_y^2 P_z^2
\end{aligned} \tag{C.1}$$

2. For each symmetry, construct the transformations for each component. e.g., Inversion symmetry

$$x \Rightarrow -x$$

$$y \Rightarrow -y$$

$$z \Rightarrow -z$$

e.g., 90^{o} counter-clockwise rotation around the z-axis

$$x \Rightarrow y$$

$$y \Rightarrow -x$$

$$z \Rightarrow z$$

A complete list of the cubic transformations can be found at table C.1.

3. The free energy equation must look the same in the new coordinate system. Substitute the transformed coordinates into Eq (C.1) for a given symmetry. e.g., under 90^{o} counter-clockwise rotation around the z-axis, $P_x' = P_y, P_y' = -P_x, P_z' = P_z$ where the prime (') refers to the transformed coordinates. The free energy in the transformed

coordinates, $\mathcal{F}'$, becomes

$$\begin{aligned}
\mathcal{F}' =& P_0' + a_1 P_y + a_2(-P_x) + a_3 P_z \\
&+ \frac{b_1}{2}P_y^2 + \frac{b_2}{2}(-P_x)^2 + \frac{b_3}{2}P_z^2 \\
&+ b_1' P_y(-P_x) + b_2' P_y P_z + b_3'(-P_x)P_z \\
&+ \frac{c_1}{3}P_y^3 + \frac{c_2}{3}(-P_x)^3 + \frac{c_3}{3}P_z^3 \\
&+ c_1'(P_y)^2(-P_x) + c_2' P_y^2 P_z + c_3' P_y(-P_x)^2 + c_4'(-P_x)^2 P_z \\
&+ c_5' P_y P_z^2 + c_6'(-P_x)P_z^2 + c_7' P_y(-P_x)P_z \\
&+ \frac{d_1}{4}P_y^4 + \frac{d_2}{4}(-P_x)^4 + \frac{d_3}{4}P_z^4 \\
&+ d_1' P_y^3(-P_x) + d_2' P_y^3 P_z + d_3' P_y(-P_x)^3 \\
&+ d_4'(-P_x)^3 P_z + d_5' P_y P_z^3 + d_6'(-P_x)P_z^3 \\
&+ d_7' P_y^2(-P_x)^2 + d_8' P_y^2 P_z^2 + d_9'(-P_x)^2 P_z^2
\end{aligned}$$

$$\begin{aligned}
=& P_0' - a_2 P_x + a_1 P_y + a_3 P_z \\
&+ \frac{b_2}{2}P_x^2 + \frac{b_1}{2}P_y^2 + \frac{b_3}{2}P_z^2 \\
&- b_1' P_x P_y - b_3' P_x P_z + b_2' P_y P_z \\
&- \frac{c_2}{3}P_x^3 + \frac{c_1}{3}P_y^3 + \frac{c_3}{3}P_z^3 \\
&- c_3' P_x^2 P_y + c_4' P_x^2 P_z - c_1' P_x P_y^2 + c_2' P_y^2 P_z \\
&- c_6' P_x P_z^2 + c_5' P_y P_z^2 - c_7' P_x P_y P_z \\
&+ \frac{d_2}{4}P_x^4 + \frac{d_1}{4}P_y^4 + \frac{d_3}{4}P_z^4 \\
&- d_3' P_x^3 P_y - d_4' P_x^3 P_z - d_1' P_x P_y^3 + d_2' P_y^3 P_z \\
&- d_6' P_x P_z^3 + d_5' P_y P_z^3 \\
&+ d_7' P_x^2 P_y^2 + d_9' P_x^2 P_z^2 + d_8' P_y^2 P_z^2
\end{aligned} \tag{C.2}$$

4. Since the energy must be the same before and after the transformation, we can equate the coefficients between Eq (C.1) and Eq (C.2). Under this symmetry, we must have

that $P_0' = P_0; a_1 = -a_2 = a_2 = 0; b_2 = b_1; b_1' = -b_1' = 0; b_2' = -b_3' = b_3' = 0; c_1 = -c_2 = c_2 = 0; c_1' = -c_3'; c_2' = c_4'; c_5' = -c_6' = c_6' = 0; c_7' = -c_7' = 0; d_1 = d_2; d_1' = -d_3'; d_2' = -d_4' = -d_2' = 0; d_5' = -d_6' = -d_5' = 0; d_8' = d_9'$.

5. Write the new, reduced free energy equation using the new coefficients determined from the symmetry.

$$\begin{aligned}\mathcal{F} =& P_0 + a_3 P_z \\ &+ \frac{b_1}{2}\left[P_x^2 + P_y^2\right] + \frac{b_3}{2}P_z^2 \\ &+ \frac{c_3}{3}P_z^3 \\ &+ c_1'\left[P_x^2 P_y + P_x P_y^2\right] + c_2'\left[P_x^2 P_z + P_y^2 P_z\right] \\ &+ \frac{d_1}{4}\left[P_x^4 + P_y^4\right] + \frac{d_3}{4}P_z^4 \\ &+ d_1'\left[P_x^3 P_y - P_x P_y^3\right] \\ &+ d_7' P_x^2 P_y^2 + d_8'\left[P_x^2 P_z^2 + P_y^2 P_z^2\right] \end{aligned} \tag{C.3}$$

6. Repeat for the remaining symmetries, or until there are no terms left.

In our LGD free energy equation, gradient terms for the polarization up to first order where also included. These are also transformed, where we treat the transformation of the derivative and the polarization separately, and then recombine. e.g., under 90° counter-clockwise rotation around the z-axis, we have $x' = y, y' = -x, z' = z, P_x' = P_y, P_y' = -P_x, P_z' = P_z$ where the prime (') refers to the rotated coordinate system. The derivatives become:

$$\begin{aligned}\frac{\partial}{\partial x'} &= \frac{\partial}{\partial y} \\ \frac{\partial}{\partial y'} &= -\frac{\partial}{\partial x} \\ \frac{\partial}{\partial z'} &= \frac{\partial}{\partial z}\end{aligned}$$

Combined with the transformations of the polarization, we have:

$$\frac{\partial P'_x}{\partial x'} = \frac{\partial}{\partial y} P_y = \frac{\partial P_y}{\partial y}$$
$$\frac{\partial P'_y}{\partial y'} = -\frac{\partial}{\partial x}(-P_x) = \frac{\partial P_x}{\partial x}$$
$$\frac{\partial P'_z}{\partial z'} = -\frac{\partial}{\partial z} P_z = \frac{\partial P_z}{\partial z}$$

The free energy equations for different symmetries are well-known. Appendix A to Ref [51] contains examples for several common perovskite ferroelectrics.

Symmetry	**Transformations**
90^o counter-clockwise rotation around the z-axis	$x \Rightarrow y$ $y \Rightarrow -x$ $z \Rightarrow z$
90^o counter-clockwise rotation around the y-axis	$x \Rightarrow -z$ $y \Rightarrow y$ $z \Rightarrow x$
90^o counter-clockwise rotation around the x-axis	$x \Rightarrow x$ $y \Rightarrow z$ $z \Rightarrow -y$
120^o counter-clockwise rotation around the (111) axis	$x \Rightarrow z$ $y \Rightarrow x$ $z \Rightarrow y$
120^o counter-clockwise rotation around the $(\bar{1}\bar{1}1)$ axis	$x \Rightarrow -z$ $y \Rightarrow x$ $z \Rightarrow -y$
120^o counter-clockwise rotation around the $(\bar{1}11)$ axis	$x \Rightarrow -y$ $y \Rightarrow z$ $z \Rightarrow -x$
120^o counter-clockwise rotation around the $(1\bar{1}1)$ axis	$x \Rightarrow -y$ $y \Rightarrow -z$ $z \Rightarrow x$
Mirror image across the x-z plane	$x \Rightarrow x$ $y \Rightarrow -y$ $z \Rightarrow z$
Mirror image across the y-z plane	$x \Rightarrow -x$ $y \Rightarrow y$ $z \Rightarrow z$
Mirror image across the x-y plane	$x \Rightarrow x$ $y \Rightarrow y$ $z \Rightarrow -z$
Inversion	$x \Rightarrow -x$ $y \Rightarrow -y$ $z \Rightarrow -z$

Table C.1: Table of cubic symmetries and associated transformations